An Evaluation Testbed for Alternative Wind Turbine Blade Tip Designs

by

Drew Gertz

A thesis
presented to the University of Waterloo
in fulfillment of the
thesis requirement for the degree of
Master of Applied Science
in
Mechanical Engineering

Waterloo, Ontario, Canada, 2011

I hereby declare that I am the sole author of this thesis. This is a true copy of the thesis, including any required final revisions, as accepted by my examiners.

I understand that my thesis may be made electronically available to the public.

Abstract

The majority of present-day horizontal axis wind turbine blade tips are simple designs based on historical trends. There is, however, some evidence that varying the design of the tip can result in significant changes in performance characteristics such as power output, noise, and structural loading. Very few studies have tested this idea on an actual rotating blade and there is much to be investigated. Thus, a project was devised to examine experimentally the effect of various tip designs on an operational rotating wind turbine rotor.

A tapered, twisted blade 1.6 m in length was custom designed for use in the UW Wind Energy Research Facility using the blade element momentum (BEM) method. A coupling mechanism was designed such that the outer 10% of each blade could be exchanged to evaluate the effect of different tip designs. A set of three blades was fabricated out of fibre-reinforced plastic, while the tips were machined out of maple wood on a CNC milling machine.

The blade was evaluated with a standard rectangular tip to establish baseline performance against which to compare the alternative tip configurations. The three-bladed rotor was tested at shaft speeds from 100 rpm to 240 rpm in wind speeds up to the facility maximum of 11.1 m/s. The rotor was found to have a maximum power coefficient of 0.42 at a tip speed ratio of 5.3 and a 1.45 kW rated power at a wind speed of 11 m/s. The performance was compared to predictions made using the BEM method with airfoil data generated using a modified Viterna method and the Aerodas method. While the Aerodas data was capable of predicting the power fairly accurately from 5 m/s to 10 m/s, the modified Viterna method predicted the entire curve much more accurately.

Two winglet designs were also tested. The first (called Maniaci) was designed by David Maniaci of Pennsylvania State University and the other (called Gertz) was designed by the author. Both winglets were found to augment the power by roughly 5% at wind speeds between 6.5 m/s and 9.5 m/s, while performance was decreased above and below this speed range. It was calculated that the annual energy production could be increased using the Maniaci and Gertz winglets by 2.3% and 3%, respectively. Considering the preliminary nature of the study the results are encouraging and it is likely that more optimal winglet designs could be designed and evaluated using the same method. More generally, this study proved that the blades with interchangeable tips are capable of being used as an evaluation testbed for alternative wind turbine blade tip designs.

Acknowledgements

I would like to first of all thank all thank my supervisor Professor David Johnson. His navigation of the fine line a supervisor must walk between providing direction and allowing independence was ideally suited to my needs. Professor Johnson happily provided the support and resources I needed to undertake my multi-disciplinary thesis project. I feel priviledged to have had him as a supervisor and my accomplishments would not have been possible without him. I also sincerely appreciate being given the opportunity to attend conferences in Halifax, Victoria, Montreal, Toronto, and Alexandria Bay, N.Y. Machinists Jason Benninger and Rob Wagner of the Department of Mechanical Engineering were also instrumental to the success of my project. The hours of work they put in to prepare my molds and wing tips as well as their trust and generosity in lending me tools was greatly appreciated. The help of Dave Cyr of Composotech Structures, Inc. was also crucial to the success of my project. Through his dedicated efforts I learned the art of mold finishing and fibreglass construction of wind turbine blades. His willingness to listen to my countless questions over the telephone and walk me through several intricate procedures of fibreglass construction were also greatly appreciated. Composotech Structures Inc. was also very generous for donating the time, space, materials, and tools required for me to build my blades. The contributions of Professor Mark Maughmer and his Ph.D. student David Maniaci were also greatly appreciated. Professor Maughmer provided great insight into the physics of winglets through multiple phone calls and emails, and David's effort to design a winglet specifically for my blade was a great contribution to the project. I would also like to thank my colleagues Brian Gaunt, Erik Skensved, Stephen Orlando, Adam Bale, and Vivian Lam who were always willing to take time out of their schedules to help me. I am especially thankful for their help in erecting and tearing down the turbine rig on several occasions. I would like to thank Gord Hitchman for his valuable help throughout my multiple test campaigns. I also appreciate the insight provided by Professor Sanjeev Bedi into mold machining and blade structural design. Finally, thank you to my friends and family for their understanding and support, without which many phases of this project would have been extremely more difficult.

Dedication

This is dedicated to all of the engineers who believe in the unparalelled value of scientific experimentation.

Table of Contents

List of Tables

List of Figures

Nomenclature

Roman Symbols

a	Axial induction factor [-]
a'	Angular induction factor [-]
$A0$	Angle of attack at zero 2D lift [degrees]
A_1	Constant used in Viterna model [-]
A_2	Constant used in Viterna model [-]
a_c	Critical induction factor [-]
$ACD1$	Angle of attack at maximum pre-stall drag [degrees]
$ACD1'$	Angle of attack at maximum pre-stall 2D drag [degrees]
$ACL1$	Angle of attack at maximum pre-stall lift [degrees]
$ACL1'$	Angle of attack at maximum pre-stall 2D lift [degrees]
A_d	Disc area [m^2]
AR	Aspect ratio [-]
b	Wing semi-span [m]
B_2	Constant used in Viterna model [-]
c	Airfoil chord length [m]
$CD0$	Minimum 2D drag coefficient [-]

$CD1$	Pre-stall drag coefficient [-]
$CD1'$	Pre-stall 2D drag coefficient [-]
$CD2$	Post-stall drag coefficient [-]
$CL1$	Pre-stall lift coefficient [-]
$CL1'$	Pre-stall 2D lift coefficient [-]
$CL2$	Post-stall lift coefficient [-]
c_m	Chord at mean radius [m]
c_s	Speed of sound [m/s]
D	Airfoil drag [N]
e	Wing span efficiency [-]
F	Aerodynamic force [N]
$f(\mu)$	Combined root/tip loss factor [-]
$F1$	Parameter used in Aerodas model [-]
$F2$	Parameter used in Aerodas model [-]
$f_R(\mu)$	Root loss factor [-]
$f_T(\mu)$	Tip loss factor [-]
$G1$	Parameter used in Aerodas model [-]
$G2$	Parameter used in Aerodas model [-]
I	Flow turbulence [%]
K	Parameter used in induction factor correction [-]
L	Airfoil lift [N]
L/D	Lift-to-drag ratio [-]
M	Airfoil pitching moment [Nm]

Ma	Mach number [-]
N	Number of blades
$N1$	Parameter used in Aerodas model [-]
$N2$	Parameter used in Aerodas model [-]
P	Power extracted by disc [W]
R	Rotor radius [m]
$RCL1$	Parameter used in Aerodas model [-]
$RCL2$	Parameter used in Aerodas model [-]
Re	Reynolds number [-]
rpm	Revolutions per minute [rev/min]
S	Wing area [m^2]
$S1$	Parameter used in Aerodas model [-]
$S1'$	Slope of linear segment of pre-stall 2D curve [-]
T	Thrust [N]
t	Airfoil thickness [m]
t/c	Airfoil thickness-to-chord ratio [-]
u	Velocity in streamwise direction [m/s]
u'	Fluctuating velocity component [m/s]
$\overline{u}$	Mean velocity [m/s]
V	Wind velocity [m/s]
v	Velocity in horizontal direction [m/s]
W	Relative velocity at blade element [m/s]
w	Velocity in vertical direction [m/s]

Greek Symbols

α	Angle of attack [degrees]
β	Blade twist [degrees]
λ	Tip speed ratio [-]
μ	Normalized radius [-]
μ_R	Normalized radius at the root [-]
ν	Kinematic viscosity [m^2/s]
ρ	Air density [kg/m^3]
$\sigma(r)$	Solidity at radius r [-]
σ_V	Parameter used in Viterna model [-]
τ	Parameter used in Viterna model [-]
φ	Inflow angle [degrees]
Ω	Rotor angular velocity [rad/s]

Subscripts

15^o	Coefficient value at 15 degrees angle of attack
20^o	Coefficient value at 20 degrees angle of attack
7^o	Coefficient value at 7 degrees angle of attack
aug	Augmentation
$bladedrag$	Due to blade drag
d	Drag
$disc$	At rotor disc
$drivetrain$	Due to drivetrain losses
e	Effective

$flatplate$	Value for flat plate
i	Induced
∞	Freestream
l	Lift
$load$	At the load
m	Moment
max	Maximum
m	Mean
n	Normal force
o	Infinite aspect ratio
P	Power
GEN	Generated by rotor
r	Due to blade rotation
s	Value at 2D stall angle
$S809$	Value for S809 airfoil
$S83X$	Value for S83X airfoil
$spinrotor$	To spin rotor
T	Thrust
t	Tangential force
tip	Blade tip
$upstream$	Upstream of rotor disc
w	Resultant at winglet

Chapter 1

Introduction

1.1 Wind Energy

Humans have been making use of the energy in the wind for at least 3000 years, however until recently it was only in sailing, grain grinding, and water pumping applications [1]. The earliest known windmill designed to generate electricity was the 12 kW DC model introduced by Brush in the USA in the late nineteenth century [2]. Due to cheap, abundantly available fossil fuels, however, wind turbines were rarely used for anything other than battery charging for remote dwellings for most of the twentieth century. Even that application became obsolete once access to the electricity grid became available. It was only after the oil shock of 1973 that there became significant interest in wind power generation [1]. Government funded research programs sprang up worldwide, and many different concepts of horizontal- and vertical-axis wind turbines (HAWTs and VAWTs) were proposed and tested. The "Danish" concept wind turbine, a 3-bladed, stall-regulated fixed-speed HAWT emerged as the dominant concept in commercial-scale applications; this judging by its widespread adoption by manufacturers worldwide [2]. A typical HAWT consists of a support structure known as the tower, the nacelle which houses the gearbox and generator, and a rotor with typically 3 blades. A modern 3-bladed turbine is pictured in figure 1.1 with the relevant components labeled.

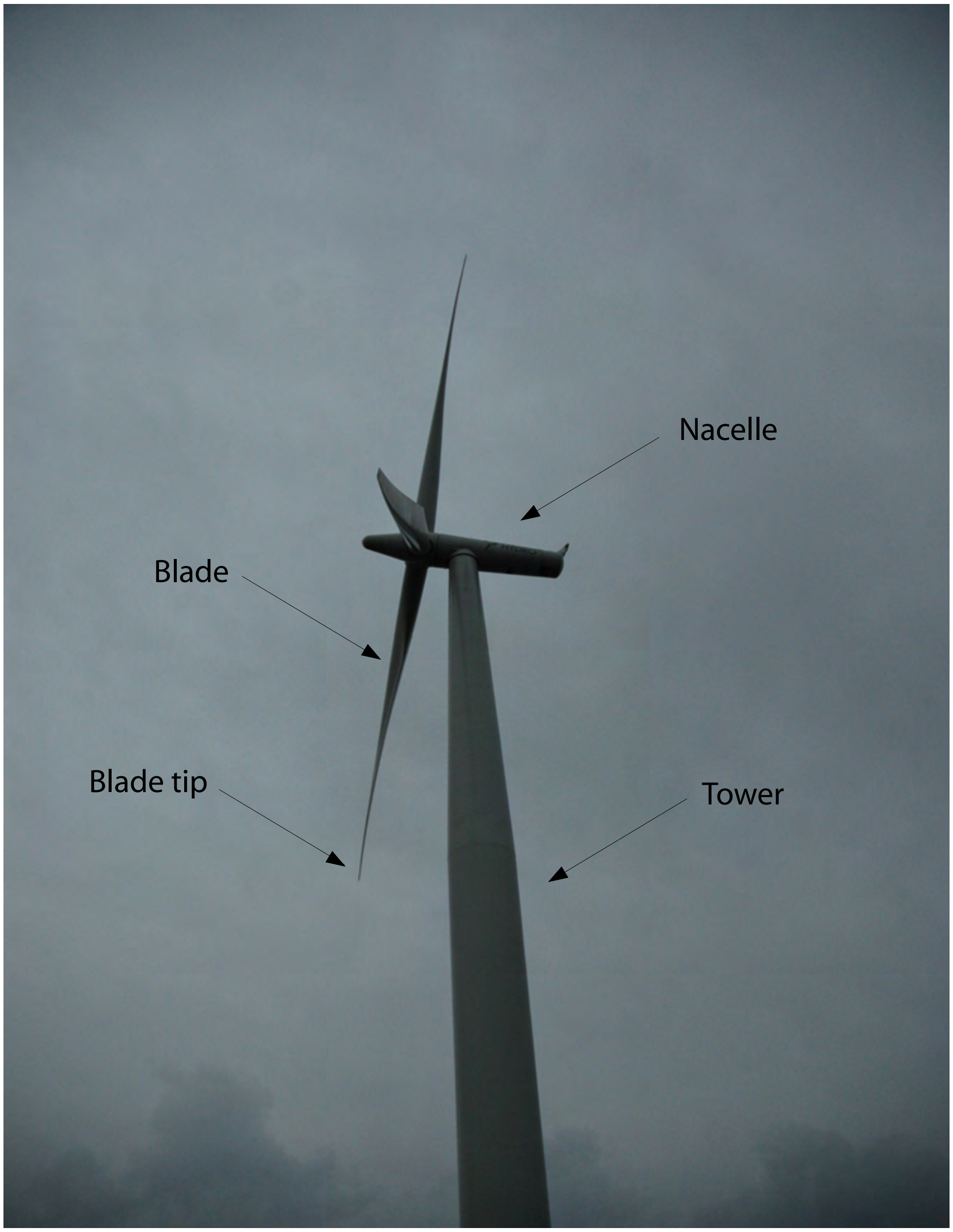

Figure 1.1: Picture of a modern wind turbine.

The wind turbine tower and nacelle are typically made of steel, while the blades are built of fibreglass. Wind turbines are identified by their rated power, that is, the power produced at a certain wind speed. This rated wind speed is typically 11 m/s.

Turbines are manufactured in a wide range of scales. A small-scale 1kW machine could have a hub height of 12 m and a rotor diameter of 2 m, whereas commercial-scale turbines can be rated at several MW. One of the world's current largest turbines is the Enercon E-126 with a hub height of 135 m, rotor diameter of 126 m and rated power of 7 MW.

Since the relatively recent adoption of wind turbines for power generation, world-wide installed capacity has grown to 175 GW as of June 2010 [3]. This is a rather impressive figure considering the technology, which only began to be explored in the mid- to late-seventies, should still be considered rather nascent compared to other established commercial-scale power generation platforms. While commercial use of wind turbines is expected to continue to expand, ample improvements to increase efficiency, reliability, and public acceptance of the technology are possible.

1.2 Project Motivation

The Wind Energy Research Group at the University of Waterloo conducts research with the goal of exploring the aerodynamics of wind turbines. As alluded to above, technology improvements to wind turbines are possible, and this includes those in the realm of aerodynamic design. The component of most importance with respect to wind turbine aerodynamics is the blade. Thus efforts by the group are typically focused on the aerodynamic performance of the blade. In terms of potential design improvements, blade tips have long been known to be a source of aerodynamic inefficiency on wind turbines. The blade tip is labeled in figure 1.1. What are known as tip-loss effects reduce the power output while blade tips are also a significant source of turbine noise. The designs of current HAWT blade tips vary depending on scale but are for the most part simple shapes within the blade plane. The standard tip is most common for small-scale applications (0 - 50 kW), while the tapered tip has become prevalent on sizes beyond 50 kW. See figure 1.2 for sketches of the standard (Std) and tapered (A) tips, plus several other concepts. These conventional shapes are popular due to their proven track records and ease of manufacture. There is, however, good reason to explore alternative tip designs.

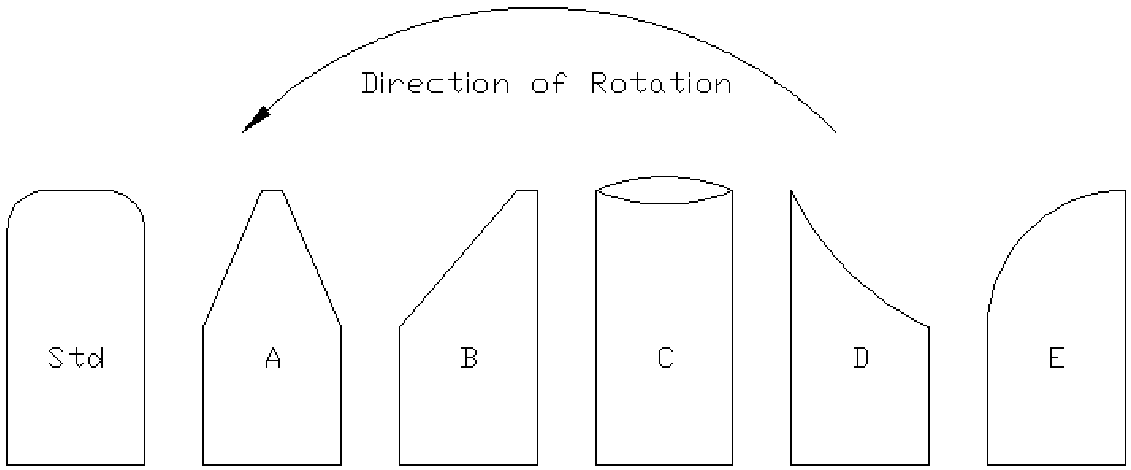

Figure 1.2: Various blade tip designs. Std - standard; A - tapered; B - swept tapered; C - non-planar; D - ogee; E - rounded taper. Adapted from Antoniou et al [4].

Simple alterations to the standard tip such as the swept (B) and ogee (D) shapes have been found to produce desirable results in terms of bending load alleviation [4]; whereas out of plane shapes, such as the endplate and winglet (C), can apparently augment the power output. Computational and experimental studies on small-scale rotors have found that the power produced by a wind turbine can be increased by 4 - 9 % using such devices [5, 6]. Computational studies have also been performed on large rotors (MW-scale), and predict that power can be augmented by 2 - 3% at such a scale [7]. Finally, it has also been suggested that alternative tip shapes can reduce aerodynamic blade noise [8].

1.3 Thesis outline and organization

It is clear that unconventional tip shapes can produce certain desirable improvements in wind turbine performance. In reviewing the literature, it was also found that very little experimental research on the topic has been performed on operational rotating turbine blades. For these reasons, and with the large scale experimental facilities available, a research study that explored the effect of various blade tip designs on the performance of a wind turbine was developed. This project involved designing and fabricating a wind turbine blade that is compatible with the available rig and facility and has a mechanism for exchanging tips in order to evaluate the variation in performance due solely to different tip designs. Due to the instrumentation currently installed on the rig and at the testing facility, rotor performance testing was limited to power generation measurements. For this reason, only tips that are known to affect the power generation of the rotor, namely winglets, were tested.

The project was divided into three phases: firstly the aerodynamic design of the baseline blade and two winglets; secondly the fabrication of the aforementioned blade design with integrated tip exchange mechanism; and thirdly the performance testing of the three-bladed rotor with standard tip and the two different winglet designs. This thesis begins by giving the reader a review of two- and three-dimensional wing aerodynamics followed by a section dedicated to the theory required to understand the blade design technique. Related large-scale experimental studies on HAWTs are then discussed, followed by a review of pertinent studies regarding the influence of blade tip geometry. The next section presents the aerodynamic design process concluding with the resulting design geometry and predicted performance of the baseline rotor (blades with standard tip). The structural design of the blade, including the tip exchange mechanism, is then presented with the blade fabrication outlined in great detail in an appendix. Next is the experimental design, apparatus, and procedure, followed by a presentation and discussion of the results.

Chapter 2

Background

2.1 Two-dimensional aerodynamics

Many wind turbine aerodynamic models assume two-dimensional (2D) flow over the blade and thus apply 2D airfoil data in their analyses. This is true of the design methodology used in this research project, and thus a brief review of airfoils and their 2D aerodynamic behaviour is now presented. An airfoil is the cross-sectional shape of a streamlined body as illustrated in figure 2.1. The chord length c is the length of the line joining the leading and trailing edges. The thickness t is the greatest thickness of the airfoil and is typically presented as a ratio (t/c) with respect to the chord length. When placed in a 2D velocity field, an airfoil will alter the streamlines of the field as depicted in figure 2.2. The presence of the airfoil introduces curvature to the freestream velocity (V_∞) field.

According to Bernoulli's theorem, which assumes ideal flow with no skin friction, a pressure deficit results above the airfoil which generates a force vector, F. This

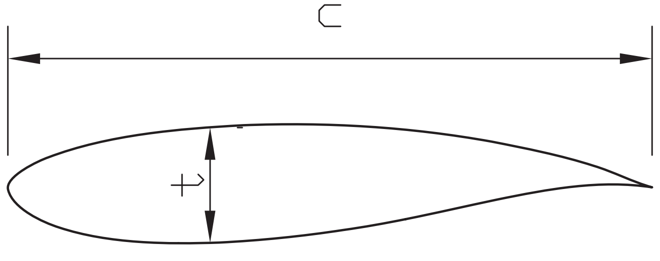

Figure 2.1: Example of an airfoil with dimensions labeled.

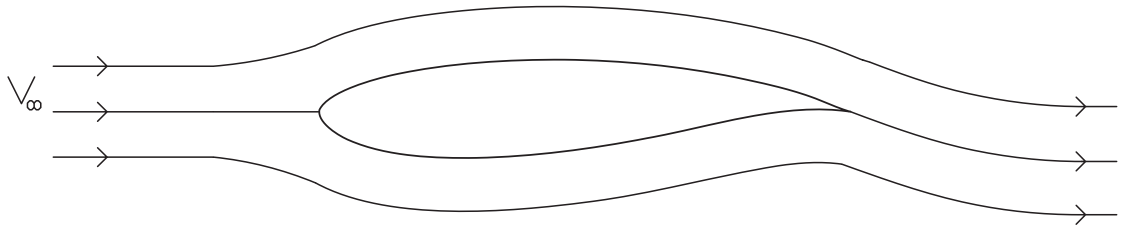

Figure 2.2: Ideal streamlines over an airfoil.

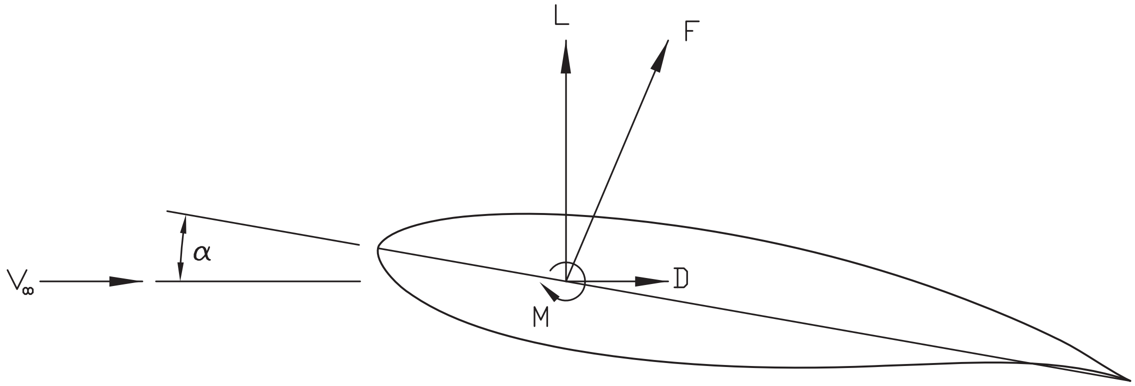

Figure 2.3: Forces on an airfoil. Adapted from Hansen [1].

force can be broken down into a component perpendicular to V_∞ known as lift (L) and one parallel to it known as drag (D). A pitching moment (M) is also generated as a result of F, and is typically defined at the quarter chord position ($c/4$) [1]. Figure 2.3 illustrates the relation between these parameters.

Lift, drag, and moment are often non-dimensionalized as C_l, C_d, and C_m and defined per unit length according to equation 2.1, equation 2.2, and equation 2.3, respectively:

$$C_l = \frac{L}{\frac{1}{2}\rho V_\infty^2 c} \tag{2.1}$$

$$C_d = \frac{D}{\frac{1}{2}\rho V_\infty^2 c} \tag{2.2}$$

$$C_m = \frac{M}{\frac{1}{2}\rho V_\infty^2 c^2} \tag{2.3}$$

C_l, C_d, and C_m are functions of the angle of attack (α), Reynolds number (Re), and Mach number (Ma) [1]. The parameter α is defined by the angle between V_∞ and the chord line. Re and Ma are defined by equation 2.4 and equation 2.5, respectively:

$$Re = \frac{cV_\infty}{\nu} \tag{2.4}$$

$$Ma = \frac{V_\infty}{c_s} \tag{2.5}$$

where ν is the kinematic viscosity and c_s is the speed of sound. Reynolds number is a measure of the ratio of inertial forces to viscous forces.

Airfoil performance data are typically presented in the C_l and C_d vs. α curves. An example is presented in figure 2.4. C_l increases linearly with α over the first portion of the curve. An airfoil begins to stall when α reaches a point such that the flow on the upper surface separates. At this point there is loss of lift and a drag rise also ensues. The onset of stall begins when the data start to deviate from the linear trend. Lift will then typically peak, seen at an angle of attack of 10^o in this case. Analytical methods are usually only able to accurately predict airfoil behaviour before stall, necessitating the gathering of experimental data to quantify post-stall performance.

This section has outlined the behaviour of airfoils in a purely two-dimensional manner, that is, assuming a wing of infinite span. A real wing has a finite span which introduces complications to the resulting flow field. These issues are discussed next.

2.2 Three-dimensional aerodynamics

As discussed above, the lift generated on a wing is the result of a pressure difference between the high and low pressure surfaces. When considering a finite wing, three-dimensional effects arise due to the natural phenomenon of pressure equalization at the wing tip. The higher pressure air on the lower surface tends to wrap around the tip to join the lower pressure air on the upper surface. This so-called “tip leakage” generates what are known as tip vortices. See figure 2.5 for a diagram of the flow

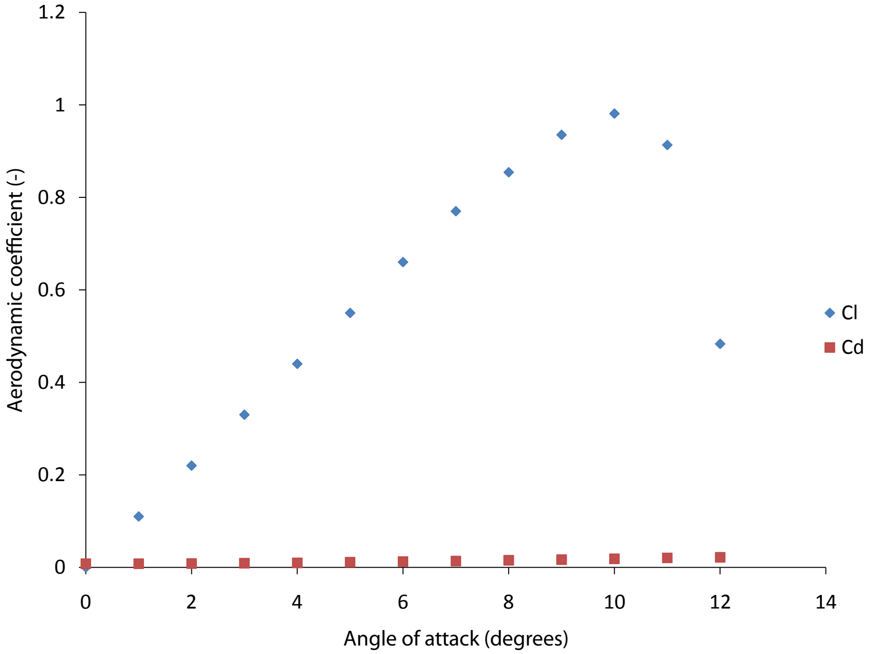

Figure 2.4: Example of lift and drag profiles vs. angle of attack. Adapted from Selig [9].

around the tips. The pressure equalization generates spanwise fluid motion, and as a result the streamlines over the wing are introduced to a spanwise velocity component. Over the low-pressure surface this component is directed away from the tip, whereas over the high-pressure surface it is directed towards the tip [10]. See figure 2.6 for an illustration of the deflection of the streamlines flowing past a 3D wing.

When the streamlines meet at the trailing edge of the wing, their opposing spanwise velocity components generate a vortex sheet that extends downstream with the freestream flow. The presence of this vortex system affects the flow past the wing and manifests itself as downwash. The downwash V_i is the total induced velocity from all vortices at a section of the wing [1] and it effectively deflects the freestream downwards behind the wing. This deflection is caused by the downward component of velocity that is added to the freestream flow by the vortex system. Figure 2.7 illustrates the effect of the velocity component w on the freestream velocity V_∞. The result of this vector sum is the effective velocity V_e. The geometric angle of attack α is defined with respect to V_∞ and the effective angle of attack α_e with respect to V_e. The angle α_i is the difference between α and α_e and is known as the induced

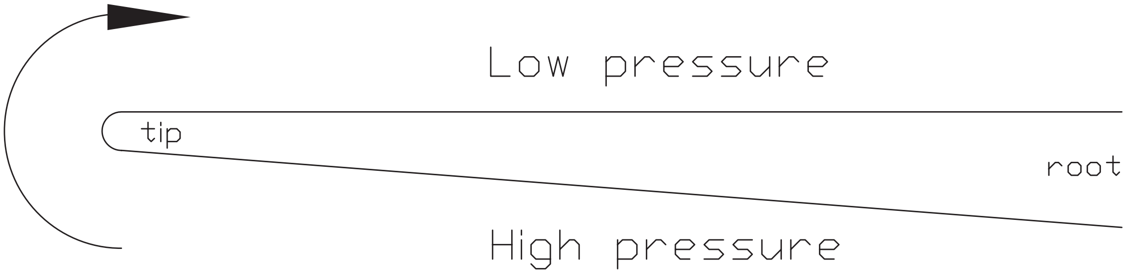

Figure 2.5: Flow leakage around a wing tip. Adapted from Anderson [10].

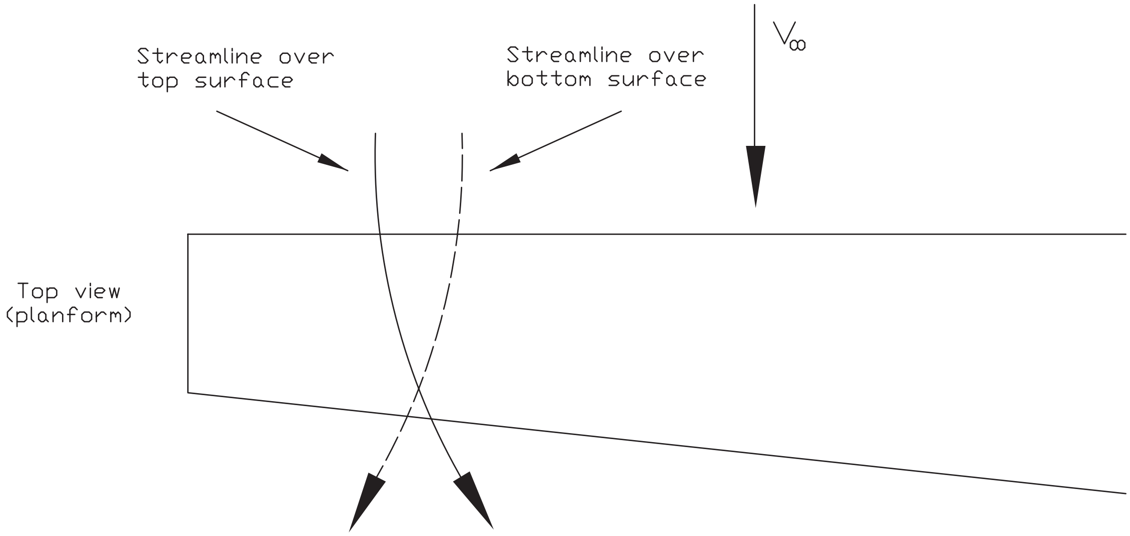

Figure 2.6: Streamlines over a wing deflected by 3D effects. Adapted from Anderson [10].

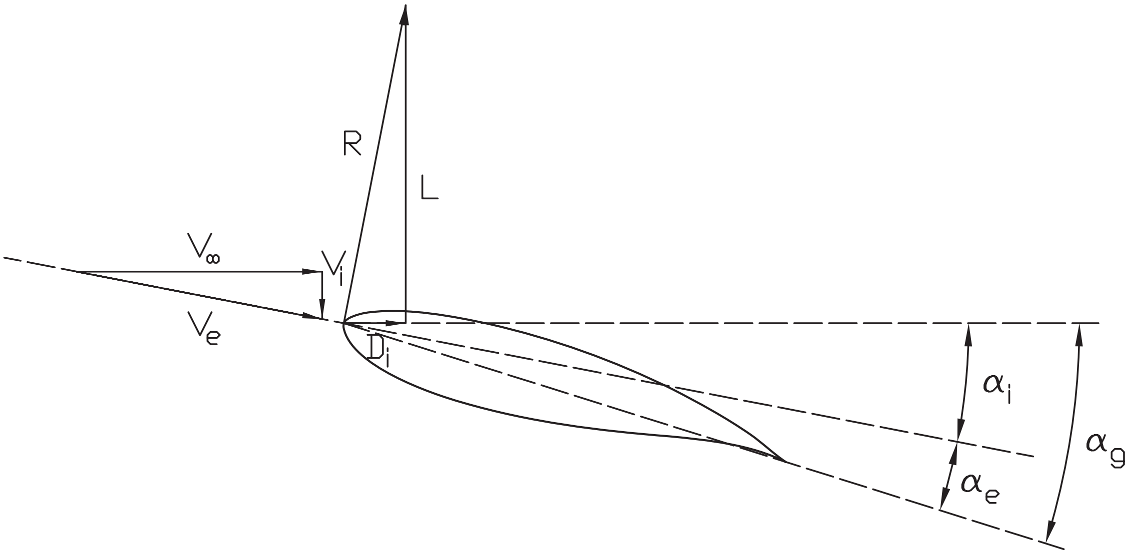

Figure 2.7: Effect of downwash on aerodynamic forces. Adapted from Hansen [1].

angle of attack. The deflection of the freestream velocity essentially tilts the original lift vector (R in figure 2.7) backwards, introducing a component parallel to V_∞ known as the induced drag, D_i. This reduces the magnitude of the lift vector L which is still, by definition, perpendicular to the incoming freestream velocity. D_i can be non-dimensionalized in the same way as L and D, and is defined in equation 2.6:

$$C_{d_i} = \frac{C_L^2}{\pi\,(AR)\,e} \tag{2.6}$$

where AR is the aspect ratio and e is the span efficiency of the wing. AR is defined in equation 2.7 [10]:

$$AR = \frac{b^2}{S} \tag{2.7}$$

where b is half the wing span and S is the planform area. A wing absent of 3D effects has an infinite span and hence infinite AR. As AR decreases, the effect of the vortex system on the flow over the wing increases [10]. The span efficiency e depends on the planform shape of the wing. The ideal case of $e = 1$ occurs for a wing with elliptical loading and hence an elliptical planform [10].

To summarize, in the 3D case the lift is reduced compared to a 2D wing at the same geometric angle of attack. This is due to the tilted lift vector which also introduces an additional component of drag. Both of these effects are a result of the downwash induced by the vortex system generated by the finite-length wing.

2.3 Horizontal axis wind turbine aerodynamics

To understand the rotor design portion of the research project it is important to be familiar with the underlying aerodynamic principles of HAWTs. This section briefly reviews the fundamental theory before outlining the model used in the design and the code used to implement the model and optimize the blade geometry.

2.3.1 General theory

The wind turbine rotor is responsible for extracting kinetic energy from the wind. The rotor can be represented as a permeable disc called an actuator disc which acts to extract pressure energy. Energy is only extracted from the mass of air that passes through the disc, thus a boundary can be drawn that encompasses this mass of air and defines a streamtube that extends both up and downstream. The presence of the rotor acts to slow the air down which results in an expansion of the streamtube since the mass flow rate is constant along the streamtube [2]. It can be shown that half of the axial velocity reduction in the streamtube occurs upstream of the disc and half downstream. While the velocity gradually decreases as it approaches and flows through the disc, the static pressure experiences a step drop across the plane of the disc [2] as illustrated in figure 2.8.

The magnitude of the velocity decrease is described by the axial flow induction factor, a, defined in equation 2.8 [2]:

$$V_{disc} = V_{\infty}(1 - a) \tag{2.8}$$

where V_{disc} is the axial velocity at the disc and V_{∞} is the incoming freestream velocity. The pressure difference across the disc imparts a change of momentum on the flow. It can be shown that the power P extracted from the air by the disc is [2]:

$$P = 2\rho A_d V_{\infty}^3 a(1 - a)^2 \tag{2.9}$$

where

$$A_d = \pi R^2 \tag{2.10}$$

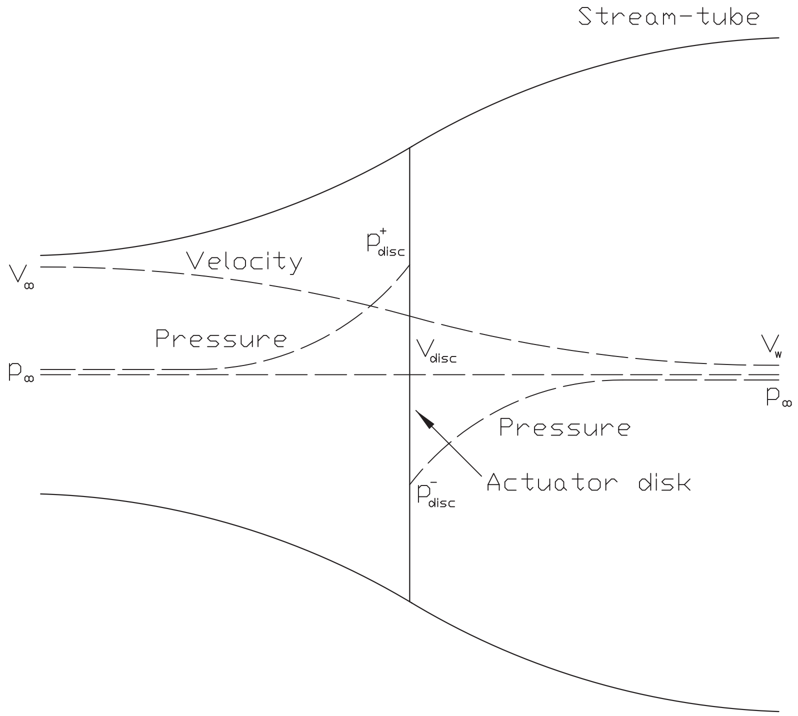

Figure 2.8: Energy extracting actuator disk and streamtube. Adapted from Burton et al. [2].

ρ is the air density and R is the disc radius. The power coefficient C_P is defined as [2]:

$$C_p = \frac{P}{\frac{1}{2}\rho A_d V_\infty^3} \tag{2.11}$$

where the denominator is equal to the total power available in a streamtube the size of the disc. The maximum theoretical value of C_p was derived by Betz [11] to be 0.593. This number is less than one due to downstream effects and because the streamtube is forced to expand as it approaches the disc. Thus, upstream where the wind speed is equal to V_∞, the streamtube cross-section is smaller than the rotor [2].

The thrust coefficient, C_T, gives the force applied on the disc due to the pressure drop and is given by [2]:

$$C_T = 4a(1-a). \tag{2.12}$$

For values of $a \geq 0.4$, the momentum theory is invalid and an empirical correction must be applied. This will be discussed in section 2.3.2.3.

When a rotor with a finite number of blades is used as the actuator disc, it imparts tangential velocity to the flow as it passes through the rotor. This tangential velocity is quantified by the angular induction factor a'. At the rotor plane, the induced angular velocity at radius r is $\Omega r a'$, while immediately downstream of the disc the tangential velocity settles to $2\Omega r a'$ [2]. The value Ω is the angular velocity of the rotor. Figure 2.9 provides an illustration of these relations.

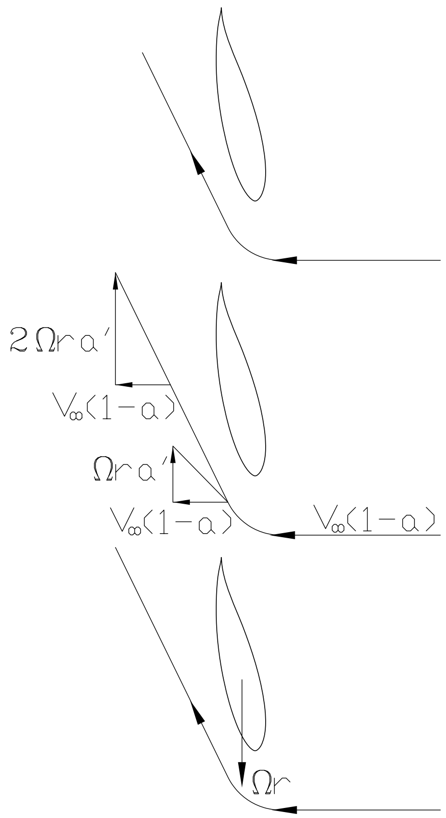

Figure 2.9: Effect of rotor on velocity field. Adapted from Burton et al. [2].

The angular velocity of the flow is produced in reaction to the rotor torque, which is equal to the rate of change of angular momentum. Power is the product of torque and angular velocity of the rotor, and, considering the disc as a collection of infinitesimal annular rings, each independent of the next, power derived from the pressure drop (equation 2.9) can be equated to power in terms of rotor torque. The power

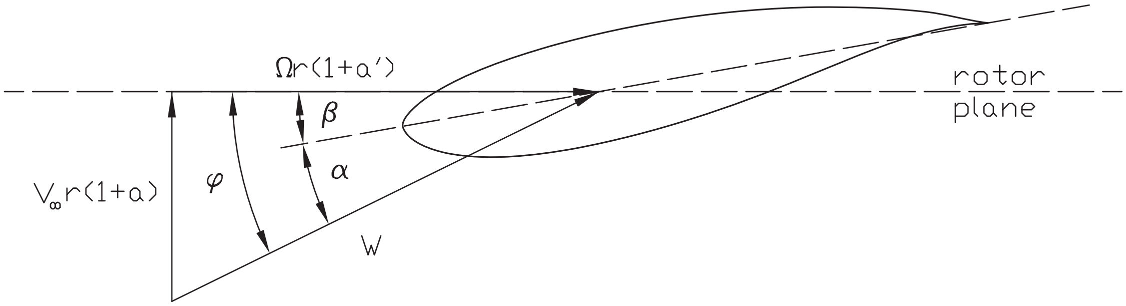

Figure 2.10: Blade element velocity triangle. Adapted from Burton et al. [2].

coefficient can then be derived for the elemental ring at radius r [2]:

$$\frac{d}{dr}C_p = 8(1-a)a'\lambda^2\left(\frac{r}{R}\right)^3 \tag{2.13}$$

where λ is known as the tip speed ratio, defined by:

$$\lambda = \frac{\Omega R}{V_\infty} \tag{2.14}$$

Knowing how a and a' vary radially, the power coefficient for the entire rotor can be found for a particular λ using equation 2.13 by summing the elemental contributions of each ring. In the case of a rotor with a finite number of blades, the contribution is not due to the entire ring but the blade elements incorporated in that ring.

2.3.2 Blade element momentum (BEM) theory

2.3.2.1 Fundamental theory

BEM extends actuator disk theory by incorporating the influence of the rotor blades. The effect of each elemental ring is determined by analyzing the aerodynamic response of the blades to the flow field in which they are immersed. In this method, the forces on the blade elements are calculated from airfoil data using the relative velocity, called W, at the rotor plane. The relative velocity vector W at a blade element at a particular radial position depends on the wind speed, flow factors, and rotational speed of the rotor. With the C_l and C_d data of each blade element available, the forces on the blades can be determined for given values of a and a' [2]. See figure 2.10 for a diagram of the velocity triangle and figure 2.11 for the force components at the blade.

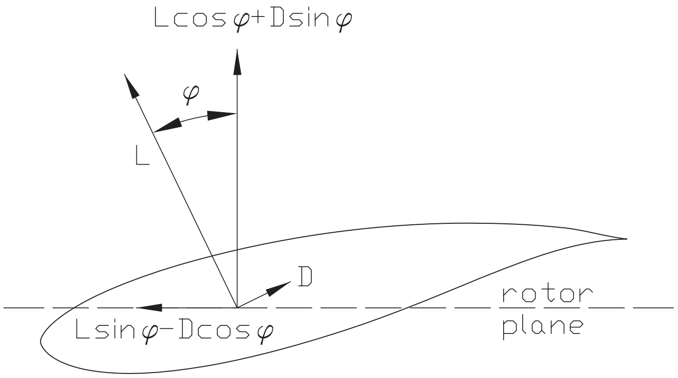

Figure 2.11: Blade element force components. Adapted from Hansen [1].

Note the inflow angle, called φ, which is the angle of the resultant velocity W with respect to the rotor plane. The local twist angle of the blade, called β, is also labeled. This is the setting of the particular blade element and is defined as the angle between the airfoil chord line and the plane of the disc. The angle β is set so as to achieve the desired α for the blade element. From figure 2.10 it can be deduced that:

$$\alpha = \varphi - \beta \tag{2.15}$$

The twist and chord distributions of a blade typically vary from root to tip. Figure 2.10 also demonstrates that:

$$tan\varphi = \frac{(1-a)V_\infty}{(1+a')\Omega r} \tag{2.16}$$

In figure 2.11, the lift and drag forces have been projected into components normal and tangential to the rotor plane. The tangential component contributes the torque while the normal component contributes the thrust loading on the rotor. Non-dimensionalizing with respect to $\frac{1}{2}\rho W^2 c$, and calling the normal and tangential components C_n and C_t, respectively, their equations become:

$$C_n = C_l cos\varphi + C_d sin\varphi \tag{2.17}$$

$$C_t = C_l sin\varphi - C_d cos\varphi \tag{2.18}$$

It can also be shown that [1]:

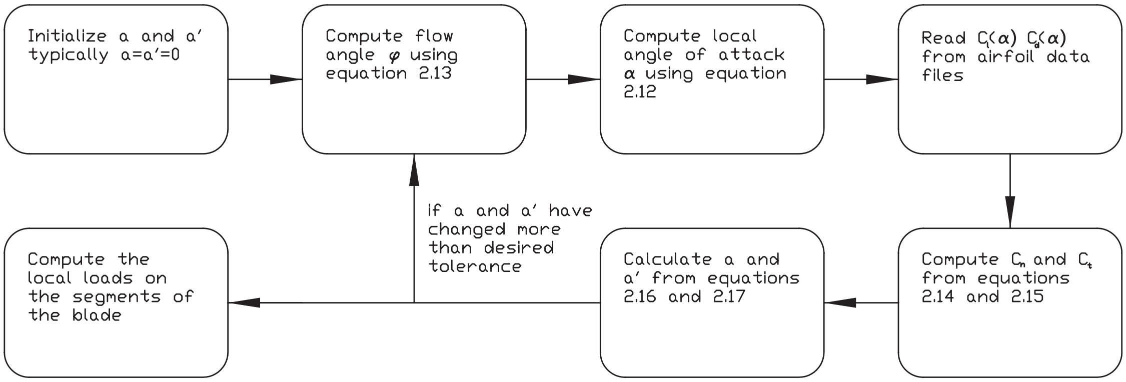

Figure 2.12: Flow chart outlining the BEM algorithm.

$$a = \frac{1}{\frac{4sin^2\varphi}{\sigma C_n} + 1} \tag{2.19}$$

and

$$a' = \frac{1}{\frac{4sin\varphi cos\varphi}{\sigma C_t} - 1} \tag{2.20}$$

where

$$\sigma(r) = \frac{c(r)N}{2\pi r}, \tag{2.21}$$

N is the number of blades and $\sigma(r)$ is the "solidity" at radius r. This parameter accounts for the finite number of blades. These are all of the equations that are required for the BEM algorithm. As alluded to above, all elements are assumed to be independent. This allows the BEM algorithm to be completed consecutively for each radial strip by executing the procedure outlined in figure 2.12 [1].

With the loads known for each element, the total power can be calculated. The torque at each element is found by multiplying the tangential force by the radius to that element. The rotor power is the sum of all elemental contributions of torque multiplied by the rotor angular velocity. The total thrust loading can also be found by summation of the elemental thrust contributions.

The method outlined in this section is not quite complete as it does not take into account the corrections for tip and root losses and high induction factor. These are discussed next.

2.3.2.2 Tip and root loss correction

Blade tip vortices act to reduce the angle of attack in the tip region as discussed in section 2.2, which reduces the power output of the rotor. The same issue arises at the blade root and corrections must be applied to account for these items [2]. A correction was derived by Prandtl and is applied to the induction factors during the BEM algorithm. The updated equations for the induction factors are hence [1]:

$$a = \frac{1}{\frac{4f(\mu)sin^2\varphi}{\sigma C_n} + 1} \tag{2.22}$$

and

$$a' = \frac{1}{\frac{4f(\mu)sin\varphi cos\varphi}{\sigma C_t} - 1} \tag{2.23}$$

where [2]

$$f(\mu) = f_T(\mu) f_R(\mu) \tag{2.24}$$

$$f_T(\mu) = \frac{2}{\pi} cos\left(e^{(N/2\mu)(1-\mu)\sqrt{1+(\lambda\mu)^2/(1-a)^2}}\right) \tag{2.25}$$

and [2]

$$f_R(\mu) = \frac{2}{\pi} cos\left(e^{-N/2(\mu-\mu_R/\mu)\sqrt{1+(\lambda\mu)^2/(1-a)^2}}\right) \tag{2.26}$$

where μ is the normalized radius $\frac{r}{R}$ and μ_R is the value of μ at the blade root. An extra step is therefore added after step 2 of the BEM computation to calculate $f(\mu)$. As well, equation 2.22 and 2.23 should be used in step 6 of the BEM computation rather than equations 2.19 and 2.20 [1].

2.3.2.3 Correction for high axial induction

Simple momentum theory breaks down for axial induction factor values greater than 0.4 [1]. A correction, proposed by Spera [12], is applied in step 6 of the BEM algorithm. It is applied as follows:

if $a \leq a_c$ equation 2.22 still applies
if $a > a_c$ equation 2.22 should be replaced with the following:

$$a = \frac{1}{2}\left[2 + K(1-2a_c) - \sqrt{(K(1-2a_c)+2)^2 + 4(Ka_c^2 - 1)}\right] \tag{2.27}$$

where

$$K = \frac{4f(\mu)sin^2\varphi}{\sigma C_n} \tag{2.28}$$

and $a_c = 0.2$. With these corrections applied, the typical BEM algorithm is complete.

2.3.2.4 PROPID blade design program

PROPID [13] is a freely-available multipoint inverse BEM-based design program for HAWTs. It improves on the classical method for wind turbine blade design known as the "design by analysis" approach. In the design by analysis method, candidate geometries are analyzed and the geometry is refined incrementally until the desired performance is reached [14].

PROPID makes use of the PROP [15, 16, 17, 18] code for analysis, but rather than having to use the design by analysis approach it enables the designer to specify desired aerodynamic (hence performance) characteristics from which the required geometry is determined. This allows the designer to quickly determine the optimum design for the desired optimization criteria. The aerodynamic characteristics can be single values or distributions along the blade. To perform a blade design using PROPID the user supplies an input file with design options and preferences as well as files containing the performance data of the airfoils to be used in the design. Input file options allow the designer to account for 3D flow losses, high axial induction factors, angular momentum, shaft tilt effects, and the atmospheric boundary layer profile as well as to customize the BEM details and apply airfoil data adjustments. The parameters describing the blade geometry are also required. Table 3.2 outlines the options specified in the input file.

There are many possible paths to follow in optimizing the geometry of the blade. If desired the user can make use of PROPID's multipoint design capability which allows the designer to specify performance characteristics for more than one operational point. The geometry, namely blade length, chord distribution, and twist distribution, are determined by the specifications in the input file. For example a maximum power

Option	Type	Notes
use tip loss model	yes/no	Prandtl
use hub loss model	yes/no	Prandtl
use brake state model	yes/no	Spera
use Viterna model	yes/no	Model for airfoil data
include angular momentum	yes/no	account for rotating wake
boundary layer wind exponent	float	shape of wind velocity profile
number of blade elements	int	spanwise elements (typically 10)
first element used in analysis	int	Typically 1
last segment used in analysis	int	Typically number of blade elements
print out data	yes/no	data generated during iterations
use shaft tilt effects on crossflow	yes/no	if rotor axis is tilted
air density	float	for power calculations
hub cutout	float	section occupied by hub/nacelle
hub height	float	height of rotor axis
number of blades	int	
rotor radius	float	distance from rotor axis to tip

Table 2.1: PROPID input file options. From Selig [13].

can be specified which constrains the blade length, and the chord and twist distributions can be determined based on desired axial induction factor and lift-to-drag ratio (L/D) distributions, respectively. Although extremely capable for blade design, PROPID does not allow the user to provide custom airfoil data over the entire operating range of the turbine, specifically at high angles of attack. For those designers who wish to use their own data at high angles of attack, another method must be found for performance analysis. For this reason PROPID was used to optimize the geometry, while the WT_Perf [19] code, discussed next, was used to produce the performance curves presented throughout.

2.3.2.5 WT_Perf rotor performance analysis code

WT_Perf is a wind turbine performance analysis code supplied by the National Wind Technology Center (NWTC) and developed by Buhl [19]. It uses BEM to analyze a given rotor design for any combination of wind speed, rotor speed, and blade pitch. It has the same set of options as PROPID, however there are no built in stall delay or post-stall models. This allows for the use of custom airfoil data which was desired in this case. Another advantage is that the rotor can be analyzed for an array of conditions (wind speed, rotor speed, and blade pitch) in a single analysis. Using PROPID each set of conditions would have to be analyzed in a separate analysis. It was the ability to use custom airfoil data, however, that made WT_Perf the code of choice for performance analysis.

2.3.3 Airfoil data correction and extension

During turbine operation, rotational effects along the blade will alter the blade's lift and drag performance as compared to 2D data provided by wind tunnel experiments or analytical methods. One result of this phenomena is a delay in blade stall which must be accounted for during rotor performance analysis. Once the data has been altered to account for stall delay it must be extended to cover the wide range of angles of attack seen by the blade during operation. Over the entire operating range of the turbine, blade angles of attack can span a range from roughly -15° to 50°, a range well beyond what is typically tested and available. To perform the design and evaluate the blade's performance using the BEM method, the designer must therefore generate adjusted and extended airfoil data files at angles of attack and Reynolds numbers spanning the operational range of the blade.

Airfoil data for the selected airfoils was only available for the pre-stall region, which is discussed further in section 3.1.3.1, hence only methods which could extend such data were used. This section will outline the Viterna method, a well-known method to apply such corrections, a more modern study by Tangler and Kocurek which refined the Viterna method, and the Aerodas model which was developed using empirical data and is the most recent of the three. Other available methods will also be mentioned but not elaborated upon.

2.3.3.1 Viterna method

The Viterna method [20] is an empirical model developed in the 1980s to help blade designers better predict wind turbine post-stall rotor power using the BEM method. Three sets of field test data were used to correct 2D aerodynamic coefficients such that, when used in a BEM analysis, they closely predicted the power curves of the turbines. Two data sets came from tests involving unique rotor configurations of the NASA Mod-0 turbine and one from the Danish Gedser turbine.

This model requires 2D airfoil data up to the 2D stall peak, which typically occurs at an angle of attack of no less than 10^o. To properly predict the power curves, Viterna [20] found that it was necessary to reduce the unstalled lift curve slope, increase the drag coefficient before stall, and decrease the drag coefficient after stall. Interestingly, it was found that the altered coefficients were approximately the same as those of a finite length wing with the same aspect ratio as the blade. To accomplish the required changes, the formulas for converting infinite length airfoil data to finite length must first be applied to the airfoil data below stall [20]:

$$C_L = C_{L_o} \tag{2.29}$$

$$C_D = C_{D_o} + \frac{C_L^2}{\pi AR}\left(1+\sigma_V\right) \tag{2.30}$$

$$\alpha = \alpha_o + \frac{57.3 C_L}{\pi AR}\left(1+\tau\right) \tag{2.31}$$

where o is a subscript denoting infinite aspect ratio data. The factors σ_V and τ are used to alter the span loading distribution from elliptical, however these values are typically small and can be assumed to be 0 [20]. Viterna also recommended disabling any tip/hub loss corrections since end effects are now accounted for in the airfoil data.

The second part of the method models the airfoil data from stall to 90^o. Assuming the shaft power after stall is constant, the following equations were derived [20]:

$$C_L = A_1 sin2\alpha + A_2\frac{cos^2\alpha}{sin\alpha} \tag{2.32}$$

$$C_D = B_1 sin^2\alpha + B_2 cos\alpha \tag{2.33}$$

where

$$A_1 = \frac{C_{D_{max}}}{2} \tag{2.34}$$

$$A_2 = (C_{L_s} - C_{D_{max}} sin\alpha_s cos\alpha_s)\,\frac{sin\alpha_s}{cos^2\alpha_s} \tag{2.35}$$

$$B_1 = C_{D_{max}} \tag{2.36}$$

$$B_2 = \frac{C_{D_s} - C_{D_{max}} sin^2\alpha_s}{cos\alpha_s} \tag{2.37}$$

$$C_{D_{max}} = 1.11 + 0.018AR. \tag{2.38}$$

A_2 and B_2 are solved using the values at the 2D stall angle, hence the subscript s is used to denote values at that point. For aspect ratios greater than 50, $C_{D_{max}}$ remains constant at 2.01. The main advantage of this model is that it can be used to produce airfoil data at angles of attack beyond stall even without the corresponding 2D coefficients. A more recent study by Tangler and Kocurek [21] evaluated the Viterna method and provided some recommendations.

2.3.3.2 Refined method of Tangler and Kocurek

The 2004 NREL paper by Tangler and Kocurek [21] provided great insight into the stall delay and post-stall behaviour of an operating wind turbine rotor. In this study the NREL UAE Phase VI [22] experimental data was used to generate lift and drag coefficient vs. angle of attack data for the S809 airfoil. This study is outlined in detail in section 2.4.1.1. Since the data was gathered on an operational rotating turbine, it was inherent that these data sets included rotational effects and spanned the full angle of attack range. Tangler and Kocurek used this data to evaluate the Viterna model and provide some recommendations as to how to use it to produce more accurate power curve predictions. According to the experimental data, the blade's L/D matched that of a flat plate beyond 20° angle of attack. Due to these findings, Tangler and Kocurek argued that Viterna's model should not be applied from the 2D stall peak (which for the S809 is 15°) but from the angle of attack at which the experimental C_L/C_D (L/D) matches that of the flat plate model; in this case 20^o.

This ensures that the aerodynamic coefficients from that point on satisfy flat plate theory and hence the experimental results. Evidence of stall-delay, also known as rotational augmentation, was also found. This phenomenon manifests itself in the near- and post-2D-stall regime, as can be seen in figure 2.13.

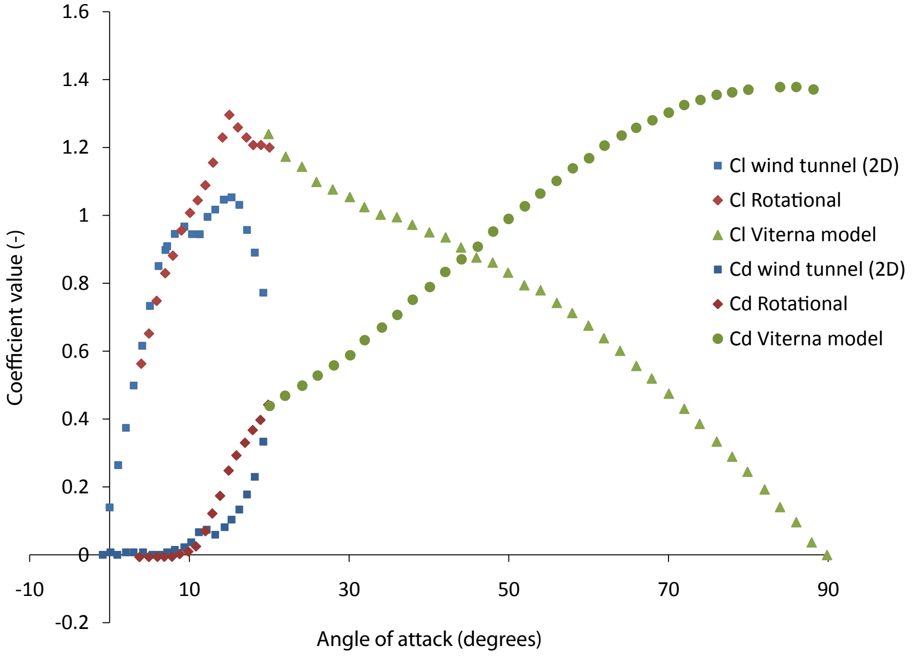

Figure 2.13: S809 2D and rotational airfoil data. Adapted from Tangler and Kocurek [21].

It can be seen that the experimental 3D lift and drag coefficients deviate from the 2D data beginning at roughly 10°, where the 2D curve shows evidence of the onset of stall. Beyond this point, the 3D lift coefficient continues to rise until it reaches a peak above the 2D stall value at 15°. The lift coefficient then decreases and meets the Viterna model at 20°. The drag coefficient, meanwhile, also increases above the 2D value and meets the Viterna model at 20°. One conclusion is thus that 2D airfoil data is valid in the range below the onset of 2D stall. As for the region from 2D stall to 20°, Tangler and Kocurek used the experimentally derived coefficients over that range, as they were fortunate enough to have such data at their disposal. Their input files to the BEM model thus consisted of 2D airfoil data to the onset of stall at 10^o, experimentally derived coefficients from 10^o to 20^o, and the Viterna model

Parameter	Description
A0	angle of attack at zero 2D lift (deg)
t/c	airfoil thickness to chord ratio
ACL1’	angle of attack at maximum pre-stall 2D lift (deg)
CL1max’	maximum pre-stall 2D lift coefficient; at $\alpha = ACL1'$
S1’	slope of linear segment of pre-stall lift curve (1/deg)
CD0	minimum 2D drag coefficient; at $\alpha = A0$; for all aspect ratios
ACD1’	angle of attack at maximum pre-stall 2D drag (deg)
CD1max’	maximum pre-stall 2D drag coefficient; at $\alpha = ACD1'$

Table 2.2: Input parameters for Aerodas model. Adapted from Spera [23].

beyond. Final recommendations from Tangler and Kocurek were to leave the tip/hub loss models activated during the BEM algorithm, as this provided better agreement with experimental data, and that the blade AR, used in the Viterna equations, should be defined as the blade length divided by the blade chord at 80% radius.

2.3.3.3 Aerodas model

The Aerodas model [23] was developed to enable the generation of the extended airfoil data required for wind turbine and wind tunnel fan performance prediction using only the limited airfoil data typically available. To use this method, the reference 2D airfoil data must include the stall peak, which occurs at an angle of attack of 10^o for the sample provided in figure 2.4. The study used an empirical approach whereby a broad range of test data was used to develop equations for lift and drag over the full range required. Airfoil data is divided into two distinct regions called the pre-stall and post-stall regimes, for which unique equations are provided for both the lift and drag. Unlike previous models, post-stall airfoil performance is not assumed to follow that of a flat plate hence new equations are presented for that region. Validation of the model was performed for 14 different airfoils of various aspect ratios. The Aerodas model was found to predict post-stall lift and drag coefficients more accurately than other available models, including the flat plate. The method was also used to predict the performance of the NREL UAE Phase VI blade, for which very acceptable results were obtained.

The model requires seven input parameters for a given airfoil. These are extracted from the available 2D airfoil data and are outlined in table 2.2 with short descriptions.

The airfoil data is then generated using the equations outlined next. The pre-stall lift is called $CL1$ and the post-stall lift is called $CL2$.

for $\alpha \geq A0$

$$CL1 = S1(\alpha - A0) - RCL1 \left(\frac{\alpha - A0}{ACL1 - A0} \right)^{N1} \tag{2.39}$$

for $\alpha < A0$

$$CL1 = S1(\alpha - A0) + RCL1 \left(\frac{A0 - \alpha}{ACL1 - A0} \right)^{N1} \tag{2.40}$$

where

$$S1 = \frac{S1'}{1 + 18.2S1'AR^{-0.9}} \tag{2.41}$$

$$RCL1 = S1(ACL1 - A0) - CL1_{max} \tag{2.42}$$

$$ACL1 = ACL1' + 18.2CL1'_{max}AR^{-0.9} \tag{2.43}$$

$$CL1_{max} = CL1'_{max} \left\{ 0.67 + 0.33exp \left[- \left(\frac{4.0}{AR} \right)^2 \right] \right\} \tag{2.44}$$

$$N1 = 1 + CL1_{max}/RCL1 \tag{2.45}$$

and

$$AR = 2(R_{tip} - R_h)/c_m \tag{2.46}$$

where R_{tip} is the tip radius, R_m is the mean radius, and c_m is the chord at the mean radius. The mean radius is defined as the radius at which half of the swept area of the rotor is enclosed. The lift coefficient in the post-stall regime is defined as follows:

for $0 < \alpha < ACL1$

$$CL2 = 0 \tag{2.47}$$

for $ACL1 \leq \alpha \leq 92.0$

$$CL2 = -0.032(\alpha - 92.0) - RCL2 \left(\frac{92.0 - \alpha}{51.0} \right)^{N2} \tag{2.48}$$

for $\alpha > 92.0$

$$CL2 = -0.032(\alpha - 92.0) - RCL2 \left(\frac{\alpha - 92.0}{51.0} \right)^{N2} \tag{2.49}$$

where

$$RCL2 = 1.632 - CL2_{max} \tag{2.50}$$

$$N2 = 1 + CL2_{max}/RCL2 \tag{2.51}$$

$$CL2_{max} = F1F2 \tag{2.52}$$

$$F1 = 1.190 \left(1.0 - \left(\frac{t}{c} \right)^2 \right) \tag{2.53}$$

$$F2 = 0.65 + 0.35exp\left[- (9.0/AR)^{2.3} \right] \tag{2.54}$$

The drag in the pre- and post-stall region are called $CD1$ and $CD2$, respectively. They are defined as follows:

for $2A0 - ACD1 \leq \alpha \leq ACD1$

$$CD1 = CD0 + (CD1_{max} - CD0) \left(\frac{\alpha - A0}{ACD1 - A0} \right)^m \tag{2.55}$$

where

$$ACD1 = ACD1' + 18.2CL1'_{max}AR^{-0.9} \tag{2.56}$$

$$CD1_{max} = CD1_{max'} + 0.280CL1^2_{max}AR^{-0.9} \tag{2.57}$$

The pre-stall drag (equation 2.55) is commonly defined as a quadratic equation with $m = 2.0$, although an exponent greater than 2.0 is sometimes appropriate.

for $\alpha \geq ACD1$

$$CD2 = CD1_{max} + (CD2_{max} - CD1_{max})\, sin \left(\frac{90 - \alpha}{90 - ACD1} * 90 \right) \tag{2.58}$$

where

$$CD2_{max} = G1G2 \tag{2.59}$$

$$G1 = 2.3exp\left(-\left(0.65\left(\frac{t}{c}\right)\right)^{0.9}\right) \tag{2.60}$$

$$G2 = 0.52 + 0.48exp\left[-\left(6.5/AR\right)^{1.1}\right] \tag{2.61}$$

2.3.3.4 Other models

Several other models have been proposed to correct 2D airfoil data to account for rotational effects. Some examples are the methods of Snel et al. [24], Chaviaropoulos and Hansen [25], Raj [26], Bak et al. [27], Lindenburg [28], and Corrigan and Shillings [29]. None of these models were pursued in this case as they all require 2D airfoil data spanning the operational range of angles of attack of the turbine. As mentioned before, this data is not available for the series of airfoils selected in this case.

2.4 Related work

In this section, studies related to the experimental phase of the project will be discussed. As will be outlined later, the experimental phase of this project involved characterizing the performance of the baseline rotor (having blades with standard tips) followed by that with each of the two different winglet designs. In this research, performance is assessed only by measurement of the power generation characteristics of the rotor, hence only studies that produced this type of results are presented.

2.4.1 Comparison of rotor performance to prediction

The two most important curves used to characterize rotor performance are the power vs. wind speed and power coefficient vs. tip speed ratio curves. The typical shapes of these curves for a stall-regulated three-bladed HAWT are shown in figure 2.14 and figure 2.15. The initial linear section of the power curve is the most predictable since the flow is still mostly attached and performance can be estimated using widely-available 2D airfoil data. The blade begins to stall prior to the first peak making the performance significantly more difficult to estimate for the remainder of the curve. The power coefficient curve presents the same data as the power curve only it is non-dimensionalized allowing the performance of different sized turbines to be compared. For a constant speed turbine, the right side of this curve corresponds to the lowest wind speed on the power curve, and wind speed increases with decreasing tip speed ratio. Predicted and actual performance data can be plotted on these axes to compare model accuracy.

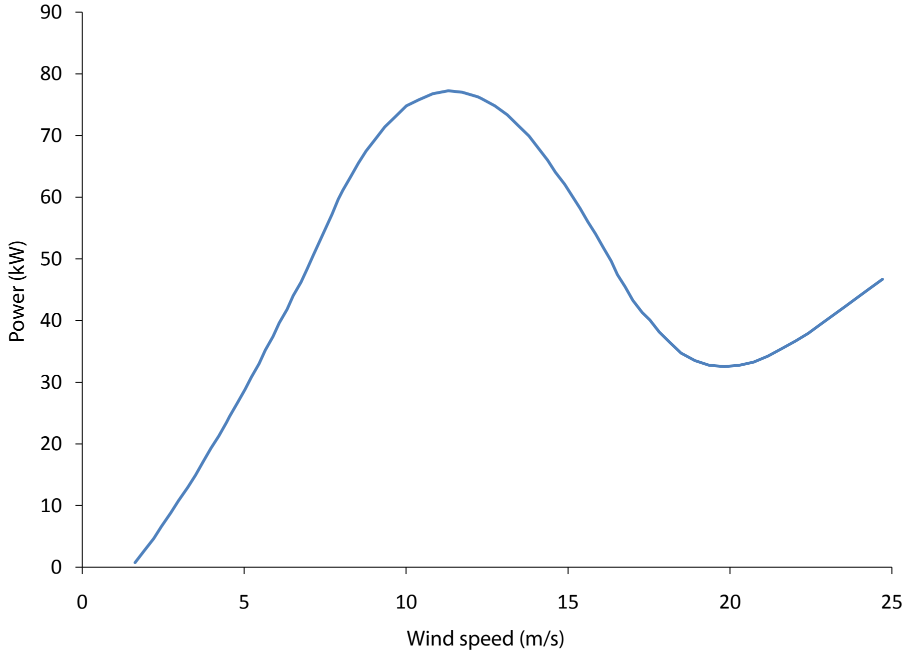

Figure 2.14: Example power curve of a stall-regulated wind turbine. Adapted from Burton et al. [2].

Since the initiation of serious research into wind turbine rotor aerodynamic design and testing in the 1980s there have been many studies focusing on the comparison of actual rotor performance to that predicted by models during the design phase. Due to the large size of even low power wind turbines, most studies of this type have been performed outside in uncontrolled atmospheric wind conditions. The international research community eventually realized, however, that the outdoor flow field was too complex to draw reliable conclusions due to rapid variations in wind speed, direction, turbulence, and shear, among other variables. It was thus decided that comprehensive studies in controlled conditions were required in order to quantify the response of a wind turbine rotor to known inflow conditions [30]. To date there have been two such detailed, exhaustive studies performed in controlled conditions, that is, in large-scale wind tunnels.

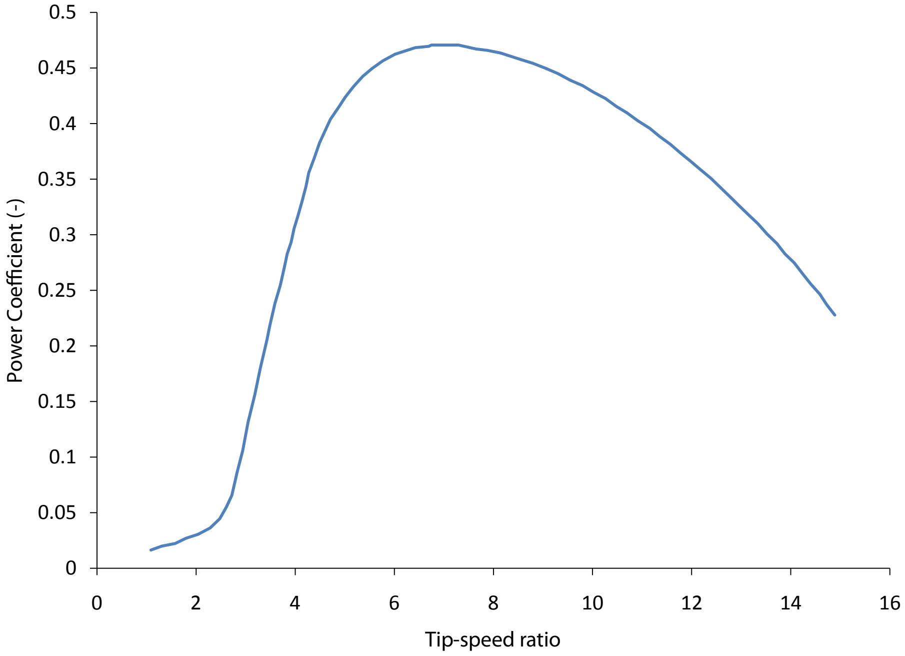

Figure 2.15: Example power-coefficient curve of a stall-regulated wind turbine. Adapted from Burton et al. [2].

2.4.1.1 NREL Unsteady Aerodynamics Experiment (UAE) Phase VI

The first of the two well-known studies was the NREL Unsteady Aerodynamics Experiment (UAE) Phase VI which was completed in May 2000. This experiment was performed using a 10 m diameter turbine in the NASA-Ames 24.4 m x 36.6 m wind tunnel. See table 2.3 for the specifications of the wind turbine used.

The NASA-Ames tunnel is the largest in the world and using six 18 000 hp fans [22] this facility can produce wind speeds speeds from 5 m/s to 50 m/s with a stream wise turbulence of no more than 0.5%. Data was gathered at 1700 different test conditions over a three-week period [30]. See figure 2.16 for a picture of the turbine mounted in the tunnel. This experiment produced a wealth of information to the international scientific community and it is being used to help researchers enhance and validate models which previously had no such experimental data with which to compare.

Of interest in this context is the power curve and how it compares to various model predictions. Soon after gathering the data a blind comparison test was ex-

Parameter	Specification
Number of blades	2
Rotor diameter (m)	10.058
Hub height (m)	12.192
Rotational speed (rpm)	71.63 or 90
Cut-in wind speed (m/s)	6
Power regulation	stall
Rated power	19.8 kW
Rotor location	upwind or downwind
Blade airfoil	NREL S809
Planform	tapered and twisted

Table 2.3: Specifications of turbine used in NREL UAE Phase VI. Adapted from Simms et al. [31].

ecuted in which 30 experts from 18 organizations forming 16 groups were provided with the turbine geometry and operating conditions and were asked to predict the power curve for the simple case of zero rotor yaw. The diverse group was made up of an international assortment of industry, academic, and government organizations specializing in wind turbine performance and load modeling. It was divided into four basic modeling-tool categories: aeroelastic codes, performance codes, wake codes, and CFD (computational fluid dynamics) codes. The results were divided into the four different modeling-tool categories and thus there are four plots. They are displayed as power vs. wind speed in figure 2.17, figure 2.18, figure 2.19, and figure 2.20. Note that only the experimental data curve is labeled as the sources of the various model predictions were not provided.

It is clear that no particular group was able to predict the power curve with any certainty, and the uncertainty increases with wind speed. At 7 m/s power predictions ranged from 25% to 175% of the measured value. This was very surprising to the modelers since in this case the blade is not stalled at any location and thus performance should be easiest to predict. Meanwhile at 20 m/s, when the blade is stalled from the root to 80% radius, power predictions ranged from 30% to 250% of the measured value. In addition, modelers tended to over predict forces inboard and over predict them outboard, resulting in an offsetting effect which masked errors even further. The modelers agreed that the errors were likely due to different modeler assumptions on how to use the 2D airfoil data and extrapolate it to 3D [30]. These findings made it clear that predicting the power curve of a stall-regulated turbine is

Figure 2.16: UAE Phase VI turbine mounted in NASA Ames 24.4 m x 36.6 m wind tunnel. From Schreck et al. [32]).

not trivial. Six years later, a similar study was completed called the Model Rotor Experiment in Controlled Conditions (MEXICO).

2.4.1.2 Model Rotor Experiment in Controlled Conditions (MEXICO)

The MEXICO project was coordinated by the Energy Research Center of the Netherlands (ECN) and involved collaboration between eight research labs spread throughout the Netherlands, Israel, Denmark, Sweden, and Greece [33].

The experiments were executed in December 2006 at the LLF (Large Scale Low Speed) wind tunnel of the German Dutch Wind Tunnel Facilities (DNW). This is the largest tunnel in the European Union and is located in North East Polder in the Netherlands. The measurements were gathered with the 9.5 m x 9.5 m open test section of the LLF where the flow is blowing from a nozzle to a collector and there is a closed loop between the collector and nozzle. The turbine was a 4.5 m diameter model designed specifically for this experiment [33]. See figure 2.21 for a photo of

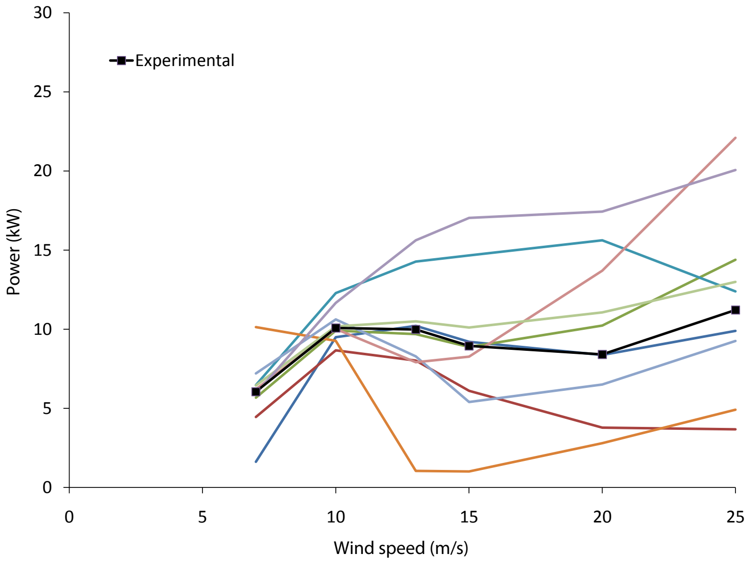

Figure 2.17: Power curve predictions from UAE blind test - aeroelastic codes. Adapted from Simms et al. [30].

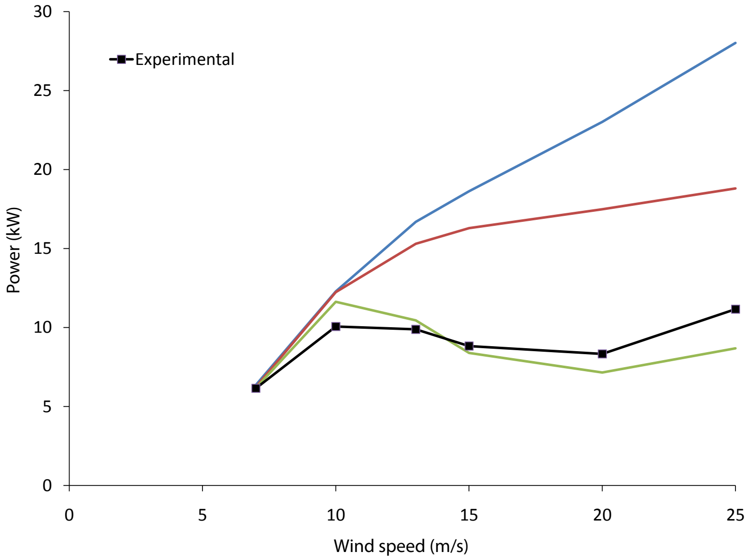

Figure 2.18: Power curve predictions from UAE blind test - performance codes. Adapted from Simms et al. [30].

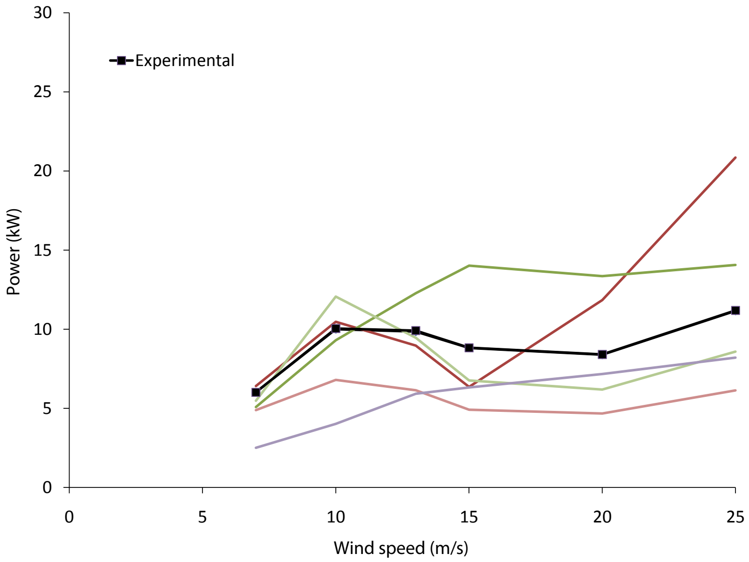

Figure 2.19: Power curve predictions from UAE blind test - wake codes. Adapted from Simms et al. [30].

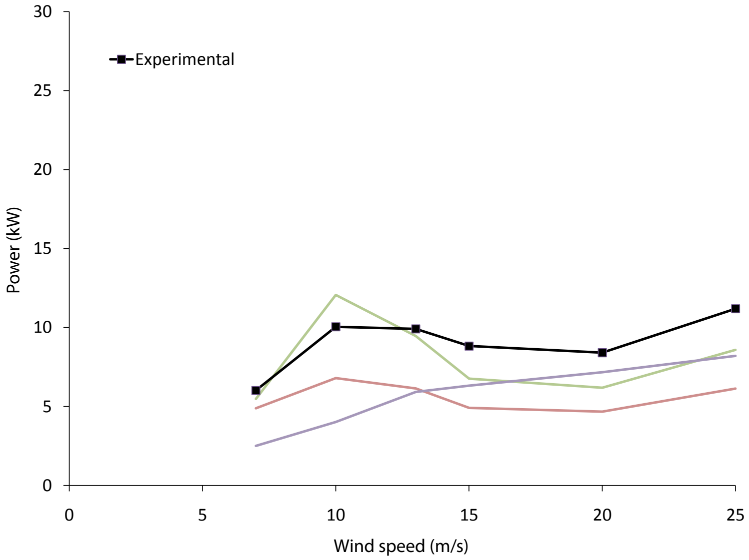

Figure 2.20: Power curve predictions from UAE blind test - CFD codes. Adapted from Simms et al. [30].

the turbine mounted in the tunnel and table 2.4 for the specifications of the research turbine.

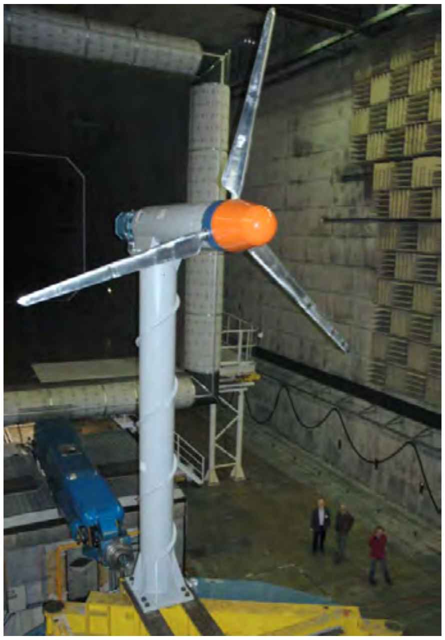

Figure 2.21: MEXICO turbine mounted in DNW LLF wind tunnel. From Schreck et al. [32].

The result of interest in this case is again the comparison of predicted performance to that determined experimentally. This is presented in figure 2.22 this time in the form of $C_p - \lambda$.

The $C_p - \lambda$ curve was predicted using the BEM method. It can be seen that the prediction follows the trend of the experimental result but there are some discrepancies. Below tip-speed ratios of 5 the code under predicts, while from 6 to 8 it over predicts. At tip-speed ratios greater than 9 the prediction is fairly close to the experimental result. This is surely related to the fact that at higher tip-speed ratios the flow over the blade is attached and therefore the performance is easier to predict.

Parameter	Specification
Number of blades	3
Diameter (m)	4.5
Rotor speed (rpm)	424.5, 324.5
Airfoils	root: DU 91-W2-250 mid-span: RISØ A1-21 outer part: NACA 64-418
Blade shape	twisted and tapered
Blade pitch	yes, quick pitch

Table 2.4: MEXICO research turbine specifications. Adapted from Schreck et al. [32].

2.5 Effect of blade tip geometry

Considering the goal of this research project was to evaluate the effect of alternative blade tip designs, it is essential to understand the conditions at the tip as well as previous efforts aimed at improving the blade tip design.

Three-dimensional effects are an ever-present reality on real wings, as described in section 2.2, and rotating wings such as wind turbine blades are not immune. It is for this reason that tip and root losses must be accounted for when analyzing the aerodynamics, as mentioned in section 2.3.2.2. As described earlier, the effect of three-dimensionality is the production of a tip vortex that reduces the magnitude of the lift and introduces an additional drag component, D_i, called the induced drag. What has yet to be addressed are the approaches that have been taken to reduce such losses. The majority of historical efforts into understanding and mitigating wing tip losses have been understandably directed at aircraft wings, and the consensus has always been that altering the geometry of the tip in one way or another can change the effect of tip vortices. A wealth of different planar and non-planar wing tip designs have been presented over the years. This study only explored the effect of non-planar tips and thus this section will focus solely on studies of such designs.

2.5.1 Non-planar tips

The basic justification for a non-planar wing tip is to reduce the strength of the tip vortex and the resulting lift and drag penalties. As early as 1897 a patent was obtained by Lanchester for a vertical surface at the wing tip, acknowledging the concept that a non-planar lifting surface should reduce the induced drag by inhibiting

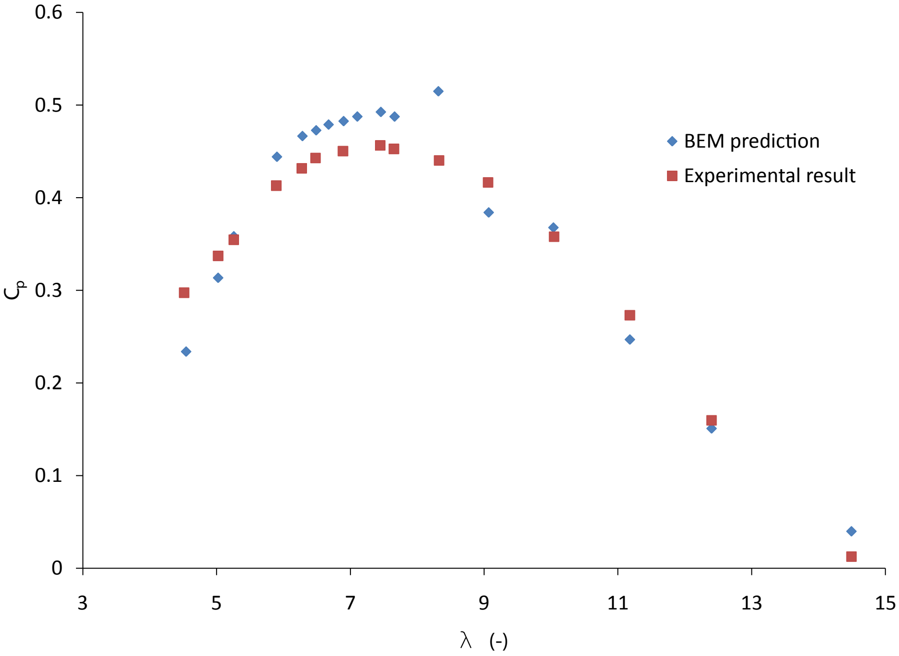

Figure 2.22: Comparison of predicted $C_p - \lambda$ to experimental result. Adapted from Micallef et al. [34].

the span wise flow induced by the tip vortex [35]. For decades, however, designers could not overcome the penalties associated with the added lifting surface. The penalties being the added viscous drag and increased loading on the wing requiring a heavier structure. In 1976 Whitcomb [35] determined that "to be fully effective the vertical surface at the tip must efficiently produce significant side forces." His work resulted in the first "winglets" which are streamlined vertical surfaces placed at the tip of the wing. Streamlining the surface using an airfoil shape produces "a vertical diffusion of the tip vortex flow at least just downstream of the tip. The large inward components of the vortex flow near the center of the vortex are substantially reduced while the small inward components in the region above the tip of the winglet are increased slightly. Thus these surfaces could be called vortex diffusers [35]." A modern winglet is depicted in figure 2.23 and is defined by the cant angle, height, twist, sweep, toe, and also the chord distribution or planform (rectangular, tapered, elliptical, etc.), airfoil, and location (pressure or suction side of wing).

The use of positive twist introduces what is known as wash-in, where as negative twist introduces wash-out. Washing in the winglet increases the angle of attack

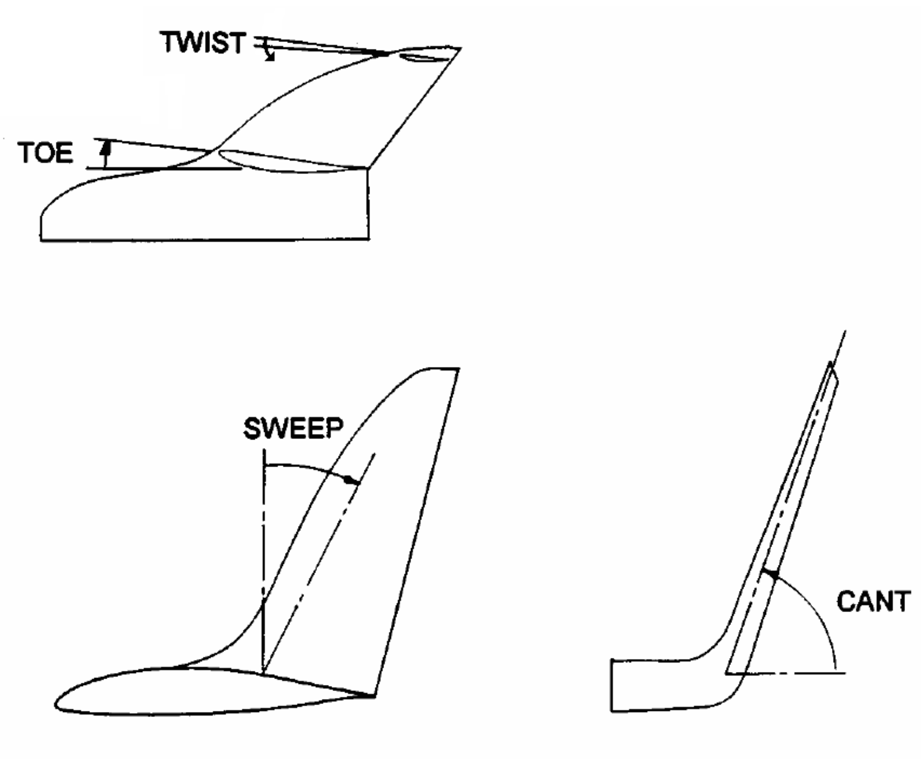

Figure 2.23: A modern winglet. All displacements shown are positive by convention. Adapted from Maughmer [36].

towards the tip while washing out reduces it. The combination of the toe and twist angle produces what will be called the setting angle. As illustrated in figure 2.24, the setting of a particular section of a winglet is the rotation of the section with respect to the tangent of the circle swept by the blade tip. This varies along the winglet height based on the root toe and tip twist of the winglet. A positive toe angle increases the setting while a positive twist decreases it.

One important point about winglets is that they can only be optimized for one particular operating point [36]. This is why they have become prevalent on commercial airliners. Such aircraft operate under extremely controlled conditions (cruise) for the majority of the time, allowing the winglet to be optimized for that set of conditions. Wind turbines, however, must operate under a wide range of wind speeds, which in turn subject the blade to a wide range of angles of attack. It is for this reason that the most applicable work on aircraft winglets in this context is that of Maughmer [36], which was focused on sailplane applications.

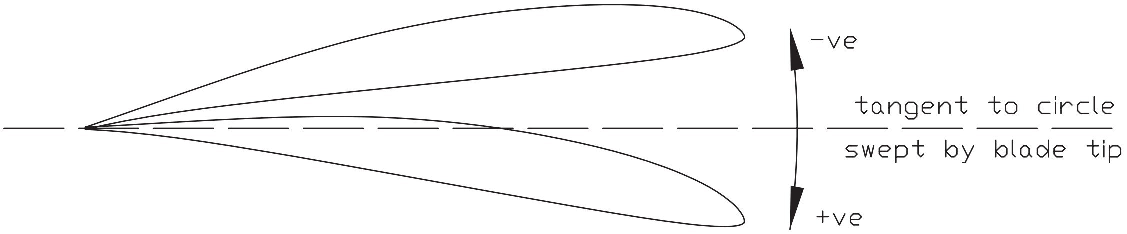

Figure 2.24: Illustration of winglet setting angle.

2.5.1.1 Work of Maughmer on sail plane winglets

A sailplane, also known as a glider, is a two-person aircraft designed for soaring. A typical glider has no engine and hence concerted efforts are made to achieve maximum aerodynamic efficiency. A sailplane has a broad operating envelope as it must be capable of performing efficiently while both climbing in thermals and soaring between them [36]. It thus has variable operating conditions like a wind turbine blade. As well, the Reynolds numbers encountered at the tip of a typical sailplane are similar to those of a small-scale wind turbine blade. Since the 1980s researchers at Pennsylvania State University, led by Professor Mark Maughmer, have been performing extensive experimental and analytical research on winglets for sailplanes.

Of great use in Maughmer's work are the guidelines issued to aspiring winglet designers, which were developed based on extensive modeling and flight testing which resulted in many successful winglet designs. Maughmer addressed the multitude of variables to be considered in designing a winglet; providing recommendations and valuable insight into their effects on winglet performance. The work of Maughmer will be used here to describe the effect of each of the multitude of variables used to describe a winglet. The following knowledge is of course based on sailplane winglets, but can be applied to wind turbines for the reasons stated previously.

Location and chord distribution Maughmer [36] mentions that winglets are best placed on the suction side of a wing as, according to free-wake simulations, placing them on the pressure side results in a contraction of the wake and a reduction in effectiveness. This is also in agreement with other studies that will be discussed later. Best practices for the selection of geometry are also discussed. The span wise chord distribution (planform) should be selected such that the loading on the winglet is near elliptical and the induced drag of the winglet itself is minimized. Hence, an elliptical planform is likely best.

Height, root chord and tip chord The selection of height, root chord, and tip chord must keep in mind the conflicting requirements of Reynolds number concerns and wetted-area penalty. Drag coefficients increase with decreasing Reynolds number, and Reynolds number is directly proportional to chord length. Greater chord lengths are therefore better with respect to Reynolds number considerations. However, to reduce gross drag, the wetted area of the winglet should be minimized. Wetted area is also directly dependent on the chord distribution in addition to the height. Thus an optimal design will maintain greater chord lengths to satisfy Reynolds number concerns while also keeping the wetted area within reason.

Twist and sweep The load distribution on the winglet is tailored by spanwise twist and sweep. One of these variables can be fixed since increasing sweep has the same effect on the load distribution as adding wash-in along the winglet. In their designs, twist was fixed at 2.6^o establishing wash-in. Ideally the sweep angle is determined iteratively by varying it until the stall pattern on the winglet is uniform in the span wise direction. It is also recommended to keep sweep angles below 40^o, otherwise cross-flow instabilities may be introduced that will cause the boundary layer to transition prematurely.

Toe and cant angle The toe angle controls the overall loading on the winglet as well as the overall effect on the load distribution of the wing due to the winglet. It is this parameter that causes winglets to only be truly optimal for one flight condition. This is because the angle of attack on the winglet is a function of the lift coefficient of the wing. The greater the toe angle, the greater the benefit at high wing lift coefficients. Increasing the toe angle, however, increases the penalty at low wing lift coefficients. It is therefore the determination of this angle that is most critical, as it will determine the performance over the entire operational envelope. Ideally the toe angle is chosen such that both the wing and winglet stall simultaneously, as there is no benefit in having the winglet carry load beyond that of the wing. In Maughmer's case, both the sweep and toe angles were initially determined by flight tests using tufts. As for cant angle, no recommendation was issued but all of their designs used an angle of 90^o [36].

Airfoil One final point of interest for this sailplane winglet program was the development of the PSU 94-097, a winglet airfoil specifically designed for sailplane applications [37]. It's drag polar is presented in figure 2.25. This airfoil would likely be a good candidate for small wind turbine applications for the reasons specified above.

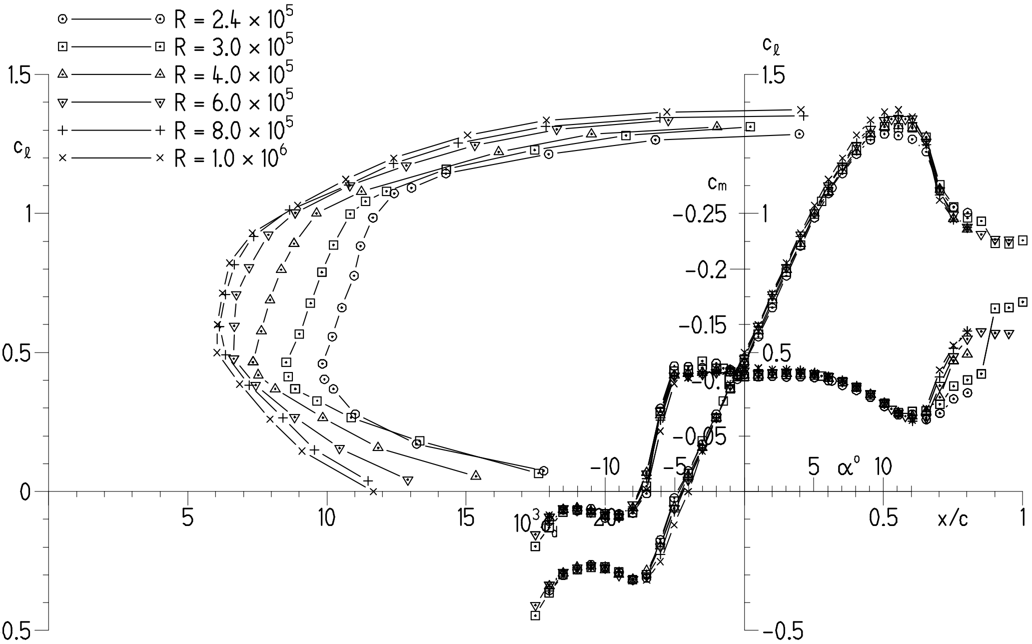

Figure 2.25: Performance characteristics of PSU 94-097. R=Reynolds number. From Maughmer et al. [37]).

Although much more limited than those on aircraft wings, efforts have been made to apply such devices to wind turbine blades.

2.5.1.2 Numerical studies on wind turbine winglets

The majority of published studies on wind turbine winglets have been numerical in nature. The consensus seems to be that it is possible to augment the power production of a turbine using winglets by means of a reduction in induced drag and hence greater torque. Due to the multitude of variables used to define a winglet, comparing studies involves considering not only the results but also the quantities used to define the winglet geometry and the operating conditions at the tip. Table 2.5 and table 2.6 provide an overview of the relevant studies and their results.

As can be deduced from the table, several approaches have been taken to analyze the effect of winglets on wind turbines. The winglet designs outlined differ greatly, but there are some general trends. All winglets are placed on the suction side, the tapered planform seems to be more popular than rectangular, and cant angles are generally agreed on at 90^o. Winglet heights typically vary from 1% to 5% of rotor radius, although the blades with lower Re_{tip} values both have heights of 10%. Sweep tends to be zero for the most part, while toe angle varies but does not exceed 5^o. The twist angle, meanwhile, varies widely from -2^o to 13^o.

The power augmentation, P_{aug}, defined as the percentage change in the maximum power coefficient, has been predicted to be as high as 8% and as low as 2%, depending on the scale of turbine. Smaller turbines with lower tip speeds can apparently achieve greater power augmentation because the additional viscous drag due to the added lifting surface is lower at lower tip speeds. This despite the fact that the reduced tip speed results in a lower Reynolds number and hence higher drag coefficients. T_{aug}, analogous to P_{aug} but relating to thrust, is seen to increase with P_{aug} which is not surprising as increased power production will inherently lead to increased thrust.

2.5.1.3 Experimental studies on wind turbine winglets

The only experimental investigation found on the effect of non-planar tips on wind turbine blades explored the effect of “tipvanes.” A tipvane is essentially a flat plate mounted at the blade tip. An extensive design and evaluation program started at Mie University in the late 1980s following van Holten’s [43] suggestion that tipvanes could be used to augment the mass flow through the rotor disc thus increasing the shaft power significantly. The most noteworthy study in this program was published in 2003 [6]. Investigations were undertaken using 2- and 3-bladed rotors having tapered and twisted blades with a length of 0.5 m to 0.65 m and maximum power coefficients of 0.45 to 0.49, respectively. The rotors were fitted with “Mie” type vanes which are tip vanes bent outwards as depicted in figure 2.26.

Experiments were performed in the open test section of a single return Gottingen type wind tunnel with a 3.6 m outlet diameter. The effect on power production of tipvanes having a height of 9% of radius was evaluated for variations of blade AR and tip Reynolds number (Re_{tip}). Aspect ratio varied from 6.2 to 8.2 and Re_{tip} from 1×10^5 to 2×10^5. Using tipvanes P_{aug} was found to be positive around the optimal tip speed ratio and negative elsewhere. These results are presented in figure 2.27.

Source and Year	Method	Winglet side	Blade length (m)	Blade AR	Re_{tip}	Planform
[38] 1998	Vortex lattice w/ free wake	suction	0.6	5.25	2.4×10^5	rectangular
[39] 2006	CFD	suction	NA	NA	NA	rectangular
[40] 2007	vortex lattice and free-wake lifting line	suction	30	14	4.4×10^6	tapered
[41] 2007	CFD	suction	MW -sized	NA	NA	tapered
[7] 2007	CFD and free wake lifting line	suction	63	15	5×10^6	tapered
[42] 2008	free-wake vortex-line	suction	46.2	NA	NA	NA
[8] 2008	CFD and free wake lifting line	suction	63	15	5×10^6	tapered
[5] 2009	vortex method based on Goldstein model - extension of Prandtl lifting line	suction	5	NA	8×10^5	NA

Table 2.5: Overview of numerical studies on wind turbine winglets.

Source and Year	Cant (^{o})	Height (%R)	Twist (^{o})	Sweep (^{o})	Toe (^{o})	Airfoil	P_{aug} (%)	T_{aug} (%)	$C_{p_{max}}$
[38] 1998	80	10	0	0	0	NACA 0012	8	8	.4
[39] 2006	90	1.5	-2	0	NA	NA	1.7	1.8	NA
[40] 2007	90	3 - 4	13	NA	5	Riso B118	2.9	3.1	.53
[41] 2007	90	4	4	0	NA	NA	2.77	3.55	NA
[7] 2007	90	2	NA	0	NA	Riso B-15	2.8	3.5	.53
[42] 2008	90	5.4	NA	0	NA	NA	2.6	NA	0.5
[8] 2008	90	1 - 4	0 - 8	30	0	Riso B-15	2.2 (h=2%)	4.0 (h=2%)	NA
[5] 2009	90	10	8	NA	1	S809	3.5	NA	0.35

Table 2.6: Overview of numerical studies on wind turbine winglets (continued).

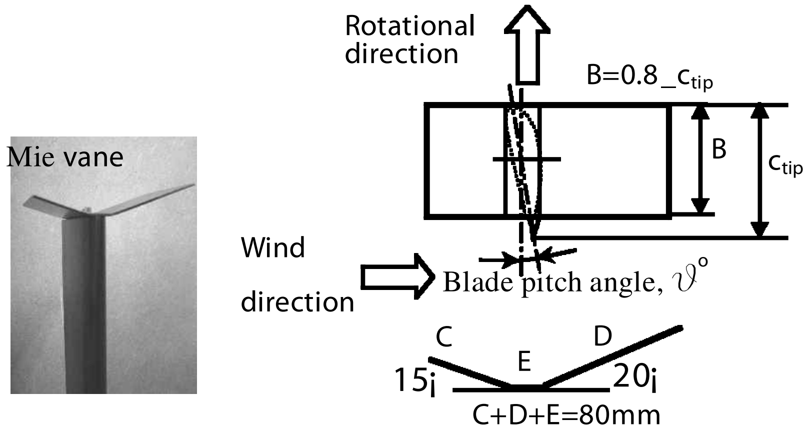

Figure 2.26: “Mie” type tip vanes. From Shimizu et al. [6].

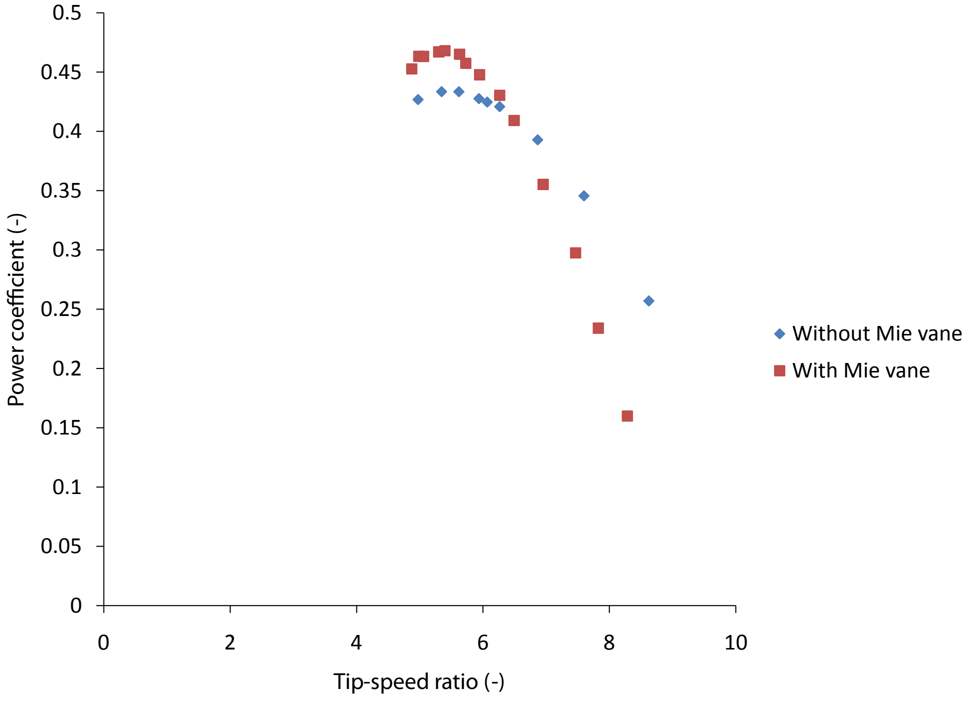

Figure 2.27: Sample power coefficient vs. tip speed ratio curve from Mie University study (two-bladed case). Adapted from Shimizu et al. [6].

In the three-bladed case, peak power augmentation reached 9% at lower aspect ratios and Reynolds numbers and decreased to 4 % as those quantities increased. It is encouraging that these experimental results agree with the trends of the numerical studies outlined above. These results can thus provide a good basis for comparison for the experimental results of the current study. The value of an increase in power on the order of a few percent is also of interest. To address this, the nature of the wind resource and the economics involved will be briefly discussed.

2.6 Wind resource and economics

The wind resource at a given site is typically described by a probability distribution. An example of such a distribution is presented in figure 2.28 for a site with an annual average wind speed of 6 m/s.

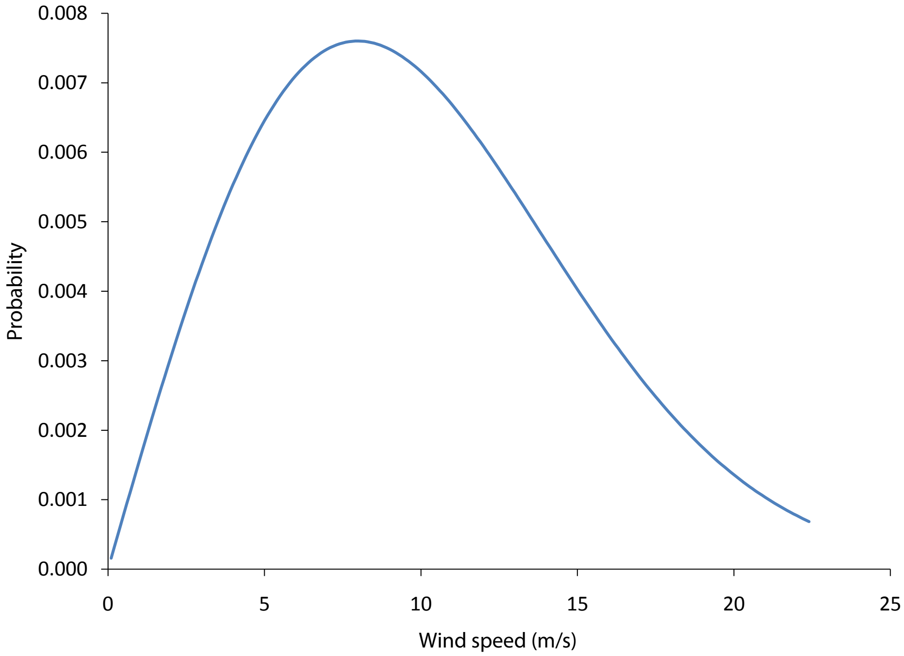

Figure 2.28: Sample wind speed probability distribution.

The shape of the curve is that of a Weibull distribution, and the most likely wind speed is indicated by the peak of the curve. The shape of the Weibull distribution is defined by the annual average wind speed at the site and the local topography [2].

Developers use the wind probability distribution to estimate the annual energy production (AEP) of a turbine. The AEP is used in the economic analysis to determine the feasibility of developing a site. It is possible to perform an economic analysis for a given site and turbine using the wind probability distribution and the power curve of the machine. Often developers are guaranteed a certain price per kWh of electricity produced by a wind turbine, which allows them to calculate the expected revenue per year. For example, the Government of Ontario has established a feed-in-tariff that guarantees wind turbine owners a return of $0.13/kWh [44].

Thus, the value of any improvements to the power curve of a turbine can be quantified by following such an approach.

Chapter 3

Aerodynamic design

This section will outline the methods by which the geometries of the blade and winglets were determined. It will first address the design constraints that had to be considered during the blade design, along with the methodology used to design the research blade, followed by the final geometry and predicted performance of the three-bladed rotor. The final section outlines the design of the two winglets tested in the study.

3.1 Blade Design

3.1.1 Design constraints

In performing the design, certain constraints had to be considered based on the specifications of the test facility. Specifically, air jet size, rotational speed of the rig, facility wind speed range, and maximum generator power all constrained the blade design. A detailed and exhaustive review of many wind tunnel experiments on HAWTs found that the median blockage ratio (based on rotor swept area) used in this type of experiment is 25% [45]. Using this finding, the maximum acceptable diameter for a rotor in the Wind Energy Research Facility, described in section 5.1, is 3.3 m. The design blade length was thus set to 1.6 m to account for the hub. In order to resolve small changes in performance, it was desirable to maximize power output and thus rotational speed. With this in mind, the design point speed was set to 200 revolutions per minute (*rpm*) so as not to operate at the rig's maximum of 240 *rpm*. The wind speed range in the facility is 0 to 11.1 m/s. In order for measurements to span the range of typical performance curves, the point of maximum efficiency (maximum

Figure 3.1: S83x airfoils. Geometry from Somers [46].

power coefficient) was set at a wind speed of 6.5 m/s. After the design was complete the predicted maximum power generation also had to be checked to ensure it did not exceed the generator maximum of 3.6 kW.

3.1.2 Airfoil selection

A wind turbine blade is defined by a distribution of cross-sectional blade stations which are blended together to form the full blade. Each station has a shape defined by the airfoil with a size defined by the chord length, and an orientation defined by the twist.

The first step in the design is the selection of the airfoils. If desired, multiple airfoils can be used along the span. In this case, the NREL S83X series was used [46]. These airfoils were designed specifically for wind turbines of 1 to 3 meter blade length. This series consists of three airfoils: the S833, S834, and S835. As recommended in the airfoil design report [46], the S833 was placed at 75% radius, the S834 at 95%, and the S835 at 40%. The S835 is used exclusively up to 40%, the S834 from 95% to the tip, and a linear blend of the airfoils is performed from 40% to 75% and 75% to 95%. See figure 3.1 for a view of the S83X series airfoils.

3.1.3 Airfoil performance data

As mentioned in section 2.3.3, 2D airfoil data must be corrected to account for rotational augmentation and extended to cover the operational range of angles of attack of a wind turbine. Based on calculated operational velocities as well as comparisons to similar sized turbines, the Reynolds numbers to be encountered by this blade were estimated based on the chord and relative velocity to vary between 1.0×10^5 and 2.0×10^5 depending on the radial location. Two-dimensional airfoil data was found spanning those Reynolds numbers in the airfoil design report [46]. The data was generated using the Eppler Airfoil Design and Analysis Code [47, 48], which has been thoroughly validated during the design, analysis, and experimental validation of other airfoils [49, 50, 51, 52, 53, 54]. The data provided by the report spans the angle of attack range from -4° to the onset of stall at roughly 7° and is provided for various blade surface roughnesses. In this case the data for a smooth blade was used. Another study [9] provided airfoil data up to 20°, but only for the S834. The design point of the rotor, which determines the blade geometry, is set such that each blade section is operating at maximum L/D. This point always occurs prior to 2D stall and it is well established that 2D data below stall is valid for wind turbine performance predictions [21]. Hence an optimal blade design can be produced without correcting and extending the airfoil data. As mentioned in section 2.3.2.1, however, having such two-dimensional airfoil data is not enough to predict rotor performance across the entire operating range. A method must therefore be chosen to correct and extend the airfoil data.

3.1.3.1 Correction and extension of S83X data

Two methods were used to correct and extend the S83X data. The first is a method that combines the Viterna model and the results of the study of Tangler and Kocurek. The other is based on the empirical Aerodas model.

Combined Viterna/Tangler and Kocurek method (VTK) To extend the S83X series airfoil data, the Viterna method [20], described in section 2.3.3.1, was altered as recommended in the paper by Tangler and Kocurek [21], discussed in section 2.3.3.2. This study provides very useful guidelines but has one drawback: it relies on experimentally derived 3D lift and drag coefficients from the onset of 2D stall to 20° angle of attack. In the case of the S83X series airfoils such data is not available. In the absence of such data, it was decided to model this region using the trends in the experimental data of Tangler and Kocurek [21]. This was deemed reasonable based on the fact that this blade had certain similarities. The aspect ratios of the UAE and research blade are 11 and 10.9, respectively. In addition, the airfoils used on the two blades were designed using the same methodology and with the same goals in mind, as they were both intended for use on wind turbine blades. It should be mentioned, however, that the Reynolds numbers encountered by the UAE blade were in the range of 2×10^6 whereas the research blade is expected to only encounter Reynolds numbers up to 2×10^5. A comparison of the 2D lift and drag data of the S83X series and S809 airfoils is provided in figure 3.2 and figure 3.3, respectively.

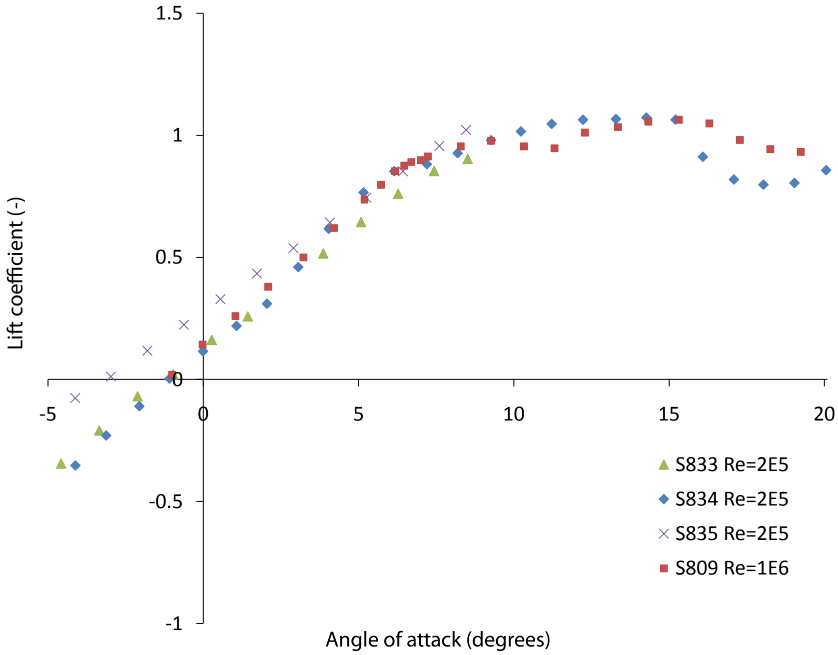

Figure 3.2: 2D lift data for S83X and S809 airfoils. Adapted from Somers [51] and Selig [9].

The comparison of the airfoil data of the S83X and S809 airfoils shows that the airfoils are rather similar, although there are some differences. The lift curve of the S809 seems to have a less abrupt stall compared to the S834. It is not surprising that the low drag region of the S809 is shifted down compared to the S83X data presented considering the difference in Reynolds numbers. The Reynolds number discrepancy makes comparison of drag more difficult, but the S809 does seem to have a wider low drag range compared to the S833 and S835. Thus there are some uncertainties to

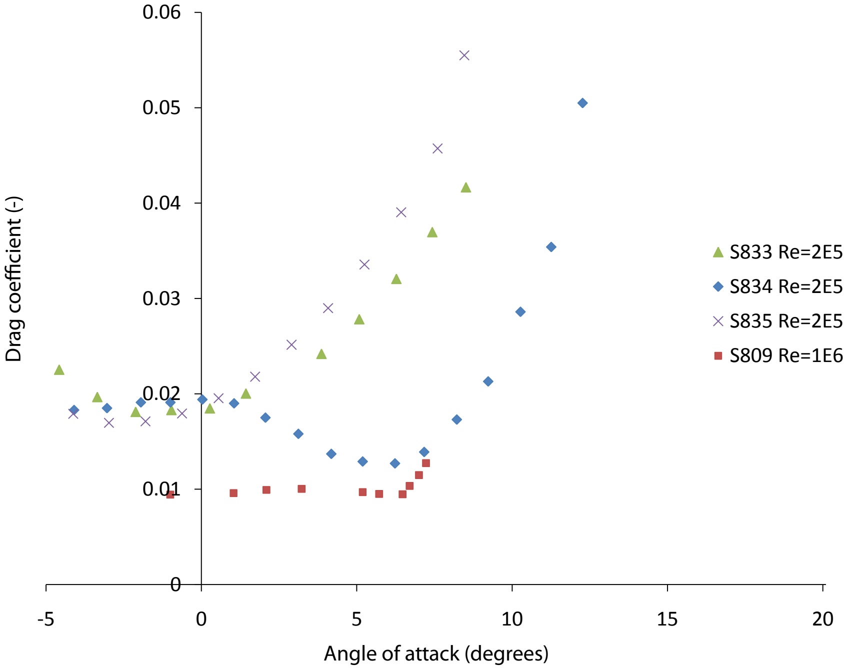

Figure 3.3: 2D drag data for S83X and S809 airfoils. Adapted from Somers [51] and Selig [9].

scaling the UAE airfoil data to that of the research blade. However with limited other options, this method was pursued. The method used to extrapolate the post-2D-stall airfoil data for the S83X airfoils is outlined next.

It was first of all assumed that for this set of airfoils the stall delay peak occurs at 15° and the blade begins to behave as a flat plate at 20° as was the case for the UAE Phase VI blade [21]. Secondly, scaling factors were used to estimate the values of $C_{L_{15^\circ}}$, the lift coefficient at the stall delay peak of 15°, and $C_{L_{20^\circ}}$, the lift coefficient at 20°. Beyond 20° the Viterna model was applied using an AR of 10.9. The drag coefficient at 20°, $C_{D_{20^\circ}}$, was determined using $C_{L_{20^\circ}}$ and assuming the L/D value of 2.75 for a flat plate at 20° [21]. Two-dimensional wind tunnel data for the S83X series airfoils was available up to the onset of stall at 7° [9]. The C_L data in between 7° and 15°, and 15° and 20° was interpolated linearly. The C_D data from 7° to 20° was interpolated using a shape function to replicate the shape of this region in figure 2.13. The relations used to determine $C_{L_{15^\circ}}$, $C_{L_{20^\circ}}$, and $C_{D_{20^\circ}}$ are outlined in equation 3.1, equation 3.2 and equation 3.3:

$$(C_{L_{15^\circ}})_{S83X} = \left(\frac{C_{L_{15^\circ}}}{C_{L_{7^\circ}}}\right)_{S809} (C_{L_{7^\circ}})_{S83X} \tag{3.1}$$

$$(C_{L_{20^\circ}})_{S83X} = \left(\frac{C_{L_{20^\circ}}}{C_{L_{7^\circ}}}\right)_{S809} (C_{L_{7^\circ}})_{S83X} \tag{3.2}$$

$$C_{D_{20^\circ}} = \left(\frac{C_L}{C_D}\right)^{-1}_{flatplate_{20^\circ}} C_{L_{20^\circ}} \tag{3.3}$$

With these data points established it was possible to generate airfoil data files that compensated for stall delay and extended as required into the post-stall regime. These files were compiled using 2D airfoil data up to 7°, scaled data points from 7° to 20°, and the Viterna model beyond 20°. One final task was to extend the data into the negative angle of attack regime, beyond -4° where the 2D airfoil data ended. To accomplish this, the AirfoilPrep spreadsheet [55] was used. This spreadsheet provides several tools for preparing airfoil data for entry into BEM wind turbine simulations. In this case the "TableExtrap" sheet was used to extend the data into the negative α regime. To extend the data the TableExtrap sheet simply reflects the existing data from the matching point (in this case 20°) to 90° and applies a scaling factor of 0.7 to C_L to account for airfoil asymmetry [56]. With this the complete airfoil data tables were ready. An example of the final airfoil data is shown in the next section.

Using Aerodas model As mentioned in section 2.3.3.3, the Aerodas model requires airfoil data that includes the 2D stall peak. Unfortunately, data spanning this range was only available for the S834. However, a set of airfoil data was produced with this method to provide a comparison to the method used above. To do this the blade had to be modeled as having the S834 airfoil along the entire span. This is clearly not the case as the S834 is only present over the outer 5% of the blade. To check the validity of this assumption, the data sets of the three S83X airfoils were compared. The lift and drag curves were presented previously in figure 3.2 and figure 3.3, respectively.

Note firstly that, unlike the data available for the S833 and S835, the S834 set provided enough information for the Aerodas model to be applied. From a lift point of view, it appears that the S833 performs very similarly to the S834. The S835, however, has consistently higher lift coefficients. The drag comparison shows the S833 to have slightly greater drag at higher angles of attack, with the S835 having even greater C_d values over this range. At lower angles of attack, this trend is reversed with the S835 displaying the lowest drag. Thus there are clearly differences between

Parameter	Value
A0	-1.11
t/c	0.15, 0.18, 0.21
ACL1'	14.27
CL1max'	1.073
S1'	0.1253
CD0	0.0191
ACD1'	14.27
CD1max'	0.0656

Table 3.1: Inputs to Aerodas model for S834 airfoil.

the airfoils but, despite the discrepancies, this method was pursued as it was desired to generate another set of airfoil data to predict the performance of the blade. The input parameters to the Aerodas model were therefore extracted from the S834 data set and are presented in table 3.1.

Note that there are three t/c values presented in table 3.1. This is because the t/c values of the S833, S834, and S835 are 0.18, 0.15, and 0.21, respectively. Thus despite the lack of airfoil data for the S833 and S835, tables were produced accounting for the changing airfoil thickness along the span of the blade. Using the Aerodas equations outlined in section 2.3.3.3, airfoil data spanning the operating range was produced. A sample is presented in figure 3.4 with the VTK data provided for comparison.

When compared to the data produced using the VTK method there are noticeable differences. The maximum lift coefficient in the VTK method is 1.27 at 15.2°, whereas with the Aerodas model it is 1.06 at 16°. It is rather encouraging, however, that the Aerodas model predicted the stall-delay peak to occur very close to that of the VTK method. The maximum drag coefficient in the VTK method is 1.32 at 85°, and 1.78 at 90° in the Aerodas case. The lift coefficient in the Aerodas model also has a valley at 27.5°, whereas in the VTK method there is no valley present after the peak at 15.2°. The drag coefficient in the VTK model is less than that of the Aerodas model up to 20°, after which point it rises much more steeply. It reaches 0.43 at 20°, as compared to the Aerodas value which is only 0.24 at 20°. Airfoil data files such those presented in figure 3.4 were provided for use in the rotor performance analysis stage. Their differences will become relevant in the performance predictions, which are presented later in section 3.1.5.

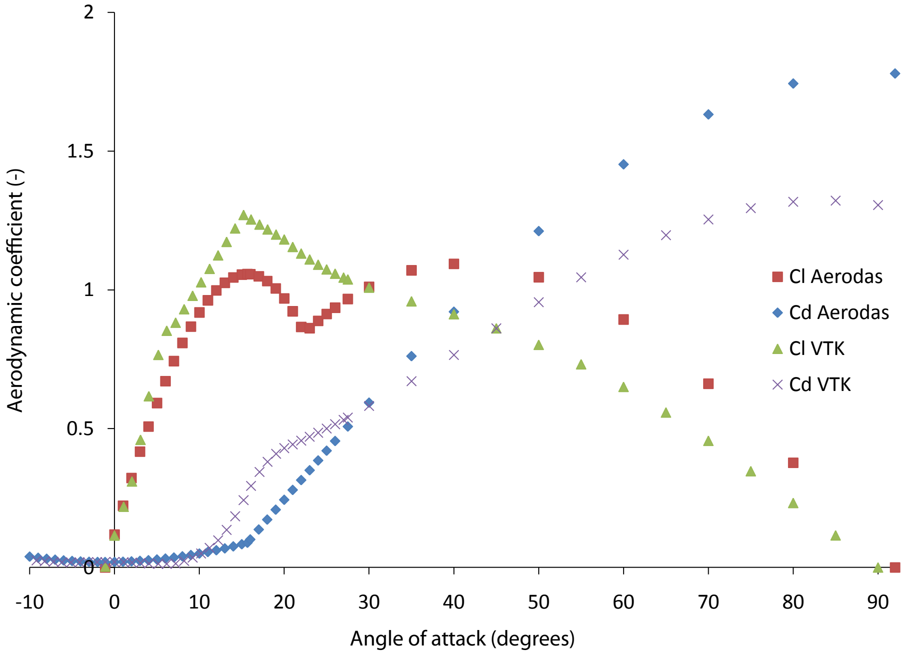

Figure 3.4: S834 data produced using Aerodas model with comparison to VTK data. $Re = 2 \times 10^5$.

3.1.4 Determination of geometry

The blade geometry is set by determining the aerodynamically optimal chord and twist distributions. This was accomplished using the PROPID design code [13] that was outlined in section 2.3.2.4. The airfoil data used to optimize the geometry was the unmodified 2D wind tunnel data available for all three airfoils. This data was selected based on the assumption that such data is valid prior to the 2D stall angle [21] and hence at the design point. Upon generation of an optimal design, the geometry is typically modified to account for structural and other considerations after which performance is re-evaluated.

3.1.4.1 Model parameters

In order to complete the design certain assumptions and specifications regarding the model must be made. These are shown in table 3.2 with brief notes regarding them. Initial chord and twist distributions are also specified, both of which are used as starting points for the iteration. The design point must also be specified in the model. The design point specifies the operational conditions at which to optimize the design and is defined by the rotor frequency and wind speed. As mentioned in section 3.1.1, constraints required that the rotational speed be 200 rpm and the wind speed be 6.5 m/s which correspond to a tip speed ratio of 5. These parameters define the design point.

Table 3.2: PROPID parameters

Parameter	Value Specified	Notes
Tip loss model	On	Prandtl's Method
Hub loss model	On	Prandtl's Method
Brake state model	On	Spera correction for high induction factors
Post-stall model	Off	Corrected 2D data used
Wake Swirl	On	Account for angular momentum
Number of blade elements	10	10 spanwise elements
Hub cutout	0.09R	Hub occupies inner 9% of radius, thus no power is produced there
Hub height	3 m	from rig geometry
Number of blades	3	standard for HAWTs
Blade length	1.6 m	from blockage ratio analysis

3.1.4.2 Design procedure

With all the aforementioned details provided, the iterative design was performed. PROPID allows the user to "specify desired aerodynamic characteristics from which the corresponding blade geometry is determined. More generally, any number of desired physically realizable characteristics can be achieved as long as some other variables are left to be determined" [14]. The aerodynamic characteristics can be single values or distributions along the blade. In this case, the angle of attack and axial induction factor distributions were specified and the twist and chord were determined by the process. See appendix C for the PROPID input file used for the design.

The α distribution was established by determining the α at which the maximum L/D occurs at each blade station. This angle changes along the blade due to the variation of local chord and flow velocity which affects local Reynolds number. Airfoil characteristics vary with Reynolds number thus at each blade station the maximum L/D occurred at a slightly different α. With the α distribution prescribed, PROPID iterates on blade twist at each station and determines the required distribution. The chord distribution was also optimized by setting the axial induction factor distribution to a constant optimal value across the blade. This optimal value is 1/3 as was derived by Glauert [2]. The chord distribution was determined iteratively based on the prescribed axial induction factor distribution which completes the blade design. The result is an aerodynamically optimal blade. Structural and manufacturing considerations can, however, end up altering the final chord and twist distributions which result in slight performance penalties.

With an optimal design established, the geometry was evaluated. Often the chord and/or twist distributions are linearized to produce a simpler blade that is easier to manufacture. For this reason, several linearizations on the chord were performed. The goal of the linearization was to maintain similar dimensions along the middle part of the blade while maintaining manageable chord lengths at the root and tip. It was also desired to keep the Reynolds number at the tip (Re_{tip}) close to 2.0×10^5 for winglet design consideration. As mentioned in section 2.5, Shimizu et al. [6] found that power augmentation due to endplates on a wind turbine of this size decreases from 9 % to 4% when Re_{tip} is increased from 1.0×10^5 to 1.5×10^5. Maughmer [36], meanwhile, designed an applicable winglet airfoil for sailplanes with a recommended Re operating range of 1.7×10^5 to 1.0×10^6. The tip chord was thus sized such that Re_{tip} is roughly 2.0×10^5 knowing that lower Re_{tip} values can be analyzed using the variable speed turbine by reducing the rotor speed.

Changing the chord distributions inherently changes the Reynolds number distribution and hence α of maximum L/D. Thus, a new optimal twist distribution was determined using PROPID's iterative approach, as before. The rotor efficiency is more sensitive to changes in twist therefore this optimal distribution was not linearized.

3.1.5 Final blade specifications

The final chord and twist design details can be found in figure 3.5 and figure 3.6, respectively. These details along with the airfoil distribution define the blade completely. The three-bladed rotor's performance was also predicted with WT_Perf using the two different sets of airfoil data outlined above. A plot of the predicted C_P vs. λ is shown in figure 3.7, while figure 3.8 displays the power curve. See appendix D for one of the WT_Perf input files used to analyze the rotor's performance.

The curves display the expected shapes for a stall-regulated three-bladed HAWT that were presented in section 2.4.1. The predictions by the two models have certain noticeable discrepancies. Firstly, both predict a maximum power coefficient ($C_{P_{max}}$) at $\lambda = 5.3$, but the VTK method's estimate is 0.46 whereas that of the Aerodas method is 0.36. The VTK method's $C_{P_{max}}$ estimate should be more reliable since data for the actual airfoils was used in this method and, as mentioned before, the performance at the design point should be relatively immune to rotational effects and hence 2D airfoil data is valid. Additionally, the Aerodas model modified the aerodynamic coefficients in the pre-2D stall regime, reducing lift and increasing drag. Thus it is no surprise that Aerodas predicted a reduced $C_{P_{max}}$ compared to the VTK data. The VTK method predicted a maximum power of 1440 W at 10 m/s while the Aerodas predicted 1600 W at 11.5 m/s. The predicted values for power at the cut-out speed are very close. The VTK method predicts the power to rise back to 1440 W at the cut-out speed of 22.5 m/s, while the Aerodas model predicts 1480 W. Had more complete airfoil data been available for the S833 and S835 it is possible that the Aerodas prediction would lie closer to that of the VTK method, which used the available data for those airfoils. These predictions will be compared to experimental data later.

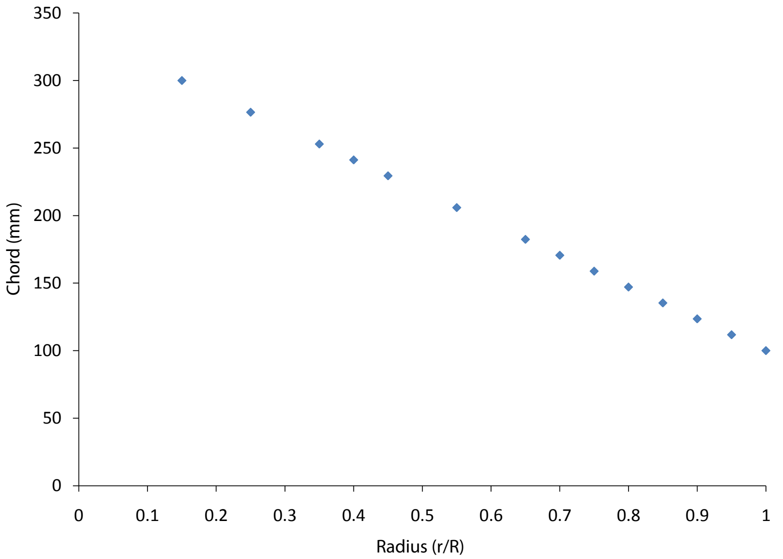

Figure 3.5: Final chord distribution of blade.

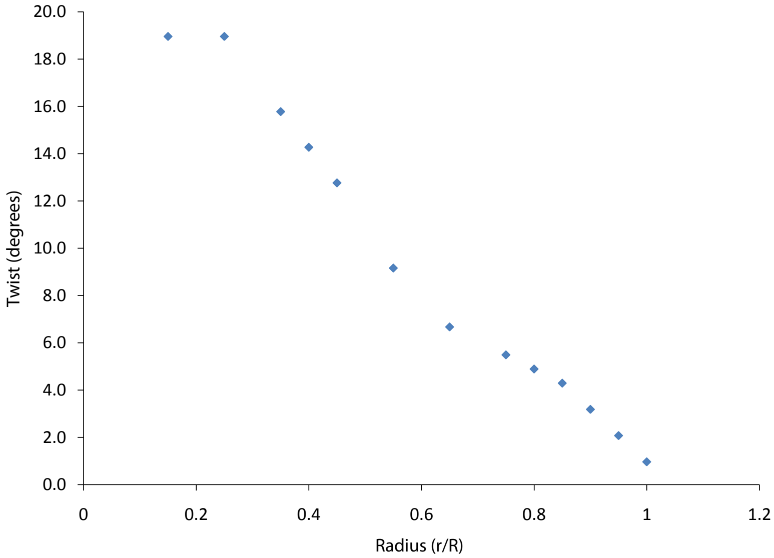

Figure 3.6: Final twist distribution of blade.

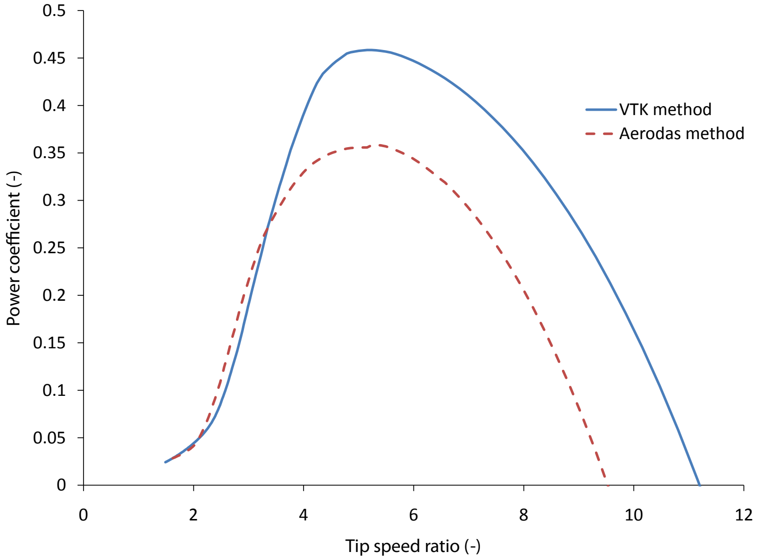

Figure 3.7: Predicted power coefficient vs. tip speed ratio of rotor.

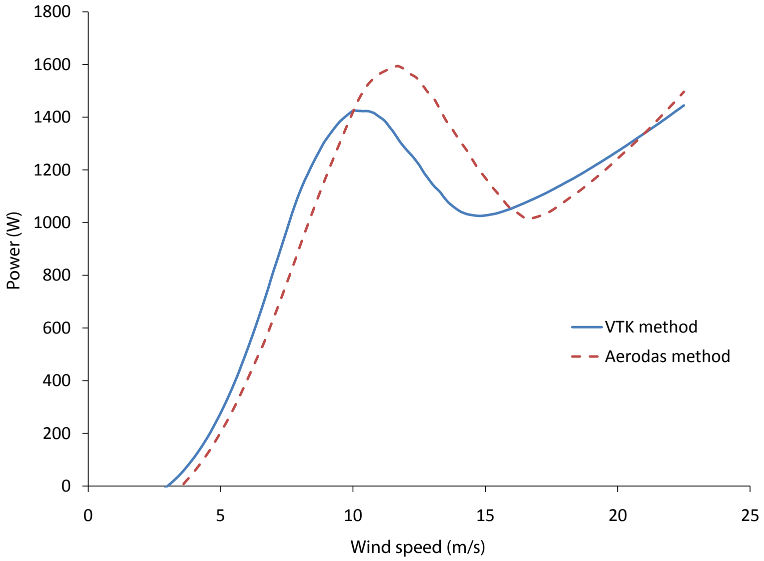

Figure 3.8: Predicted power curve of rotor.

3.2 Winglet designs

As discussed in section 2.5.1, a winglet is defined by the cant angle, height, twist, sweep, toe, and also the chord distribution or planform (rectangular, tapered, elliptical, etc.), airfoil, and location (pressure or suction side of wing). Ideally an aerodynamic analysis code, similar to those presented in other works on wind turbine winglets, would have been written to determine the parameters of an effective winglet for this particular wind turbine blade. To complete such a code would require extensive effort, however, and considering the efforts required to complete the other phases of the project it was decided to design the winglets based on the trends observed in the literature and the recommendations of Maughmer, both discussed in section 2.5. Personal correspondence with Maughmer also led to the discovery that David Maniaci, a Ph.D. candidate in his research group, had been authoring a winglet design code called WindDVE. Upon contacting Maniaci, a collaboration was agreed to which would have Maniaci design a winglet specialized for the research blade in exchange for the author to test the winglet and provide the results. Another winglet design was also completed as was originally planned.

3.2.1 Maniaci winglet

Maniaci's winglet design code, WindDVE, uses a vortex analysis method to determine the flow conditions at the blade tip. Using this code, Maniaci produced a winglet design that was optimized for a wind speed of 6.3 m/s ($\lambda = 5.3$) which corresponds to the maximum C_p of the blade. According to his analysis the winglet would increase C_p by about 10% at and above the design wind speed. This would result in a greater rated power, although Maniaci warned that the effect of stall on the winglet was not modeled which introduces some uncertainty. It was also predicted that the winglet would decrease rotor performance below 5 m/s [57]. See figure 3.9 for the predicted power curve with and without the Maniaci winglet. Note that Maniaci's code predicted a lower maximum power than the BEM prediction provided in section 3.1.5.

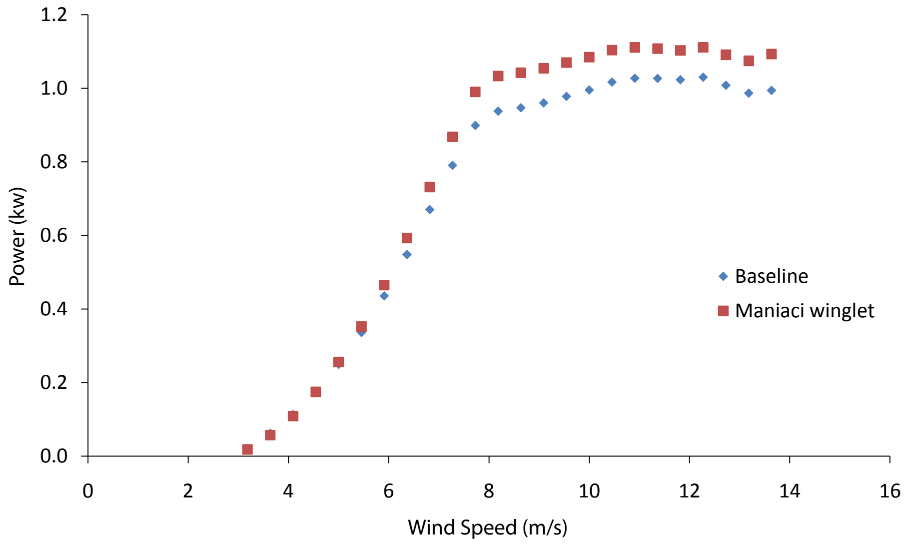

Figure 3.9: Predicted power curve with and without Maniaci winglet. From Maniaci [57].

The airfoil used was the PSU-097 [37], the drag polar of which is presented in figure 2.25. The Reynolds number ranged from 1.8×10^5 to 2.3×10^5, which is at the lower end of the design of this airfoil. The design parameters are outlined in table 3.3, and a solid model of the winglet can be found in figure 3.10.

3.2.2 Gertz winglet

As mentioned above, the method chosen to perform the winglet design was to review the literature and consider the work of Maughmer to establish a suitable design. Table 2.5 in section 2.5.1.2 summarized the literature relating to wind turbine winglet design and analysis. Upon review of this summary, some agreement was found for certain design parameters. The winglet location is always on the suction side, while the cant angle is fairly constant at 80° to 90°. Both of these trends agree with Maughmer's logic and designs [36]. The heights vary from 1% to 10% of radius, however both studies at lower Reynolds numbers (2.4×10^5 and 8×10^5) used a height of 10%. In addition, the positive experimental findings on Mie vanes discussed in section 2.5.1.3 were obtained using tip vanes with a height of 9% of radius. As well, discussions with Maughmer found that while sailplane winglet heights varied from 6% to 8% of semi-span, the best results occurred at 8% [58]. It was thus decided to use a height of 8%. An elliptical planform was chosen to produce the most efficient lift profile possible. The root chord ratio, which is the ratio of the winglet root chord to blade tip chord, was set to 1 to maximize the Reynolds numbers along the winglet span. Maughmer also mentioned that the PSU 94-097 operated sufficiently down to Reynolds numbers of 6×10^4 [58]. This set the tip chord length to 34 mm and thus the taper ratio to 0.34.

The twist, sweep, and toe angles, meanwhile, vary in the literature from $-2°$ to 13°, 0° to 30°, and 0° to 5°, respectively. Considering the lack of consensus on these parameters, Maughmer and Maniaci were consulted. Sweep is used to achieve a uniform stall pattern, however without any experimental data to refer to it was set to zero. As for toe and twist, after correspondence with Maniaci it was decided to explore the opposite extremes of his design to quantify the effect of such a configuration. Maniaci said that having a toe of roughly zero and a twist of $-0.5°$ could help more at wind speeds below the design speed while perhaps hindering performance above [59]. This would actually be more desirable from an annual energy capture point of view since lower wind speeds are more probable. For this reason a toe of $-0.5°$ and twist of $-0.5°$ were chosen for this design. See table 3.3 for the parameters defining the Gertz winglet and figure 3.11 for the solid model.

While no prediction was made for the effect of this particular winglet, it was hoped that having made educated decisions on the parameters would result in a useful winglet. Either way the experimental results would help Maniaci refine his code.

Design	Side	Planform	Root chord ratio $\left(\frac{c_{blade_{tip}}}{c_{winglet_{root}}}\right)$	Tip chord	Cant (°)	Height (%R)	Twist (°)	Sweep (°)	Toe (°)	Airfoil
Maniaci	suction	rectangular with taper	0.95	0.79	90	8	3.5	0	-3	PSU 94-097
Gertz	suction	elliptical	1	0.34	90	8	-0.5	0	-0.5	PSU 97-097

Table 3.3: Design parameters of Maniaci and Gertz winglet.

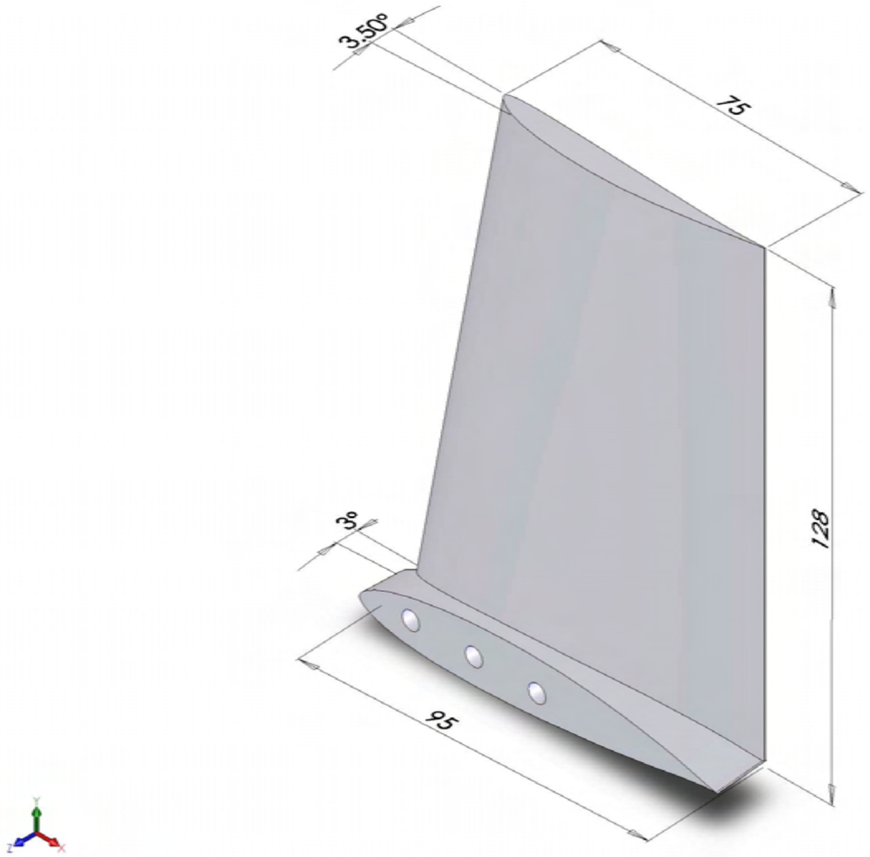

Figure 3.10: Solid model of Maniaci winglet. Dimensions in mm and degrees.

3.2.3 Comparison of winglet designs

Although the Gertz and Maniaci winglets shared some design elements, there are certain important differences. The most notable difference between the two winglets is the setting angle distribution. The setting distributions are plotted in figure 3.12 to demonstrate more readily the effect of the toe and twist angles.

Maniaci's design uses a positive twist angle which establishes wash-out. To wash-out a blade or wing is to set the twist such that the angle of attack decreases towards the tip. The Gertz winglet, meanwhile, applies a negative twist angle to establish wash-in, which uses twist to increase the angle of attack towards the tip. Such a contrast in twist strategies should allow for valuable insight into how this parameter is best suited. The planform shape and winglet root chord ratio are also different.

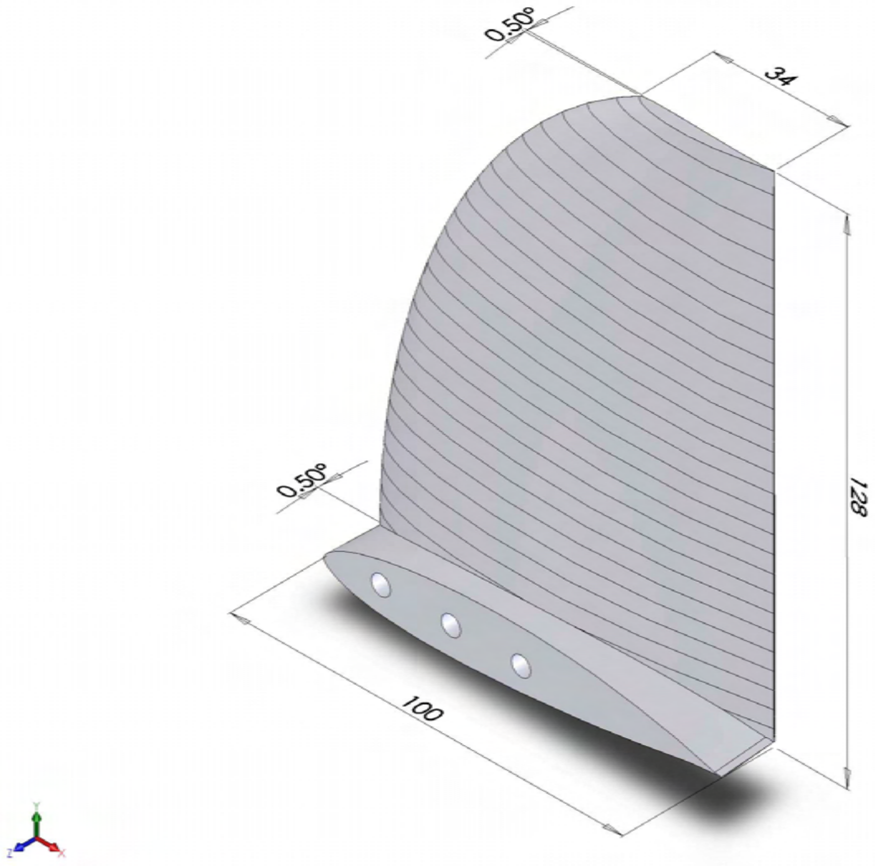

Figure 3.11: Solid model of Gertz winglet. Dimensions in mm and degrees.

The Gertz winglet uses an elliptical planform which in theory provides a more efficient lifting surface as compared a linear taper such as that used on the Maniaci design. In addition, the Gertz winglet root chord is equal to the blade tip chord whereas Maniaci's has a reduced root chord. The combination of these two features maintains greater chord lengths over the region near the root for the Gertz design. Conversely, the tip chord of the Gertz winglet is less than half that of the Maniaci design. Thus the tip region of the Gertz winglet has reduced chord lengths compared to Maniaci's. As was discussed in section 2.5.1, Reynolds number concerns lead to the desire to maintain greater chord lengths whereas wetted area concerns call for reduced chords. Clearly the Gertz and Maniaci designs take different approaches to addressing these issues, however the resulting chord distributions are still rather similar. Thus

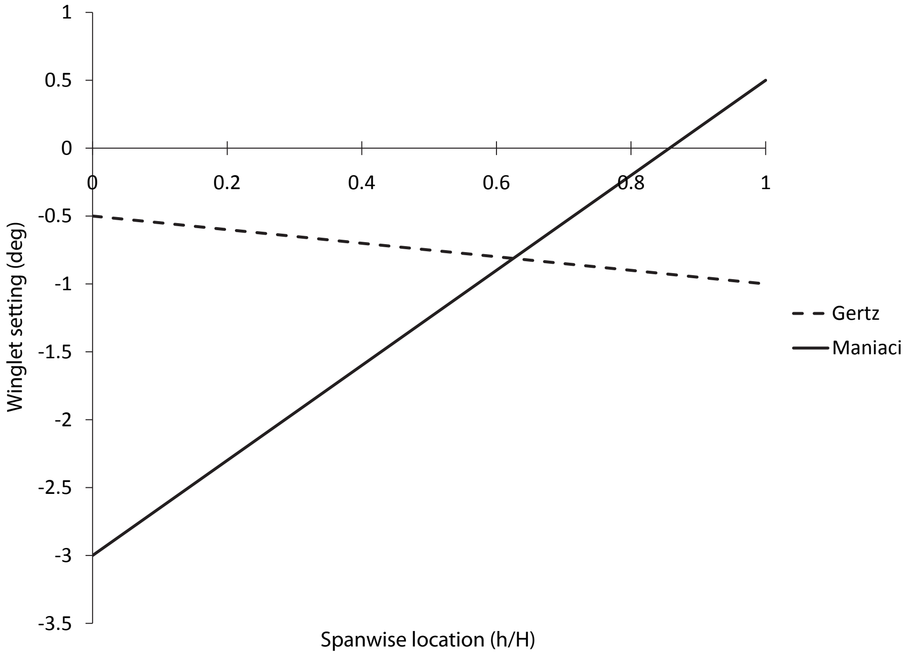

Figure 3.12: Comparison of setting distributions of Maniaci and Gertz winglets.

the main difference between the two designs is the setting angle distribution and the experimental data should provide a useful comparison.

Chapter 4

Blade structure and fabrication

With the dimensions and shape of the blade established, the next step was the structural design and fabrication. A connection with a composites manufacturing plant was already established making it possible for the blades to be built out of fibre-reinforced plastic (FRP). Firstly, however, a method was designed to allow for interchangeable blade tips. After this the design of the composition of the blade structure was completed followed by the actual fabrication of the blades and winglets themselves.

4.1 Tip exchange mechanism

In order to test the effect of different blade tip shapes, provisions were made to allow for the physical exchange of the tip portion of the blade. The criteria and constraints layout of the coupler mechanism were the following:

- Provide exact alignment between mating sides
- Little to no disturbance to the aerodynamic surface
- Simple and secure locking
- Survive tension and bending loading in operation
- Small enough to fit near tip of blade

To satisfy the requirements a three-pin cam lock system was chosen with the pins protruding from the tip and into the main blade where the cams are located. Using three pins provides excellent alignment and cam locks were found to produce a tight, secure connection. See figure 4.1 for a diagram of the cam lock system.

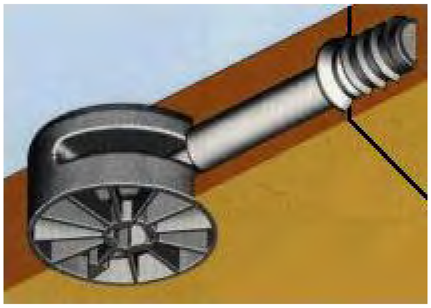

Figure 4.1: Cam lock mechanism. Adapted from das-holzportal [60].

Pins of 5 mm diameter and corresponding 12 mm diameter cams were selected, requiring the coupler to be located no further than the 90% radius location in order for the hardware to fit. This split the blade into a 1440 mm long main blade section and a 160 mm tip portion. The exchange mechanism is embedded into the cross-section with access holes to the cams in the main blade. This minimizes the hardware's disturbance to the aerodynamic surface. To locate the cam and pin holes precisely within the blade cross-section, blocks of maple wood were prepared in advance on a mill and placed within the blades during fabrication. These "coupler blocks" also contained a 100 mm x 40 mm x 10 mm volume of empty space which could be accessed after blade fabrication to dynamically balance the blades. See figure 4.2 for the solid model of the coupler block.

For installation, alignment provisions were designed into the molds which would allow the coupler blocks to be placed and located precisely during part fabrication. This ensured exact alignment of the coupler such that the mating surfaces would align perfectly when coupled together. A specialized tip was also prepared particularly for winglet testing. This tip connected to the blade at the 90% station using the aforementioned three pin cam lock system, and had itself a set of three cams such that the different winglets could be attached and detached from the end of that tip. A solid model portraying the connection of the tip to the blade and the winglet to the tip is shown in figure 4.3.

4.2 Blade structure and fabrication

The blades were fabricated out of FRP in-house after having been trained by wind turbine blade manufacturer Composotech Structures, Inc. [61] in Goderich, Ontario. The training consisted of building a set of three test blades in their shop, after which

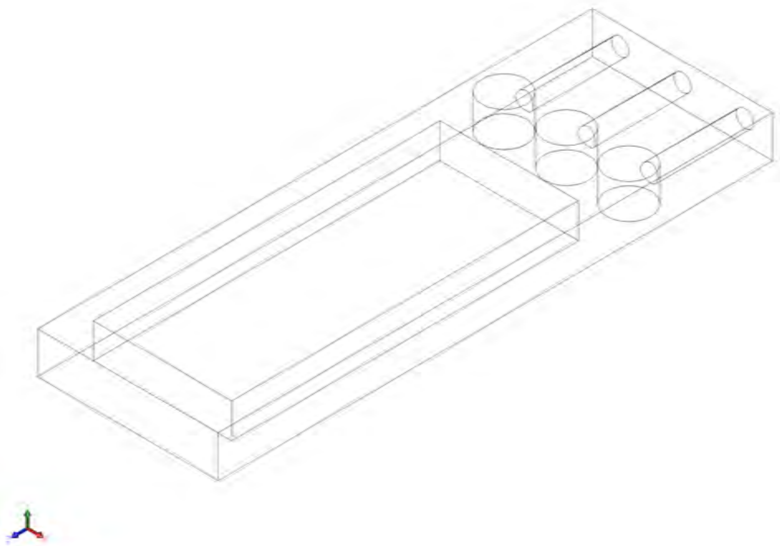

Figure 4.2: Solid model of coupler block.

the three final blades were produced in the laboratory. The blades are composed of FRP with iso-polyester resin and e-glass skin and structural layers. The outer surface of the blade is a polyester-based gel-coat compound. A fibre-wrapped foam spar was used in the blade to strengthen against bending loading. The lay-up schedule was based on that designed by Composotech engineer Chris Wraith for the Wind Energy Group's other set of blades. Details of that blade can be found in Gaunt [62].

The tips were cut on a CNC mill out of maple wood and painted such that the surface finish matched that of the blades. A full account of the blade and tip production can be found in appendix B. Figure 4.4 shows a photo of one of the finished blades, while figure 4.5, figure 4.6, and figure 4.7 show pictures of the finished standard, Maniaci, and Gertz tips, respectively.

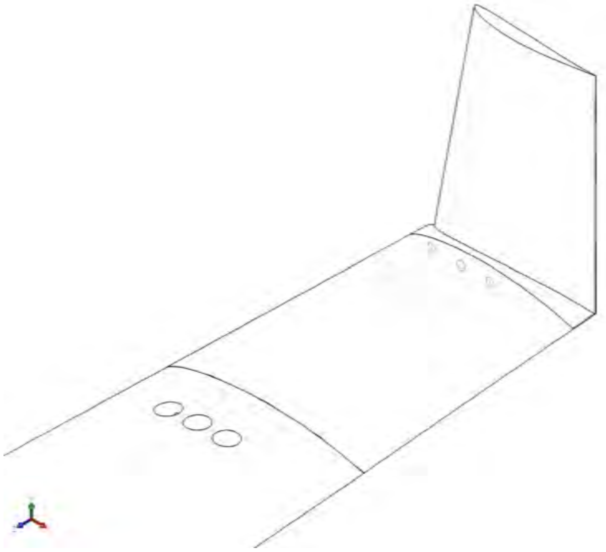

Figure 4.3: Tip connection assembly with specialized winglet tip.

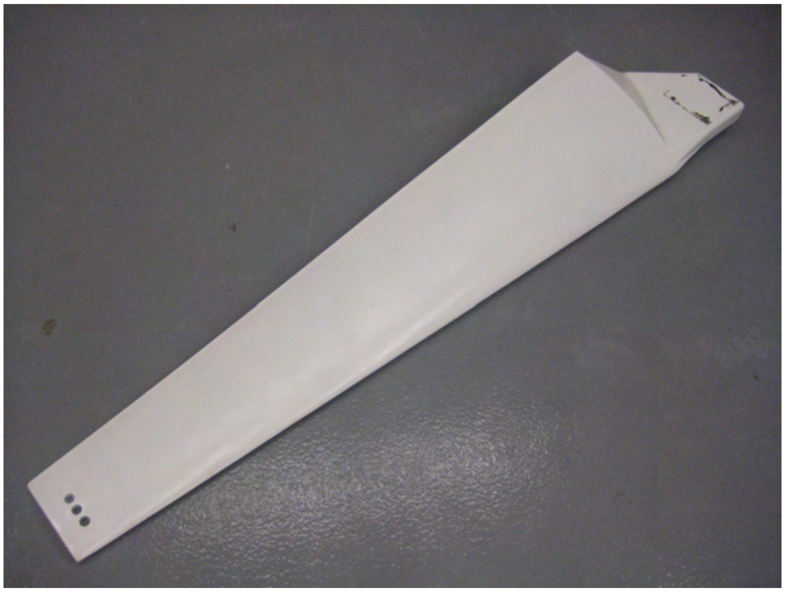

Figure 4.4: Completed blade.

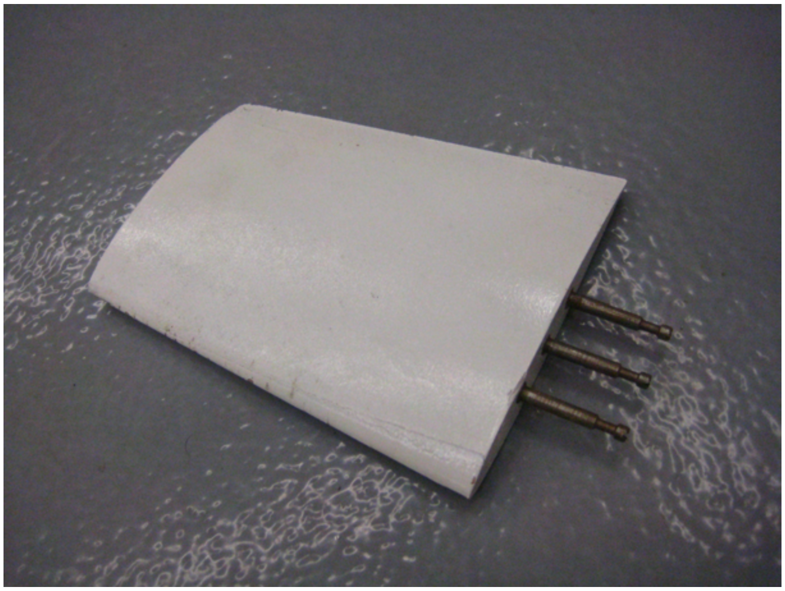

Figure 4.5: Standard tip.

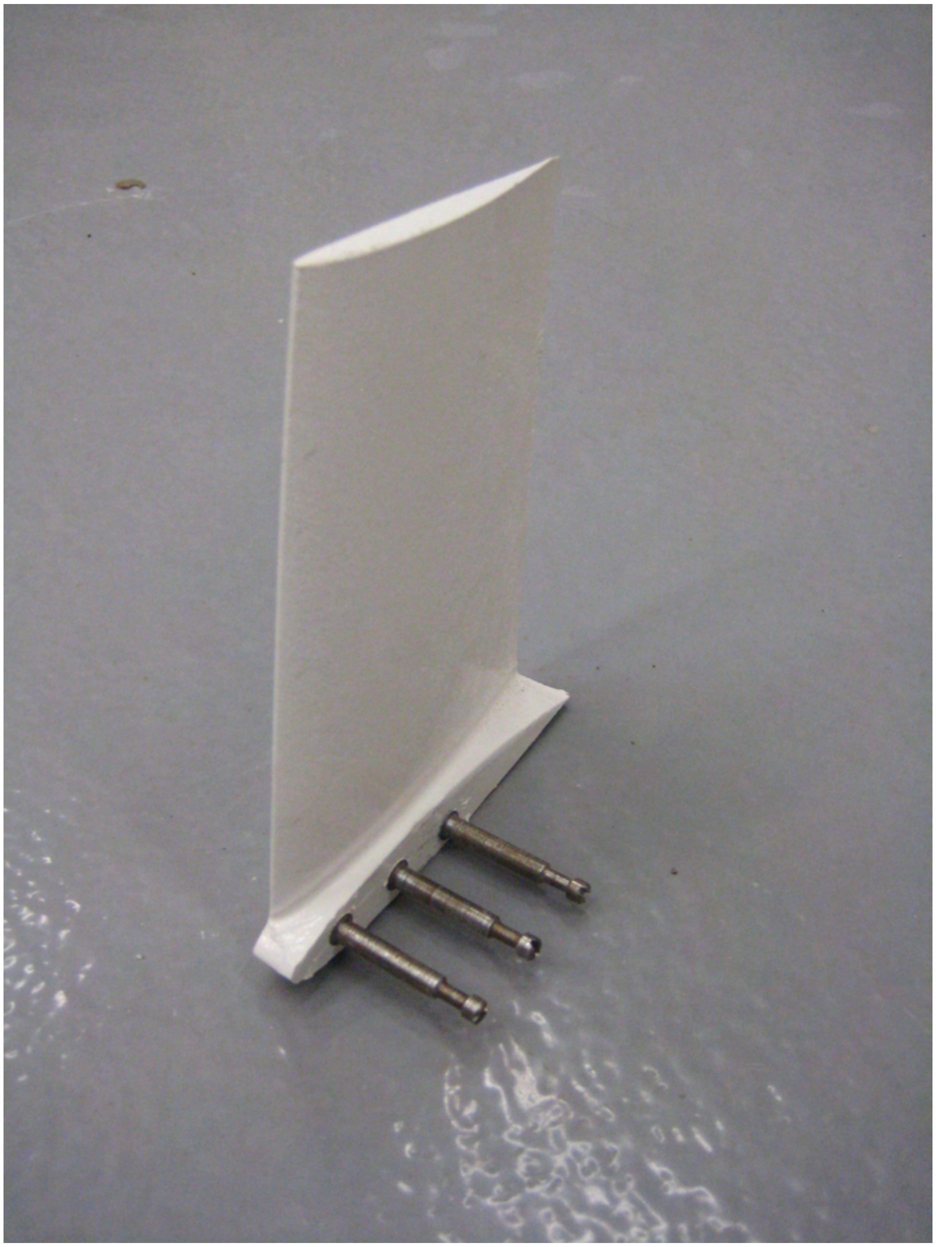

Figure 4.6: Maniaci tip.

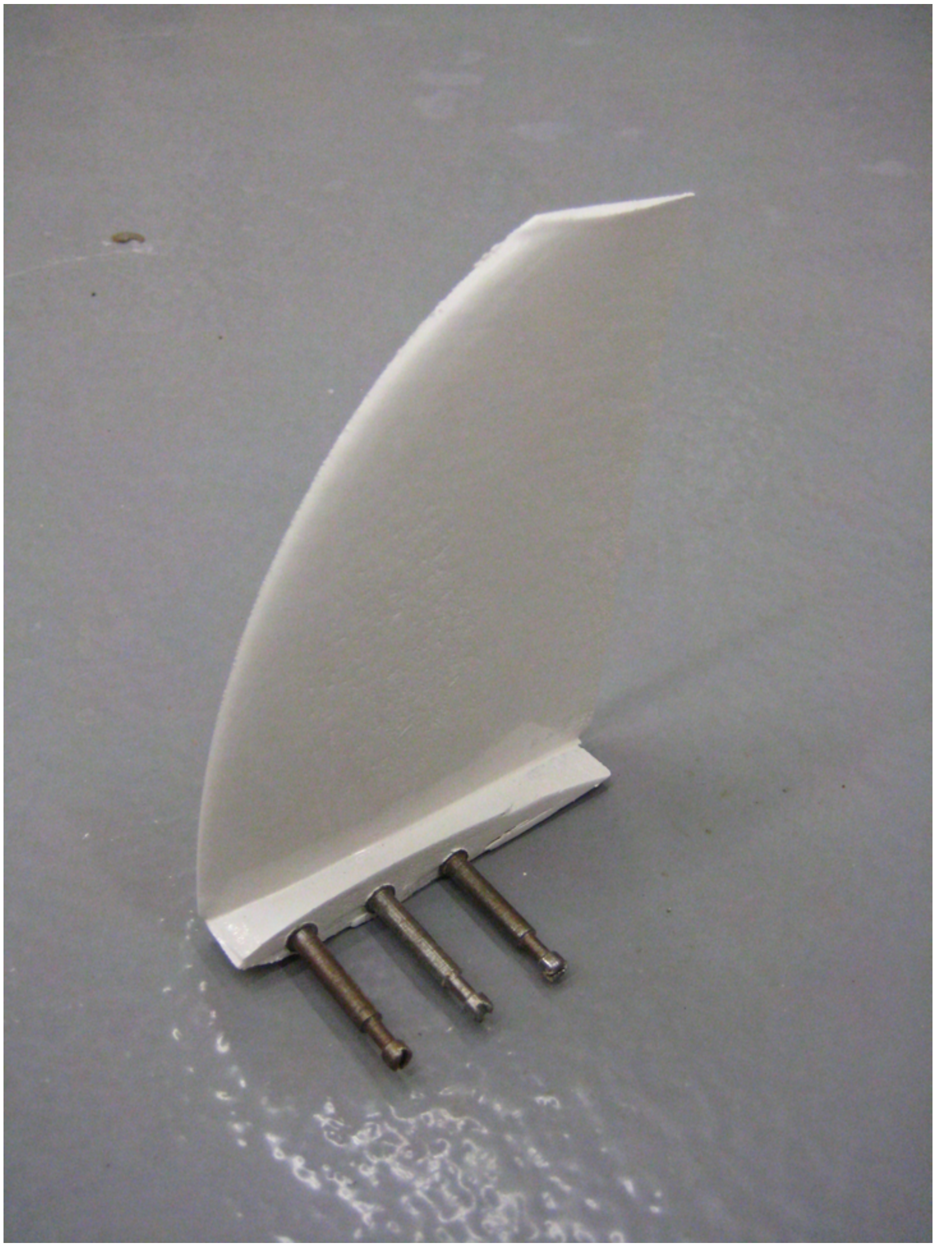

Figure 4.7: Gertz tip.

Chapter 5

Experimental procedure and apparatus

The wind facility and turbine rig used for this experiment are outlined in the sections below as well as the experimental procedure and instrumentation arrangement.

5.1 Facility

The experiment was performed at the University of Waterloo Wind Energy Research Facility shown in figure 5.1. This facility has a semi-open jet wind tunnel with a 8.23 m wide by 5.9 m high velocity field that exhausts into an open-ended test section. The test area is 15.4 m wide, 19.5 m long, and 7.8 m high at the sides and 13 m high at the peak. The wind exits the large-scale test area through a 7.93 m × 7.93 m sectional door which is open to atmospheric air at all times. Flow conditioning in the plenum is provided by two settling screens and a seven across by five high array of steel flow-straightening ducts. The fan exit plane at the ducts is rectangular with a 8.23 m width and 5.9 m height as shown in figure 5.2 [62].

The facility has six identical 2.64 m diameter fans driving the flow [63]. The fans are arranged in a 3 across by 2 high grid and are capable of being operated independently with variable frequency drives. Within the control room, adjacent to the test area, a control panel allows for the precise control of the fan speeds through a variable frequency drive connected to each fan motor. This feature allows for the wind velocity to be varied as desired. Each fan generates an air flow of 78.7 m^3/s at 413.5 Pa and the test section velocity can be varied between 0 m/s and 11.1 m/s, with turbulence intensities ranging from 10% to 15%[62]. See figure 5.3 for the layout

Figure 5.1: UW Wind Energy Research Facility.

of the Wind Energy Research Facility.

Figure 5.4 shows a three-dimensional model of the test enclosure. Note the large burn house located just beyond the exit of the enclosure which presents significant blockage and heavily distorts the flow through the test section. Further details of the geometry and flow analysis of this facility may be found in Devaud et al. [64], Gaunt [62], and Best [63]. A variable speed 3.6 kW wind turbine rig was installed in the test section 8 m downstream of the exit of the flow-straightening ducts. Details of the rig and the associated instrumentation are given next.

5.2 UW Wind Energy Group turbine rig

The UW Wind Energy Group turbine rig, pictured in figure 5.5, was designed and assembled by previous students in the research group. Details of the design can be found in McWilliam [45], while the assembly and commissioning is outlined in Gaunt [62]. The rig consists of a nacelle which is mounted on a dual-pole tower such that the rotor hub height is 3.1 m above the test section floor. The three-bladed rotor is mounted to the low-speed shaft at the front of the nacelle. There is also a pneumatic braking system with the brake disk on the low speed shaft. The brake is primarily

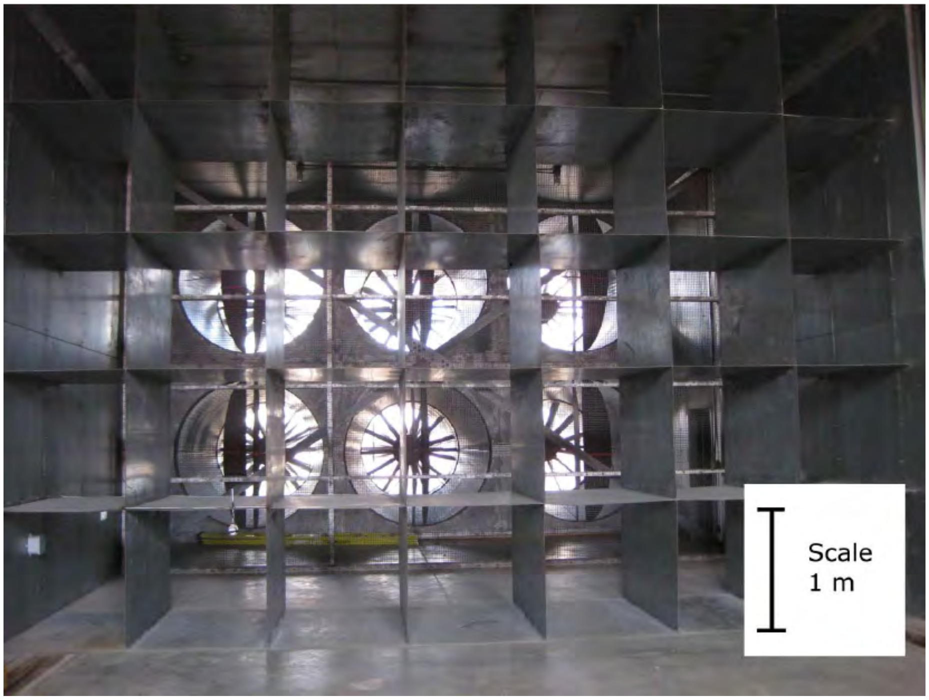

Figure 5.2: Fan exit looking upstream. From Gaunt [62].

used for parking the rotor but is also capable of serving as an emergency stop. Power is transmitted to the DC generator, located at the rear, through a three stage belt-and-pulley transmission. A diagram detailing the nacelle assembly can be seen in figure 5.6. The generator is connected to a load bank that absorbs the power produced by the rotor during testing. A sensor is also installed on the nacelle which measures the rotational speed of the low speed shaft. The speed of the rotor is controlled by varying the voltage across the generator using a manual knob in the control room. The maximum rotor speed is 240 rpm. Further details on the rig and electrical system can be found in Gaunt [62].

5.3 Measurements

5.3.1 Rotor power

Ideally the rotor power would be determined using a torque and speed sensor at the point the blades connect to the drivetrain but this method was not feasible with the

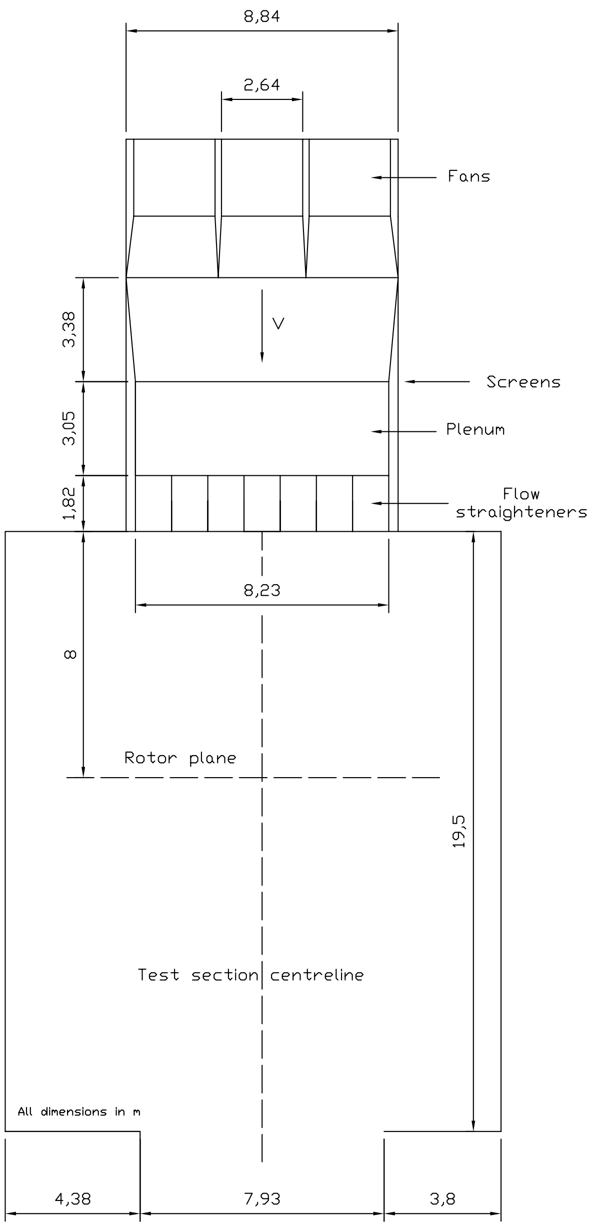

Figure 5.3: Wind Energy Research Facility floor plan. Adapted from Best [63].

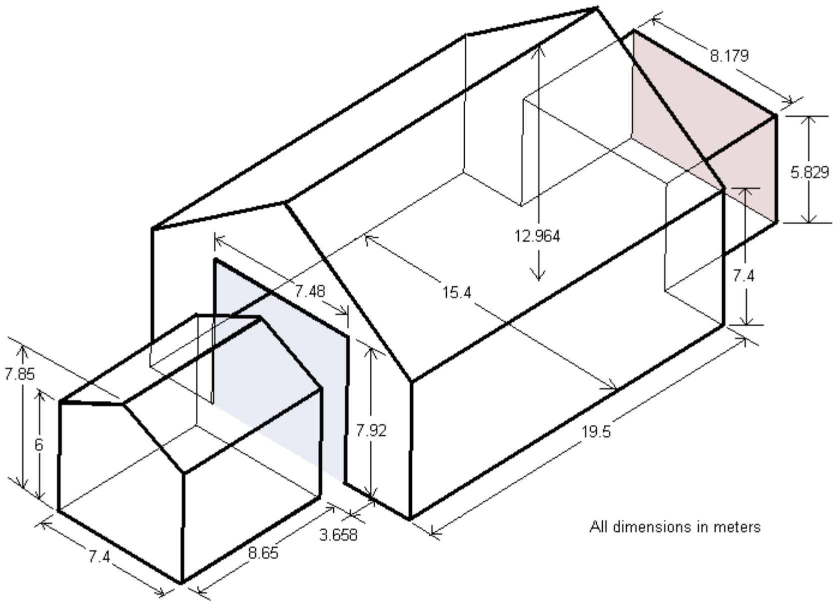

Figure 5.4: Three-dimensional view of test enclosure and burn house. From McWilliam [45].

available materials and a test rig that was designed to accommodate other instrumentation. For this reason it was required to take electrical measurements at the load. Such a measurement, however, does not account for the power losses through the drivetrain. As can be seen in figure 5.6 the drivetrain is located between the rotor and generator and it is a source of power loss before the power is measured. The actual power generated by the rotor (P_{GEN}) is the sum of the drivetrain losses ($P_{drivetrain}$) and the load power (P_{load}), as shown in equation 5.1.

$$P_{GEN} = P_{drivetrain} + P_{load} \tag{5.1}$$

It is this total value that is of interest, since the results will be compared to an aerodynamic model which only predicts the power at the blades. It was therefore required to determine $P_{drivetrain}$ and add this value to P_{load} to determine the total power generated by the rotor, P_{GEN}. The procedure to estimate $P_{drivetrain}$ was to periodically measure the power required to spin the rotor and drivetrain ($P_{spinrotor}$)

Figure 5.5: Wind Energy Group turbine rig.

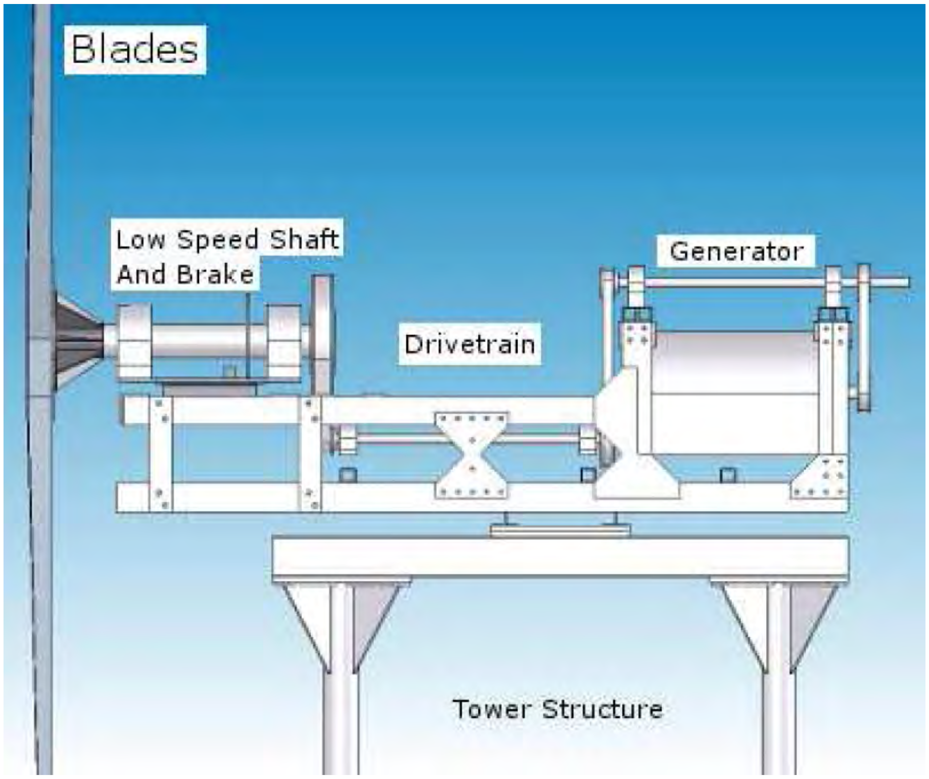

Figure 5.6: Nacelle assembly. From Gaunt [62].

without any flow through the tunnel and subtract the power required to spin the rotor ($P_{bladedrag}$), as shown in equation 5.2:

$$P_{drivetrain} = P_{spinrotor} - P_{bladedrag} \tag{5.2}$$

It was therefore required to estimate $P_{bladedrag}$. As is detailed later, the test plan called for operating the rotor over a range of shaft speeds. $P_{bladedrag}$ thus had to be measured at each operational shaft speed. To accomplish this, the shaft was motored at each operational speed without the blades mounted to the rig. This gave a measurement of $P_{drivetrain}$ at each of those shaft speeds. The blades were then attached and the same procedure was executed. Both of these steps were completed with the tunnel openings closed and the fans turned off such that the ambient wind was not a factor. $P_{bladedrag}$ was then determined by subtracting $P_{drivetrain}$ from $P_{spinrotor}$ as shown in equation 5.3:

$$P_{bladedrag} = P_{spinrotor} - P_{drivetrain} \tag{5.3}$$

This procedure resulted in an array of values corresponding to $P_{bladedrag}$ at different shaft speeds. Hence, a $P_{drivetrain}$ profile was generated on each day of testing.

To generate the $P_{drivetrain}$ profile on testing days, the following procedure was followed. Every five data points (a data point being a unique combination of wind and rotor speed), or roughly half an hour of testing, the fans were shut down and the tunnel openings were closed. Meanwhile, the rotor continued to spin at the speed at which testing was taking place. This measured the sum of $P_{bladedrag}$ and $P_{drivetrain}$, after which $P_{bladedrag}$, calculated previously, was subtracted. The $P_{drivetrain}$ profile was generated by linear interpolation of the $P_{drivetrain}$ calculations performed every five data points. This resulted in a unique value of $P_{drivetrain}$ for each data point generated.

5.3.2 Flow field

The rotor performance was predicted using a model that assumed an ideal environment; that is a turbulence intensity of 0%, no shear, fully developed flow, etc. It is thus important to establish the characteristics of the flow field in which the rotor was operating during experimental trials.

5.3.2.1 Wind speed

To complete the performance plots it is required to know the wind speed at the rotor plane. Past researchers have used a simple linear relation between fan frequency and test section wind speed such as equation 5.4 determined by Gaunt [62]:

$$V_\infty = 0.1844 \times f_{fan} \tag{5.4}$$

It has been found by Gaunt [62] and Best [63], however, that ambient conditions, specifically outdoor wind speed and direction in the vicinity of the facility, tend to affect the wind speed through the test section. For this reason it was desired to measure the wind speed at the rotor simultaneous to the other quantities, rather than rely on the linear relation between fan and wind speed. Ideally the anemometer would be placed at the plane of the rotor to measure the speed of the wind in which it is immersed. However, the presence of the spinning rotor was found to affect the flow such that there was no location in the plane of the rotor that a representative velocity could be measured. Another option would be to place the anemometer somewhere upstream where the rotor's influence is minimal. However, Best [63] found that in this particular facility, the average wind speed steadily decreases from the inlet to the outlet of the test section. This is a result of jet expansion due to the open jet nature of the facility. The only option, therefore, was to measure the wind speed far upstream where it is not affected by the presence of the rotor and use a correlation to determine the wind speed at the rotor plane. As a result, the anemometer was placed 6.5 m upstream of the rotor plane during performance testing. This position was found not to be affected by the presence of the spinning rotor.

A study was therefore required to determine the correlation coefficient between the rotor plane and the location 6.5 m upstream. Previous studies [65] had found that the velocity profile in the tunnel was not constant in the cross-stream direction. For this reason it was decided to take measurements at 2 locations in the rotor plane, one on either side of the centreline. These measurements would then be averaged to determine the average velocity at the rotor plane. Hence, there were 3 locations at which measurements were required in the test section to complete the correlation study. These locations (labeled 1, 2, and 3) are presented in figure 5.7. Note that all measurements were taken at 3.1 m above the test section floor which is the hub height of the rig.

Ideally, the correlation coefficient would be determined by taking simultaneous velocity measurements at all 3 locations. However, due to the equipment available this was not possible. It was therefore required to take wind speed measurements at one location and then move the anemometer to another location and repeat the test. This clearly introduces potential for error since the measurements are not simultaneous. Compounding this problem is of course the fact that outdoor ambient conditions are known to affect the flow through the tunnel, and hence for a given fan frequency the test section speed can vary. Nonetheless, this method was the best that could be devised, and to minimize error due to ambient conditions the correlation study was performed on a very calm day. The correlation plan is displayed in table 5.1 and shows the details of the tests performed in chronological order.

The results of the correlation study are presented in section 6.1.2. With this arrangement it would be possible to determine the actual wind speed at the rotor plane simultaneous to the other measurements of rotor shaft speed, rotor power, and air temperature.

5.3.2.2 Turbulence

The turbulence was determined using data gathered at location 2 (see figure 5.7) during the velocity correlation study. The data was collected at 9 fan frequencies

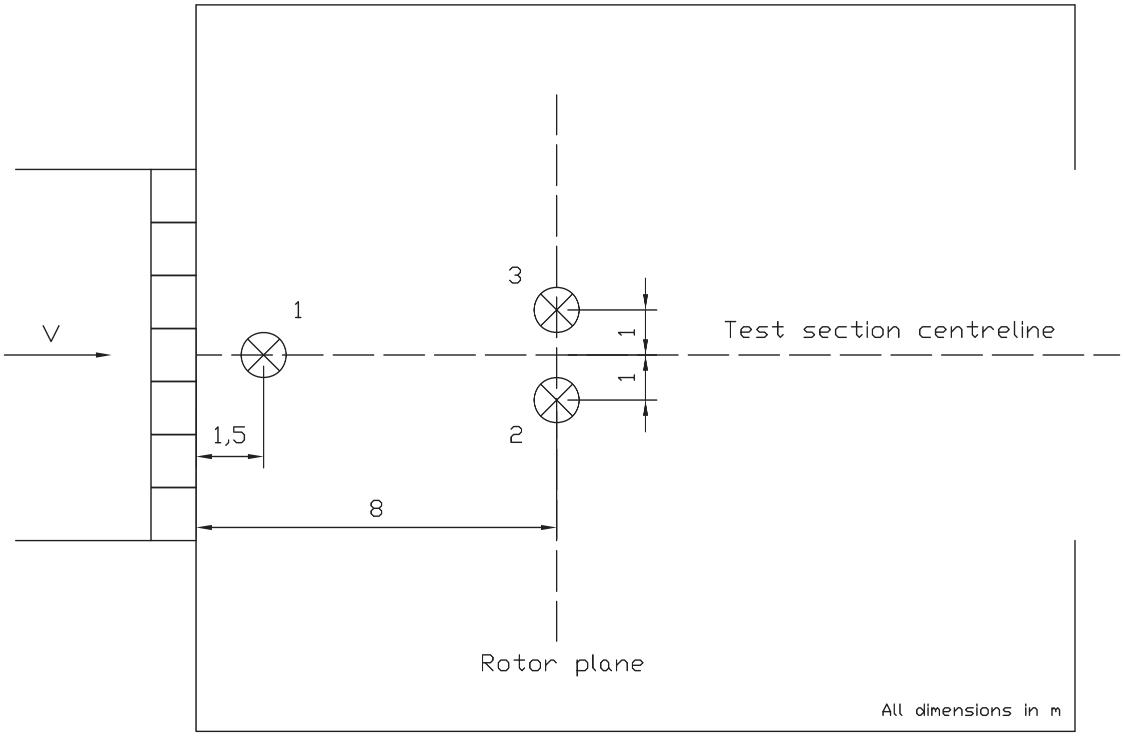

Figure 5.7: Measurement locations for correlation study.

from 20 Hz to 60 Hz in 5 Hz increments using the CSAT3 sonic anemometer at a sampling rate of 30Hz. The turbulence intensity, I, was calculated at each fan frequency using the relation in equation 5.5 [66]:

$$I = \frac{\sqrt{\frac{1}{3}\left(\overline{u'^2} + \overline{v'^2} + \overline{w'^2}\right)}}{\sqrt{\overline{u}^2 + \overline{v}^2 + \overline{w}^2}} \tag{5.5}$$

where u, v, and w are the components in the three orthogonal directions, $\overline{u}$ is the mean of the sample set and $u' = u - \overline{u}$.

Test label	Fan frequency (Hz)	Anemometer location
B	20, 30, 40, 50, 60	3
		1
		2
C	20, 30, 40, 50, 60	3
		1
		2
D	20, 30, 40, 50, 60	3
		1
		2

Table 5.1: Correlation study plan.

5.3.3 Data collection

The measurements gathered in the test section are gathered by a computer in the control room which displays and records the data. The data is managed by a custom designed Labview VI [67]. The VI records and provides a live display of the measurements and controls the data acquisition hardware. The power, wind speed, and air temperature measurements are captured using a Keithley 2700 [68]. The 2700 physically switches between channels which limits the sample rate to roughly one data point every three seconds (0.33 Hz). Power at the load is determined by independently measuring the voltage and current. The 2700 measures the voltage across the load directly and the current is determined using a shunt resistor. Power is determined by calculating the product of voltage and current. Wind speed and air temperature are measured using the Campbell Scientific CSAT 3 sonic anemometer. The rotor shaft speed is measured using an IR emitting diode which is fixed to the nacelle frame. A tab attached to the low speed shaft passes through the sensor once per revolution. The pulse from the rotor speed sensor is captured by the National Instruments NI 6251 data acquisition card and the signal is converted to the shaft rpm value by the card's digital counter feature. With this particular setup, it is possible to gather all of the measurements of interest (rotor speed, rotor power, wind speed, air temperature) simultaneously and record them to a text file to be analyzed later. The wind speed data is also collected simultaneously at 30 Hz using the CSAT3 data collection utility. This provides data at a far greater sampling rate if needed. For further details of the data acquisition system see Gaunt [62].

5.4 Experimental procedure

The experiment was designed to quantify the aerodynamic performance of the rotor. This was accomplished by generating the typical performance plots of C_P vs λ and power vs. wind speed. A typical wind turbine will operate in winds as low as 3 m/s and exceeding 20 m/s, while the facility can only generate steady wind at 3.7 m/s to 11 m/s. Therefore, in order to fully quantify the rotor's performance, it was proposed to operate not only at the design speed of 200 rpm, but as low as 100 rpm and as high as 240 rpm. Operating at these off-design speeds would generate C_p values at tip speed ratios that allow for the calculation of power output at wind speeds of 3.1 m/s to 22.1 m/s. The drawback to this method is that, at the off-design shaft speeds, C_p will be measured while the rotor is operating at Reynolds numbers above and below those at which it was designed to operate. Reducing the Reynolds number will increase the drag coefficient for a given angle of attack [46], and therefore the experimental data beyond 11 m/s will likely be a conservative estimate of the actual performance of the rotor at high wind speeds. To ensure that this practice would not introduce too much error the impact was quantified. To do so, the model used to predict the rotor power in section 3.1.5 was applied to generate a power curve at the variable speeds proposed for the experimental plan. See figure 5.8 for the resulting curve in comparison to the constant speed curve predicted earlier.

Recall that from 11 m/s to 22 m/s the rotor shaft speed decreases from 200 rpm to 100 rpm in the variable speed case. The impact is noticeable but certainly manageable. Not surprisingly, the variable speed curve is slightly below the design speed curve beginning at 11 m/s. The discrepancy increases with wind speed and the maximum difference is only 4% at 22 m/s. Below 3.7 m/s where the shaft speed is increasing, there is no noticeable difference. Thus, the variable speed test plan has a small but acceptable effect. This should be kept in mind when discussing results, but is still a worthwhile endeavour. The proposed test plan is therefore deemed acceptable. See table 5.2 for an outline of the experimental plan used to produce the performance curves.

The general procedure for power measurements was to set a common fan speed for all six fans which would result in a relatively constant wind speed across the rotor plane. The fans are variable frequency drives which are adjustable from 0 to 60 Hz. Most of the data points were generated by holding the rotor speed constant at 200 rpm (the design speed) and increasing the fan speed from 20 Hz to 60 Hz in 2 Hz increments. In order to fill out the C_P vs λ and power curves, points were also gathered at off-design rotor speeds as mentioned above. To accomplish higher tip speed ratios, the fans were held constant at 20 Hz and the rotor speed was increased

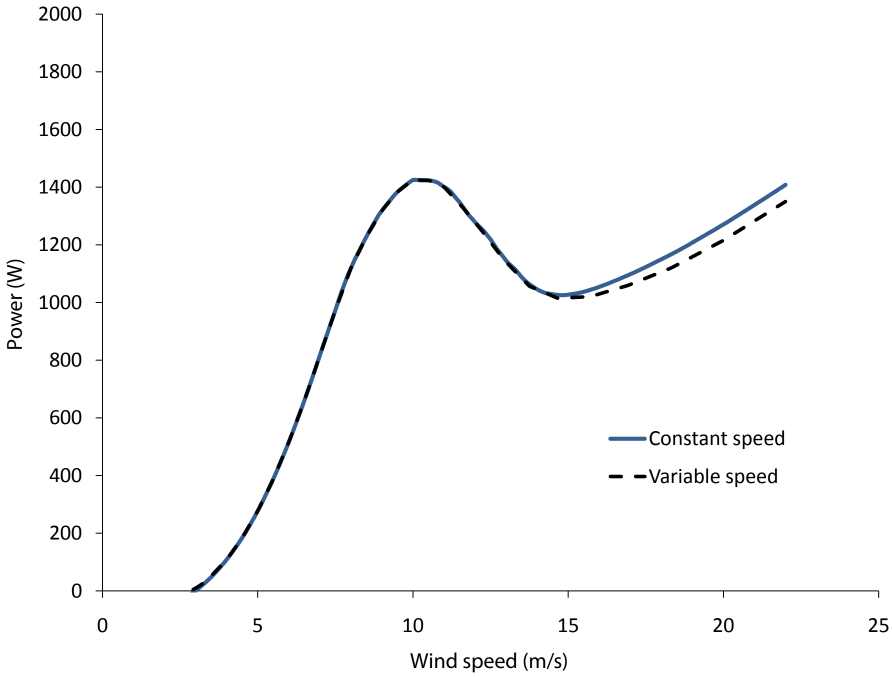

Figure 5.8: Estimated effect of variable shaft speed on power curve.

from 200 rpm to 240 rpm in 10 rpm increments. To produce lower tip speed ratios, the fans were held constant at 60 Hz and the rotor speed was decreased from 200 rpm to 100 rpm in 10 rpm increments. Measurements of wind speed, shaft speed, air temperature, and power at the load were gathered over 3 to 5 minutes at each operational point. The data sets at each operational point were then analyzed using the data reduction method outlined in section 6.2.1.

Fan freq (Hz)	Number of points	Wind Speed (m/s)	Rotor speed (rpm)	Tip speed ratio	Equivalent wind at 200 rpm (m/s)
20	4	3.7	240 - 210	10.9 - 9.5	3.1 - 3.5
20 - 60	21	3.7 - 11.1	200	9.1 - 3.10	3.7 - 11.1
60	10	11.1	190 - 100	2.9 - 1.5	11.6 - 22.1

Table 5.2: Experimental plan.

Chapter 6

Results and Discussion

This section will outline the results of the experimental work and discuss their significance. First to be reviewed is the preliminary testing phase which was necessary to determine and resolve rig and facility deficiencies and determine data accuracy and repeatability. Secondly, the performance of the baseline rotor (that with standard tips) will be presented and compared to the two BEM model predictions. Finally, the performance of the rotor with each of the two sets of winglets will be compared to the baseline case. Experimental uncertainties are also presented for selected data.

6.1 Preliminary testing

A great amount of testing was performed before the final performance data sets were gathered. This is because of the myriad issues that were discovered relating to the rig and wind facility, for which solutions had to be generated in order to produce useful results.

6.1.1 Qualitative results

The testing phase yielded several findings that are not necessarily reflected in the data. The most important observation was that there were no instances in which a tip came loose or disconnected from the blade. This was very important to the success of the rest of the project, and proves that the three-pin cam lock system works in operation. The blade dynamic balancing procedure was also found to be successful. With the previous set of blades, the rig could only operate to 220 rpm before visible vibrations of the nacelle became apparent. With the new blades, operation up to

260 rpm was possible before such vibrations surfaced. It was also found that the drivetrain losses were directly related to the temperature of the 6 bearings used to support the 3 shafts of the transmission. Warmer bearings result in warmer grease which reduces friction and hence losses. Four of the bearings were so large that they would never reach a steady-state temperature, and they were also very sensitive to convective cooling due to their exposure during testing. For this reason a temporary cowling was fashioned to reduce convective cooling and an internal space heater was installed to regulate the ambient temperature within the cowling.

6.1.2 Wind speed at rotor plane

One of the most critical parameters in generating wind turbine performance data is the speed of the wind at the rotor plane. This value must be known to the best accuracy and precision possible in order to calculate the parameters in the C_p vs. λ curve which are then used to generate a normalized power curve. Determining the wind speed in this experiment, however, was not trivial. Outdoor ambient conditions are known to affect the flow through the tunnel [63], and hence for a given fan frequency the test section speed can vary. As was discussed in section 5.3.2.1, it was necessary to take wind speed measurements upstream of the turbine during testing and use a correlation to calculate the wind speed at the rotor plane. The correlation study was performed with the test section empty so as to eliminate any effect due to the presence of the rig. Following the plan outlined in section 5.3.2.1, the correlation was determined at 5 different fan settings from 20 Hz to 60 Hz. The results of the correlation study are presented in figure 6.1.

As can be seen in figure 6.1, the velocity at the rotor plane (V_{disc}) seems to vary linearly with upstream velocity ($V_{upstream}$). Therefore a linear curve fit, which can be seen in the figure, was applied to the data. This linear relation was used to calculate the velocity at the rotor plane during the experiment. The velocity at the rotor plane is defined by equation 6.1:

$$V_{disc} = 1.1522 V_{upstream} - 0.0614 \tag{6.1}$$

Upon inspection of figure 6.1, it is also apparent that the average test section velocity increases in the downstream direction. This may be surprising considering the velocity in an open jet facility such as this should be expected to decrease with downstream distance due to jet expansion. This could indicate that the correlation indicated in figure 6.1 is incorrect. However, velocity contour maps of the test section generated previously [69] indicate that there are velocity deficit cores in between the

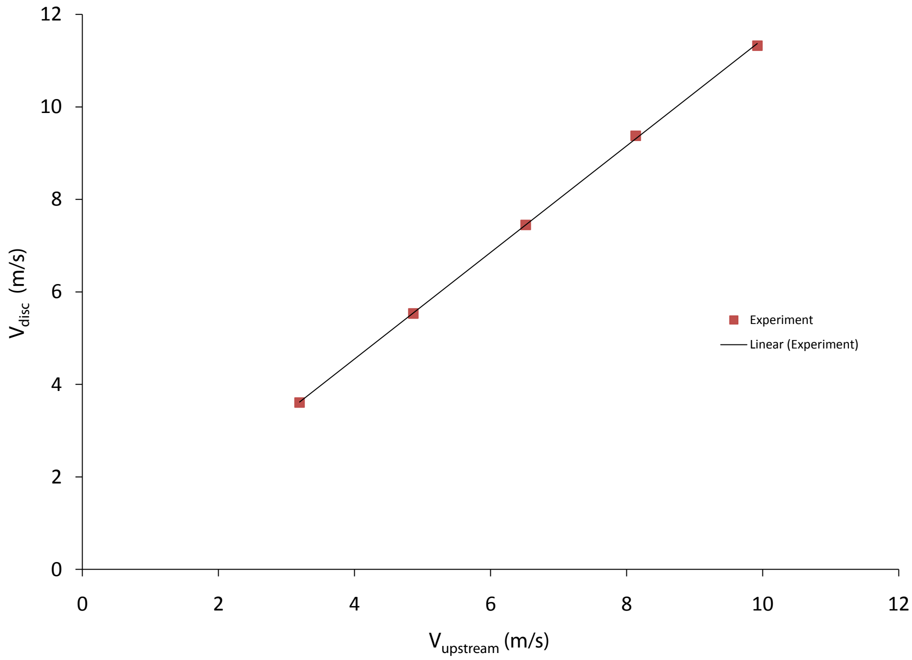

Figure 6.1: Results of correlation study between upstream location and rotor plane.

fans, and that the anemometer in the upstream location was actually placed in one of these cores. This is the reason the correlation coefficient is greater than one. The R^2 value for the linear curve fit is 0.9998 which is very close to the ideal value of 1. The uncertainty analysis (appendix E) revealed that the uncertainty on V_{disc} ranges from 3.8% at 3 m/s to 3.0% at 11 m/s; while the good R^2 value should result in the introduction of minimal error to subsequent calculations due to the curve fit.

6.1.3 Other flow characteristics

6.1.3.1 Turbulence

The turbulence intensity indicates the level of fluctuation in the velocity components of the flow and is ideally 0% for most low turbulence wind tunnel studies. A conventional wind tunnel is considered to be very good if it has a turbulence intensity of 0.5% or less. In this experiment the turbulence intensity at the rotor plane was determined using the plan outlined in section 5.3.2.2. The turbulence intensity at the rotor plane was found to vary from 5.9% to 6.2% depending on the wind speed with the average being 6.1%. The model used to predict the rotor's performance assumes 0% turbulence thus this discrepancy should be kept in mind when comparing the experimental results to the model predictions. Conversely, the turbulence intensity of outdoor wind is typically 10% or higher. Thus, using this facility to characterize the performance of wind turbines, which are inherently meant for outdoor operation, should be acceptable.

6.1.3.2 Flow deflection

Analyzing the same data set as in the turbulence measurements, the flow was found to deflect away from the test section centreline roughly 2° in both cross-stream axes at all wind speeds. The presence of the large burn house just outside the tunnel exit, which was presented in figure 5.4, could be a reason for this deflection. It presents a large blocking object to the flow and hence the flow must deflect around it. It would not be surprising if this presence is felt at least back to the rotor plane. Another possibility is that this deflection is a result of jet expansion considering the open-jet nature of the facility. In any case, this indicates another source of discrepancy between the idealized model and the experiment.

6.1.4 Drivetrain losses

As was discussed in section 5.3.1, it was necessary to estimate the drivetrain losses present while measuring the power at the load in order to establish the power generated by the rotor. The procedure used to accomplish this is outlined in section 5.3.1.

The first step was to determine the power required to spin the rotor with no wind. This was measured at varying rotor speeds so as to span the range to be encountered during performance testing. This quantity is the sum of the drivetrain losses and the power required to spin the rotor in ambient air, which is termed the rotor drag. It should be stressed here that the "rotor drag" in this case is not the same drag as will be seen during performance testing. This is simply the power required to spin the rotor in ambient air and is only required to calculate the drivetrain losses. It was required to execute each test with each different blade tip, as the drag would change for each tip. The difference in drag between the two winglets was negligible and thus one relation was established for the winglet case and one for the standard tip. It was also assumed that the rotor drag would vary linearly with ambient temperature due to it's dependence on density. For this reason the blade drag test was performed on two different days. The first day was in October and the average temperature was

10°C over the course of the experiment. The second day was in December and the average temperature was 0°C over the course of the experiment. The resulting curves are presented in figure 6.2 for the standard tip. A similar set of curves was produced for the winglet tip. Note that data was not able to be gathered at 100 rpm on the first day.

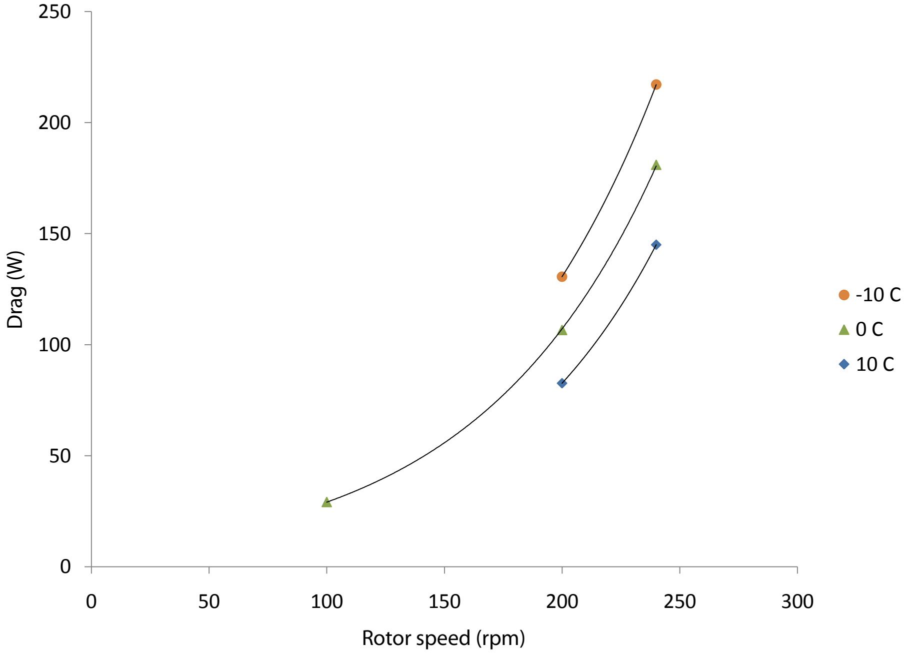

Figure 6.2: Rotor drag as a function of shaft speed and ambient temperature - standard tip.

It is clear that the drag varies with ambient temperature and with rotor speed. Exponential equations (trendlines shown) were fit to each data set such that they could be used to determine the drag for any rotor speed. The drag was then calculated during performance testing by interpolating between the curve at 0°C and the one at 10°C using the ambient temperature at the time. Unfortunately, some experiments were performed on days with a temperature below 0°C, which meant that a third curve was required at a temperature below that of the coldest day for the interpolation procedure. Since drag is known to vary linearly with temperature (this can be deduced from equation 2.2), a third curve was produced at -10°C by extrapolating the experimental drag values at 200 rpm and 240 rpm. This extrapolated curve is shown in figure 6.2.

Quantity	Label	Source	Units
Velocity upstream	$V_{upstream}$	CSAT3	m/s
Ambient temperature	T	CSAT3	°C
Ambient pressure	P	UW weather station - daily average [70]	Pa
Shaft speed	Ω	IR emitting diode, NI 6251 counter	radians/sec
Load voltage	V_l	Voltage across load	V
Load current	I_l	Voltage across in-line shunt resistor	A

Table 6.1: Measured quantities and their sources.

With a method for determining the rotor drag known, it was possible to estimate the drivetrain losses for each segment of the performance evaluation using the method outlined in section 5.3.1.

6.2 Rotor performance

Rotor performance was quantified for all rotor configurations using the plan outlined in section 5.4. Three data sets were collected for each rotor configuration so as to ensure repeatability of results.

6.2.1 Data processing

As can no doubt be deduced, several transformations had to be made to the experimental data before the final performance characteristics could be quantified. This section will present an outline of the data sources and the process followed to transform the raw data into valuable measurements. The quantities measured and their sources are outlined in table 6.1.

Performance parameters were calculated using the quantities in table 6.1. See table 6.2 for a summary of the calculations performed to determine the performance parameters.

Using the relations in table 6.2 it was possible to produce a C_p vs. λ plot for each of the 9 performance evaluation runs (3 per tip). Since it was not possible to set a desired test section wind speed explicitly, it was then necessary to produce data

Quantity	Label	Equation	Units
Wind speed at rotor plane	V_{disc}	$V_{disc} = 1.1522V_{upstream} - 0.0614$	m/s
Air density	ρ	P/RT	kg/m^3
Power at load	P_{load}	$V_l I_l$	W
Drivetrain losses	$P_{drivetrain}$	f(T, Ω, $P_{spinrotor}$, $P_{rotordrag}$). See section 6.1.4 and section 5.3.1.	W
Power generated by rotor	P_{GEN}	$P_{load} + P_{drivetrain}$	W
Tip speed ratio	λ	$\Omega R/V_{disc}$	-
Power coefficient	C_p	$\frac{P_{GEN}}{\frac{1}{2}\rho\pi R^2 V_{disc}^3}$	-

Table 6.2: Calculated parameters for performance evaluation.

points for a normalized array of wind speeds such that the data for each tip at each normalized wind speed could be averaged and the performance of the winglets could be compared to the baseline blade. Thus, an array of wind speeds at constant increments was produced and C_p was determined at each wind speed in the array by linear interpolation between the available data points. This new array of normalized C_p values was used to generate a normalized power curve at sea level standard atmospheric conditions and for the design shaft speed of 200 rpm.

6.2.2 Baseline rotor

6.2.2.1 Rotor performance vs. prediction

The performance of the rotor is ultimately described by the power curve and the C_P vs. λ plot. Since the power was calculated using the power coefficient, the C_P vs. λ plot is presented first. Figure 6.3 presents the average of the data produced over all three runs for the baseline (standard tip) case. The averaged data was produced using the data reduction method outlined in section 6.2.1. The curves predicted by the BEM model using the VTK and Aerodas airfoil data are also displayed along with the uncertainty range for each experimental data point. The uncertainty in the power coefficient ranged from ±5% to ±10%. Not surprisingly, the uncertainty was heavily dependent on the tip speed ratio; higher tip speed ratios resulted in greater uncertainty. This makes sense as for this particular experimental plan higher tip speed ratios corresponded to lower wind speeds and lower power generation. The calculation of C_P involves dividing the power by the cube of the wind speed. Hence minor perturbations in wind speed will be more influential to C_P over this range due to the lower power value, resulting in greater uncertainty.

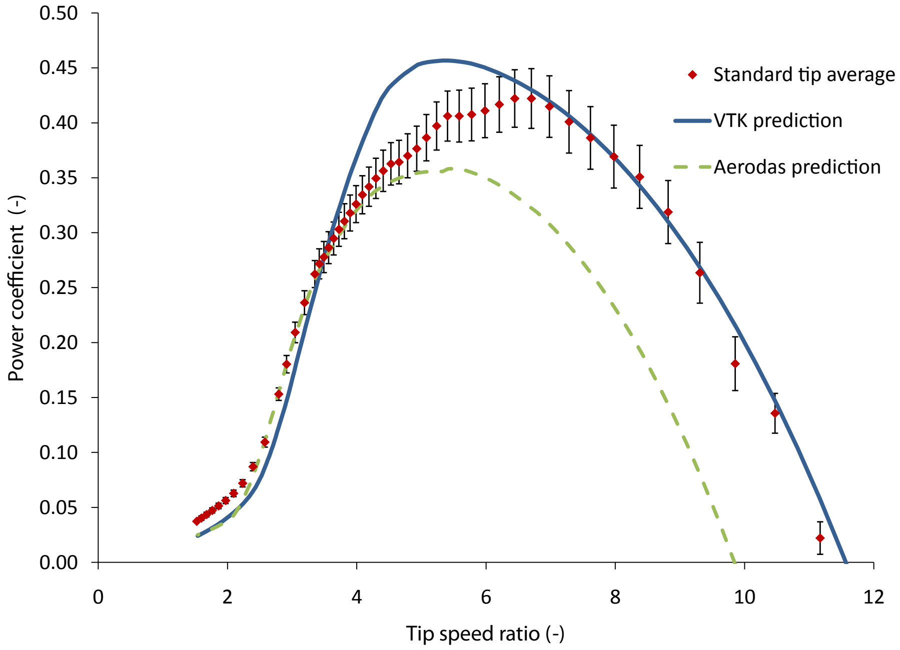

Figure 6.3: C_P vs. λ for baseline rotor.

The results indicate that the power coefficient peak ($C_{P_{max}}$) is 0.42 for $\lambda = 6.7$. This is in contrast to the VTK model's prediction of 0.46 and the Aerodas model's prediction of 0.36, both at $\lambda = 5.3$. Thus the VTK method did predict $C_{P_{max}}$ more accurately, as was hypothesized in section 3.1.5. However the rotor clearly did not behave exactly as predicted at the design point, which is indicated by the peak of the VTK C_P curve. This is significant as the performance prediction at this point was used to optimize the blade geometry. The implications of this are discussed further in section 6.2.2.2.

The Aerodas model was very successful in predicting the power coefficient between tip speed ratios of 2.5 and 4, while the VTK method predicted the performance more accurately at tip speed ratios beyond 6.5. The result is an interesting transition from the Aerodas model to the VTK model between $\lambda = 4$ and $\lambda = 6.5$. Neither model, however, was capable of predicting C_P accurately at low tip speed ratios. This behaviour is also demonstrated in the power curve, presented in figure 6.4. The curve predicted by the BEM models and the uncertainty range for each experimental data point are also presented. The uncertainty in the power data varied from ±7% at high wind speeds to ±12% at lower speeds.

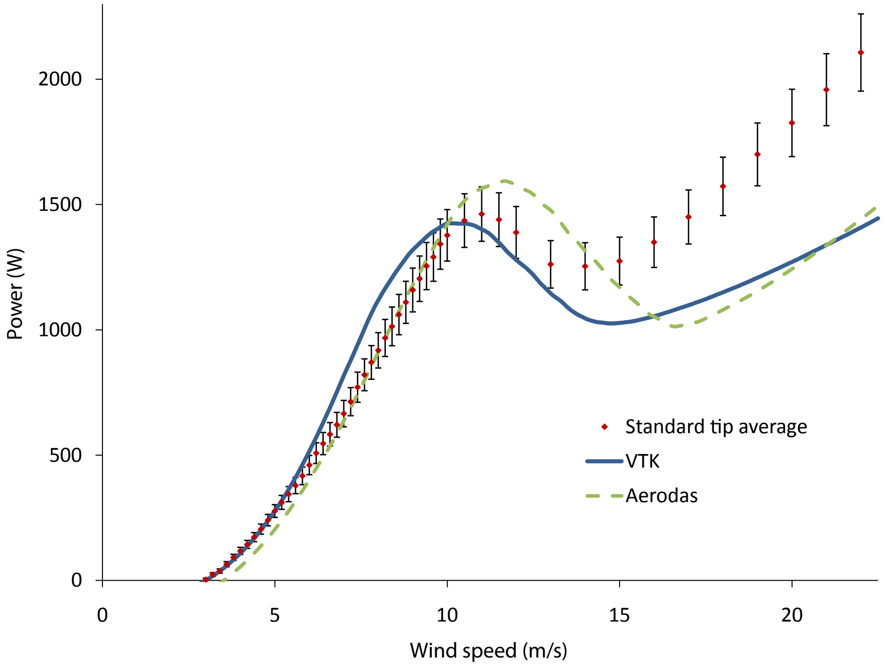

Figure 6.4: Power data for baseline rotor.

The power curve provides further insight into the performance of the two models. The transition between the two models mentioned above is clearly visible between wind speeds of 5.5 m/s and 7.2 m/s. The prediction by the VTK model follows the experimental result closely until roughly 5.5 m/s, where the prediction rises more steeply than the experimental data. From 7.2 m/s to 10 m/s, the data follows the Aerodas model quite closely. The design point lies at 6.5 m/s and hence is not perfectly predicted by either model as was seen in the C_P - λ curve. Recall that the airfoil data used in the VTK model for angles of attack up to 7°, corresponding to low wind speeds, was sourced from 2D airfoil data. This type of data is known to be reliable for performance predictions at low wind speeds when stall is not present on the blade and thus the accuracy of the VTK model at low wind speeds was expected. Clearly, however, there is something acting to reduce the power beyond 5.5 m/s which has likely been accounted for in the Aerodas model based on the more accurate prediction.

The power curve shows that the experimental data peaked at 1450 W and 11 m/s. This is close to the VTK method's estimate of 1440 W, while the Aerodas model predicted 1600 W. The wind speed at which the peak power occurred was in between the model estimates of 10 m/s and 11.5 m/s. Both models thus came fairly close to predicting the wind speed and magnitude of the power peak, with the VTK method being slightly better.

What was not obvious in the C_P vs. λ plot was the region overpredicted by the Aerodas model and overpredicted by the VTK method, which occurs for wind speeds between 10.5 m/s and 14 m/s. Both models reach minimums towards the end of this region, like the experimental data, however they are too low and occur at wind speeds too high. The experimental data reaches the minimum at 1250 W and 14 m/s compared to roughly 1020 W for the models at 14.5 m/s and 16.5 m/s.

Beyond 14 m/s the models essentially converge and reach roughly 1450 W at the cut-out speed, well below the experimental result of 2100 W. The Aerodas model does, however, seem to replicate the slope of the experimental data at high wind speeds better than the VTK method. Considering the blade was modeled as having an S834 profile along the entire span, the results are encouraging and may indicate some valuable capability to the Aerodas method. If proper airfoil data were available for the S833 and S835 a more accurate prediction would most likely be possible. It is also possible that some of the input parameters that were extracted from the 2D airfoil data to produce the Aerodas data were inaccurate. Values such as the maximum drag coefficient before stall and the slope of the linear portion of the lift curve are rather subjective and hence it is not always obvious what value to select. Possible reasons for the discrepancies between the VTK model and the experiment are many.

Beyond 7°, the point at which the onset of 2D stall begins, appropriate airfoil data was not available for input to the model. The first part of this region, corresponding to wind speeds from 8 m/s to 15 m/s and angles of attack between 7° and 20°, used airfoil data that was scaled from the results of a previous study which used a blade operating at greater Reynolds numbers and with a different airfoil. Hence it is possible that the scaling factors used were not appropriate for this blade. The remaining part of the power curve, having wind speeds in excess of 15 m/s (angles of attack greater than 20°), was modeled using the Viterna method as described in section 2.3.3.1. This model is directly dependent on the aerodynamic coefficients at 20°, which themselves included some uncertainty due to the method by which they were derived. Therefore it is unfortunate but not surprising that the prediction does not closely match the experimental result beyond 8 m/s.

It should also be considered whether the deficiencies of the rig and facility could have contributed to the discrepancies between model and experiment. Some uncertainty was introduced by the methods used to estimate the wind speed at the rotor plane and the losses through the drive train. However the uncertainty due to these methods were propagated through the calculations and the results are satisfactory. The non-zero turbulence could also have had an effect on the results. However, this effect is known to be very small [2] and is not of significance in this case due to the relatively low turbulence level. The flow deflection is also a possible cause of error. Assuming the deflection angle manifests itself as yawed flow to the turbine, however, a deflection angle of 2° is well within acceptable limits [2].

Thus it is most likely that the inaccuracies in the predictions are a result of incorrect airfoil data. The inaccurate predictions by both models is unfortunate but not surprising considering the similar documented difficulties in the results of other large-scale wind turbine performance tests discussed in section 2.4.1. Such results are relevant for comparison here as predicting wind turbine performance using BEM is almost solely dependent on the input airfoil data. Manipulations to the airfoil data, like those outlined in section 3.1.3.1, must be performed irrespective of turbine size and present a significant challenge.

Due to the nature of the Aerodas model, there are few opportunities to make adjustments to better reflect the experiment. In the case of the VTK model, however, there are.

6.2.2.2 Adjustment of VTK model parameters

The parameters that defined the airfoil data used in the model can be adjusted to determine their effect on the resulting power curve and to produce a curve that better reflects reality. In adjusting the parameters, it was first of all assumed that the region from 7° to 20° still follows the same trend: that of stall delay with the C_l values at 15° and 20° scaled by the C_l value at 7°. The values of the coefficients at 15° and 20°, however, may change. The C_d value at 20° is defined by C_l and L/D at 20°. During the design phase it was assumed that the blade would act as a flat plate beyond 20° and hence an L/D of 2.75 was used. As for the region beyond 20°, the only other parameter that affects this data is the blade AR which defines the drag maximum at

90°.

The effect of adjusting the parameters upon the model's prediction was therefore investigated. It was first of all decided to determine the reason for the discrepancy from 5 m/s onwards. It is obvious that the slope of the predicted curve needs to be reduced to align with the experiment. One hypothesis was that perhaps the blades were more rough than smooth considering that by the end of testing there was significant buildup of bugs and dirt on the blades. The performance was predicted using airfoil data for smooth blades, and drag coefficients are adversely affected by roughness [46]. To test this hypothesis, the performance analysis was performed using data for "rough" airfoils. This type of data is produced numerically by fixing the transition locations on the upper and lower surfaces of the airfoil to 0.02c and 0.05c, respectively [46]. See figure 6.5 for the results.

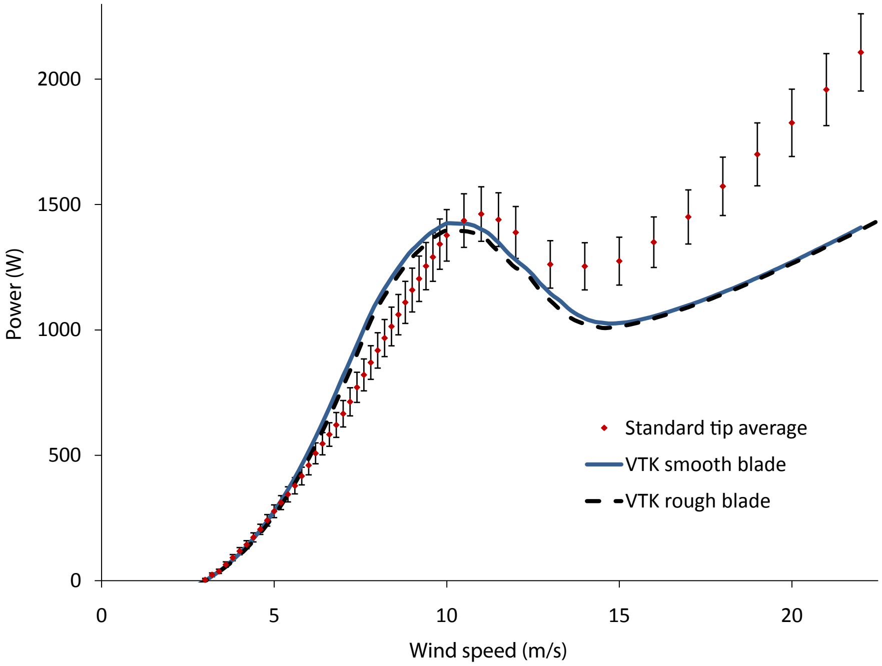

Figure 6.5: Effect of blade roughness.

As can be deduced from the figure, modeling the blade surface as being "rough" had a marginal effect, and there is still a very large discrepancy between the model prediction and the experimental result. This is not surprising considering the S83X family of airfoils was specifically designed to be insensitive to roughness affects [46], which is very important for any airfoil specific to wind turbine blades. Thus, some other adjustment was required to better predict the initial portion of the curve. The required adjustment was actually found to be that specified by Viterna [20], and outlined in section 2.3.3.1.

This method called for an adjustment of the 2D airfoil data to account for finite blade effects. This was not originally performed since the refined method of Tangler and Kocurek [21] (section 2.3.3.2) was followed, which used 2D airfoil data below stall and produced very good results. In this case, however, the adjustment suggested by Viterna was found to increase the accuracy of the prediction. Applying the adjustments outlined in section 2.3.3.1 to the 2D airfoil data produced the desired effect of reducing the predicted power such that it followed the experimental data far more closely than before over the moderate wind speed range (6 m/s to 10 m/s). Figure 6.6 shows the effect of adjusting the 2D airfoil data (that below 7°) to account for finite blade effects. In this case, the data was adjusted for an AR of 10.9. The AR for the 2D data corrections (AR_{2D}) was calculated using Tangler and Kocurek's recommendation of using the ratio of the blade length to the chord at 80% radius.

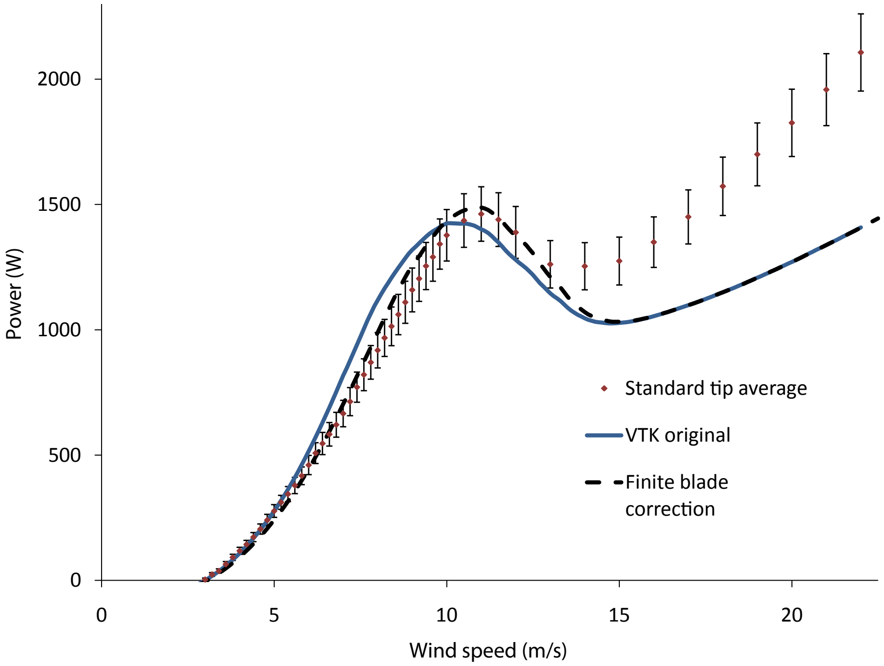

Figure 6.6: Effect of accounting for finite blade effects on 2D data.

It is clear from the figure that correcting the 2D data had the desired effect reducing power at moderate wind speeds and increasing power from 10 m/s to 15 m/s such that the prediction follows the experimental data more closely. At wind speeds below 10 m/s the new prediction actually looks similar to the Aerodas model. This is not surprising considering, as was mentioned previously, the Aerodas model altered the aerodynamic coefficients below stall in a manner similar to this adjustment. Considering one of the inputs to the Aerodas model was the AR, it is clear that such corrections are incorporated in that model. It was also found that the slope of the VTK predicted curve over the moderate wind speed region decreases with AR. This makes sense upon inspecting the applied equations (2.29, 2.30, and 2.31). Decreasing the aspect ratio increases C_d and α for a given C_l, thus decreasing torque and hence power for a given blade α.

It should also be noted that while the correction for 3D effects makes the prediction more accurate at wind speeds above 6 m/s, the prediction actually suffers below this speed. This is likely because the strength of the tip vortex (and hence the influence of 3D effects) is proportional to the lift coefficient. The angle of attack and hence lift coefficient increases with wind speed, hence 3D effects are not as prevalent at lower wind speeds. Thus it is possible that at higher wind speeds and lift coefficients the data should be corrected for the increasing influence of the tip vortex, whereas at lower speeds unmodified 2D data is more appropriate. This is very well illustrated in the C_P vs. λ plot in figure 6.3. The original model, that without finite blade corrections, predicts C_P very well at tip speed ratios above 7. Between 4 and 7, however, the experimental C_P data is clearly below the prediction. It is fairly obvious, then, that corrections for 3D effects should be implemented at moderate wind speeds (and hence angles of attack) but not below. This result also complicates the design approach slightly. Following established convention [21], the blade geometry was optimized assuming the uncorrected 2D airfoil data was valid at the design point. Meanwhile the results indicate that this data is only valid above $\lambda = 6.7$, while the design point was at $\lambda = 5.3$. It should be noted, however, that in this case the design point was at the very high end of the available 2D airfoil data and that the data was not sourced from wind tunnel tests but from an analytical code, as mentioned in section 3.1.3. Analytical codes are known to have difficulty predicting airfoil performance close to stall and hence it is possible that the data used at the design point was not entirely representative of the actual behaviour of the airfoils. Nonetheless, the prediction was able to be improved upon by correcting the 2D data for finite blade effects.

Having determined the method by which to correct for the discrepancy in the linear portion of the curve, the other required corrections were addressed. Notably, the peak power at 11 m/s, the subsequent minimum at 14 m/s, and the slope beyond 14 m/s.

	Original model	Adjusted model
AR_{2D}	infinite	10.9
$\frac{C_{L_{15^\circ}}}{C_{L_{7^\circ}}}$	1.44	1.225
$\frac{C_{L_{20^\circ}}}{C_{L_{7^\circ}}}$	1.34	1.2
L/D at 20°	2.75	3.1
$C_{d_{90^\circ}}$	1.31	2.01

Table 6.3: Parameters used in model prediction.

To align the peak at 11 m/s and the subsequent valley at 14 m/s, the scaling factor at 20° ($\frac{C_{L_{20^\circ}}}{C_{L_{7^\circ}}}$) was decreased from 1.34 to 1.2 and the scaling factor at 15° ($\frac{C_{L_{15^\circ}}}{C_{L_{7^\circ}}}$) was decreased from 1.44 to 1.225. In addition, the L/D at 20° was increased from 2.75 to 3.1. These adjustments allowed for far better agreement between the model and experiment from 10 m/s to 15 m/s. During this process the power curve was found to be very sensitive to the L/D value at 20°. Even the slightest increase would result in far greater predicted power at high wind speeds. This is because it is used to set the C_d value at 20° which essentially determines the entire drag profile beyond 20° due to the use of it as an input to the Viterna model. It is very clear that the drag has a dominant effect on the predicted power at high wind speeds.

To increase the slope in the power curve from 15 m/s onwards, it was necessary to increase the drag coefficient at 90° ($C_{d_{90^\circ}}$). It was increased from 1.31 to 2.01, which is the theoretical maximum of a blade of infinite span. It may seem counter intuitive to increase the drag coefficient in this context, however this value is used in the Viterna [20] model to calculate the lift and drag coefficients, and increasing it results in a greater rate of ascent in the power curve at high wind speeds.

The effect of disabling the hub and tip loss model was also explored based on the recommendation of Viterna [20]. Significantly better results were found, however, by leaving it on, which is in agreement with Tangler and Kocurek [21]. Considering the multitude of variables, the power curve adjustment process was iterative in nature. In the end, the curve was not able to be perfectly predicted, but the result was fairly close. See figure 6.7 for the final predicted power curve, and table 6.3 for a comparison of the original and adjusted parameters.

Having made the adjustments outlined in table 6.3, the model comes far closer to predicting the experimental result. From 3 m/s to 6.5 m/s the power is under predicted by a maximum of 21%, while in the region from 6.5 m/s to 11 m/s it is over

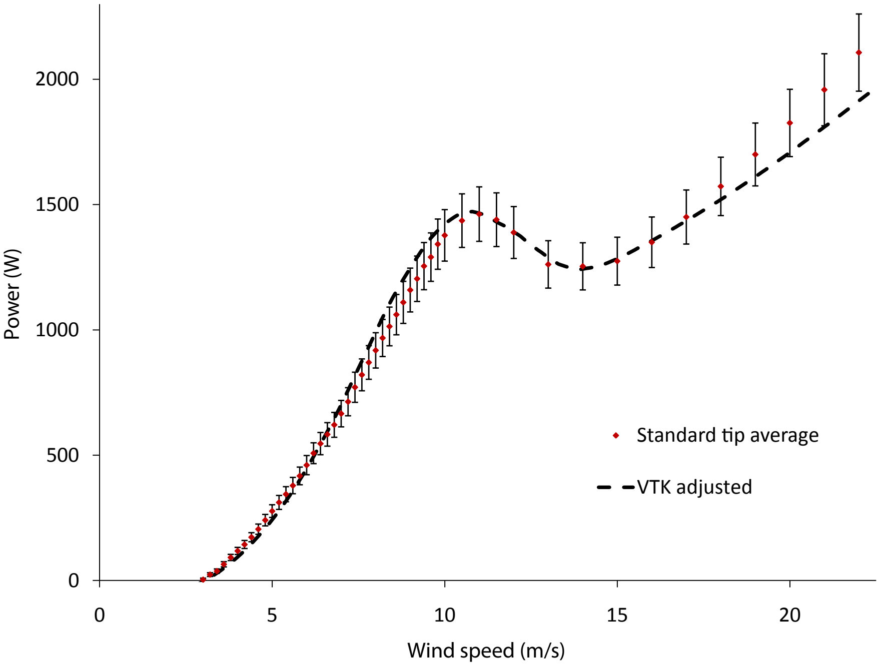

Figure 6.7: Power curve for baseline rotor with revised model.

predicted by a maximum of 9%. The peak power of 1450 W is correctly predicted at 11 m/s. From 11 m/s to 15 m/s the prediction differs with the experimental data by at most 2%. Finally, the increasing trend beginning at 15 m/s has a reduced slope compared to that of the experimental data. The maximum difference is 9% at the cut-out speed.

It should also be considered whether the adjustments to the model parameters are physically valid. Firstly, the finite blade corrections applied to the airfoil data below stall were based on the Viterna model, and the AR_{2D} value was set to 10.9 as per the recommended method of Tangler and Kocurek [21] thus this adjustment is acceptable.

The scaling factors at 15° and 20° were originally set based on the trends in the study of Tangler and Kocurek [21] which used a blade with the S809 airfoil. It was thought that since both blades shared the same AR and the S809 and the S83X series airfoils were designed for use on wind turbine blades, that perhaps they would display similar behaviour in the post-2D-stall regime. Based on the experimental results of this study that is not exactly the case. While the general trend of a C_L peak at 15° remained the same, the scaling factors at 15° and 20° were both decreased. This could simply indicate that the combination of the blade geometry, the S83X airfoils, and the operational conditions resulted in less significant rotational augmentation than was observed for the UAE blade. It is also notable that the resulting peak C_l values at 15° are between 1.1 and 1.4, while that given for the UAE blade was 1.3. The C_d values at 20° are also close at between 0.37 and 0.49 for the research blade and 0.43 for the UAE blade. These similarities indicate that the parameters used in the adjusted model are likely physically valid and acceptable.

The alteration of the L/D value at 20° is also significant. It was originally set to 2.75, that of a flat plate, and increased to 3.1. Viterna [20] and Tangler and Kocurek [21] both found that the L/D profile of a wind turbine blade was similar that of a flat plate beyond 20° angle of attack. However, the L/D at 20° in the Tangler and Kocurek experiment was actually 2.83 and thus was not exactly equal to that of a flat plate. Additionally, this adjustment only introduces a slight change to the L/D profile. Illustrating this point is the fact that the L/D value at 45°, which for a flat plate is 1, only drops to 0.97 with this adjustment. Finally, there is clearly a difference in geometry and conditions between a flat plate in a 2D wind tunnel and a rotating tapered and twisted wind turbine blade. It can thus be concluded that this adjustment does not introduce a significant change to the behaviour of the blade in the post-stall region. While it is not being modeled as behaving exactly as a flat plate, it is still very close.

The last parameter that was altered is $C_{d_{90^\circ}}$. This parameter determined the slope of the power curve from 15 m/s onwards. $C_{d_{90^\circ}}$ was increased to 2.01, which is the value for a flat plate of infinite span at 90° angle of attack. Modeling the blade as having an infinite span over this region is not unreasonable as the tip and hub loss models were left activated and hence finite blade effects are still accounted for. As can be seen in figure 6.7, however, even with this adjustment the slope of the model's prediction is low compared to the experimental result. A method was found to predict the slope very accurately, however it was only possible to achieve the desired slope for this region by increasing $C_{d_{90^\circ}}$ beyond 2.01. This increase, however, cannot be justified physically as the drag coefficient of a normal flat plate at 90° is known to have a maximum of 2.01 [71]. The drag coefficient at 90° was thus left at 2.01 despite the resulting discrepancy in the model's prediction. Recall from figure 6.4 that the Aerodas model actually predicted the slope in the high wind speed region quite well, although the magnitudes are clearly below the experimental result. This would indicate that the trend in the airfoil data at high angles of attack is likely more accurate for the Aerodas model. Additionally, as was mentioned in section 2.3.3.1, the Viterna model was derived assuming constant shaft power beyond stall. Thus it is not surprising that no valid adjustments were possible for the VTK method that would increase the slope of the power curve prediction at high wind speeds to match the experimental result perfectly. Perhaps if the model were derived again without this constant power assumption it would be more capable of predicting such an increasing trend in the power curve at high wind speeds.

The process of adjusting model parameters arbitrarily to better predict the experimental results is clearly an inexact science. This study adds to the mounting evidence that more advanced methods are needed for predicting wind turbine performance curves, which is in clear agreement with the literature.

6.2.2.3 Grading the model

Although the curve has been qualitatively validated and the model adjustments physically supported, effort should be made to quantify the difference between the predicted and actual performance. This would provide tangible evidence that the prediction does provide the necessary information and in fact reflects the performance of the rotor to a certain degree.

There are specific areas of the power curve that are important to predict correctly to ensure the success of a design campaign. The rated power, which is typically the power at 11 m/s, is one important part. According to figure 6.7, the power is predicted within the bounds of experimental uncertainty at 11 m/s which is encouraging. The other important piece of information is the maximum rotor power. It is important to predict this value accurately to ensure that the generator is not powered beyond it's rating. However it is also desirable to operate as close to that rating as possible to maximize energy capture. The model predicted a maximum power of 1910 W as compared to the experimental result of 2100 W. This represents an under prediction of 9%. Recall also that the variable speed nature of the test plan was predicted to underestimate the actual maximum power by roughly 4%. Thus the actual maximum power is likely closer to 13% greater than the model's prediction. This discrepancy would have to be kept in mind if this were a design effort for a production turbine.

To the owner, the power curve's importance ultimately lies in the prediction of the AEP of the turbine, as was mentioned in section 2.6. This quantity determines how much revenue the turbine owner can expect for a given year, and affects the economic analysis tremendously. Thus a good estimate of this quantity is essential.

Using the method outlined by Burton et al. [2], the annual energy capture of the rotor was estimated for various wind speed classes using the experimental and predicted power curves. See table 6.4 for a summary of the results.

The results show that the model is able to predict the AEP of the rotor to within no worse than 1.5%. Note that the model consistently over predicts the AEP. This is

IEC wind class [2]	Annual average wind speed (m/s)	AEP (kWh)		
		Experiment	Model prediction	% difference
I	10	8184	8235	0.6
II	8.5	7195	7286	1.3
III	7.5	6291	6388	1.5
IV	6	4585	4639	1.2

Table 6.4: Annual energy production estimates. Wind classes from Burton et al. [2].

likely due to the fact that, as is shown in figure 6.7, the model is over predicting the power between 6.5 m/s and 11 m/s. The fact that the model under predicts beyond 18 m/s likely has little effect since the probability of winds occurring at those speeds is quite low. Despite the slight error, the discrepancies in table 6.4 are acceptable. The AEP estimate results are encouraging and prove that the model's power predictions can produce acceptable estimates of AEP.

Having established the performance of the baseline rotor and adjusted the model to better reflect it, the performance of the rotor with winglets will now be analyzed.

6.2.3 Rotor performance with winglets

In addition to the rotor with standard tips, that is, the baseline rotor, performance data was gathered with each of the two sets of winglets. The first winglet, labeled Maniaci, was designed by David Maniaci at Pennsylvania State University using a vortex analysis method and is described in section 3.2.1. The second winglet, labeled Gertz, was designed by the author based on trends in the literature and discussions with Maniaci. It is described in section 3.2.2. Experimental data was gathered and processed using the same methods as for the standard tip, which allowed each winglet configuration's performance to be compared to that of the baseline rotor.

6.2.3.1 Maniaci winglet

The experimental power curve of the rotor with Maniaci winglets is shown in figure 6.8 along with the performance of the baseline rotor for comparison.

It is clear that the winglet had an effect on some regions of the power curve. To better illustrate the effect, the power augmentation was calculated. The results are displayed in figure 6.9 along with the performance predicted by Maniaci [57].

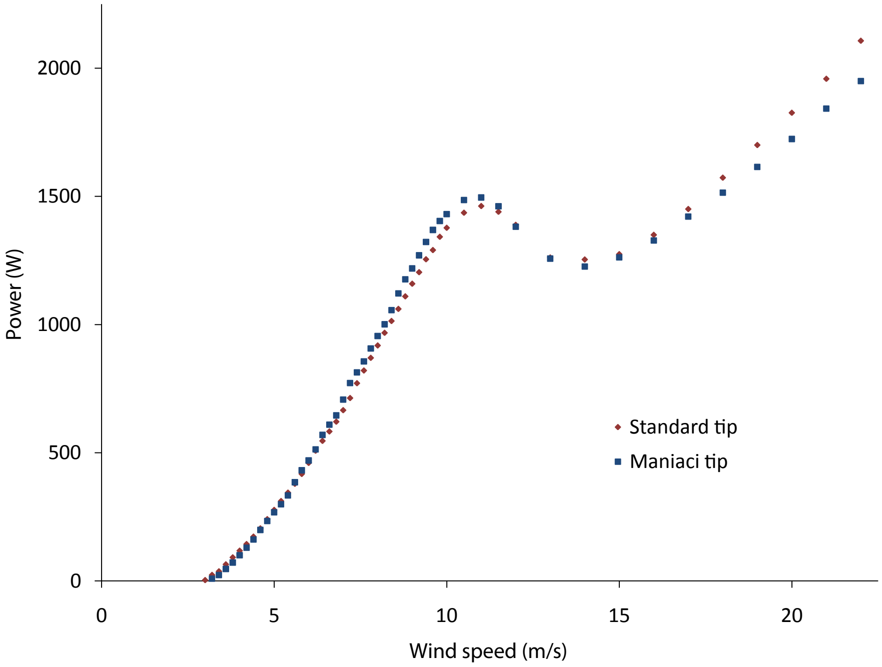

Figure 6.8: Experimental performance of rotor with Maniaci winglets.

The results indicate that the winglet does have a beneficial effect between wind speeds of 5.6 m/s and 11.5 m/s. Although the data is scattered, the general trend indicates that the power augmentation reaches slightly above 5% for wind speeds between 6.5 m/s and 9.5 m/s while declining sharply below 6.5 m/s and gently above 9.5 m/s. It also has a negative effect at wind speeds below 5.6 m/s and above 11.5 m/s. Maniaci [57], meanwhile, predicted the trend fairly accurately up to 9 m/s, although the magnitude is clearly over predicted above roughly 6 m/s. The model predicted the power augmentation to plateau at roughly 10% for wind speeds above 6 m/s. Although the experimental data shows a rough plateau up to 9.5 m/s, the power augmentation drops off beyond that point, which was not predicted by the model. It is worth noting, though, that the performance does not drop off as steeply at high wind speeds as it does at low wind speeds.

Next, the performance of the Gertz winglet will be analyzed.

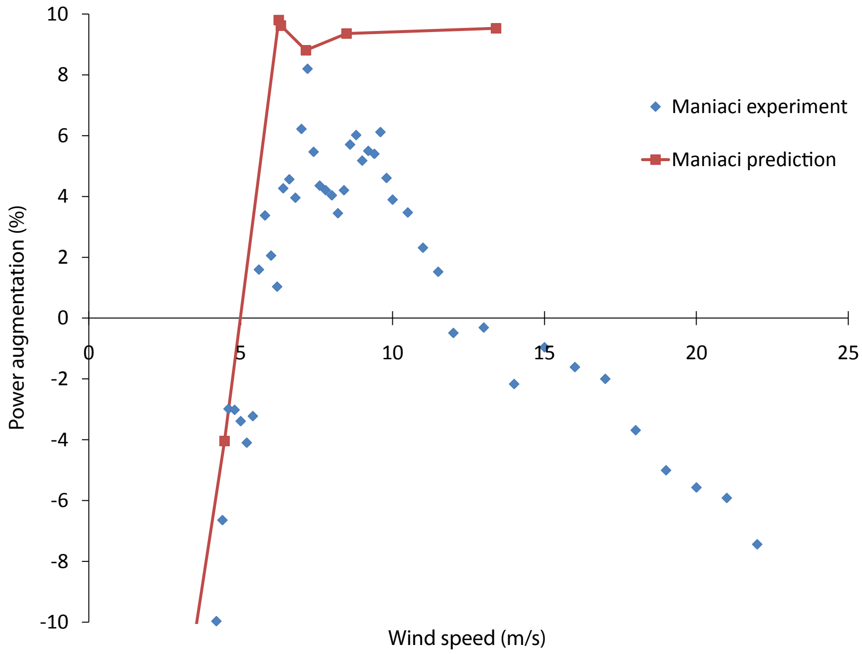

Figure 6.9: Power augmentation for Maniaci winglet. Prediction adapted from Maniaci [57].

6.2.3.2 Gertz winglet

The Gertz winglet was analyzed in the same way as the Maniaci design. For the effect of the winglet on the power curve, see figure 6.10.

The results are clearly very similar to the Maniaci design. This is not too surprising considering the similarities between the two winglets. Recall from section 3.2 that they share the same airfoil, cant angle, sweep angle, and height. Figure 6.11 shows the percentage power augmentation over the operating range. The Maniaci winglet's performance is also provided for comparison.

The power augmentation plot shows the difference between the two winglets more readily. At wind speeds below roughly 6 m/s the Maniaci winglet performs slightly better, however from 6 m/s to 10 m/s the Gertz design is superior. It displays a more steady behaviour over this region consisting of a rough plateau just above 5%. The two are very close from 10 m/s to 14 m/s after which point the Gertz design is consistently better. In section 3.2 it was hypothesized that the Gertz winglet would perform better at low speeds and worse at high speeds. The results indicate that the

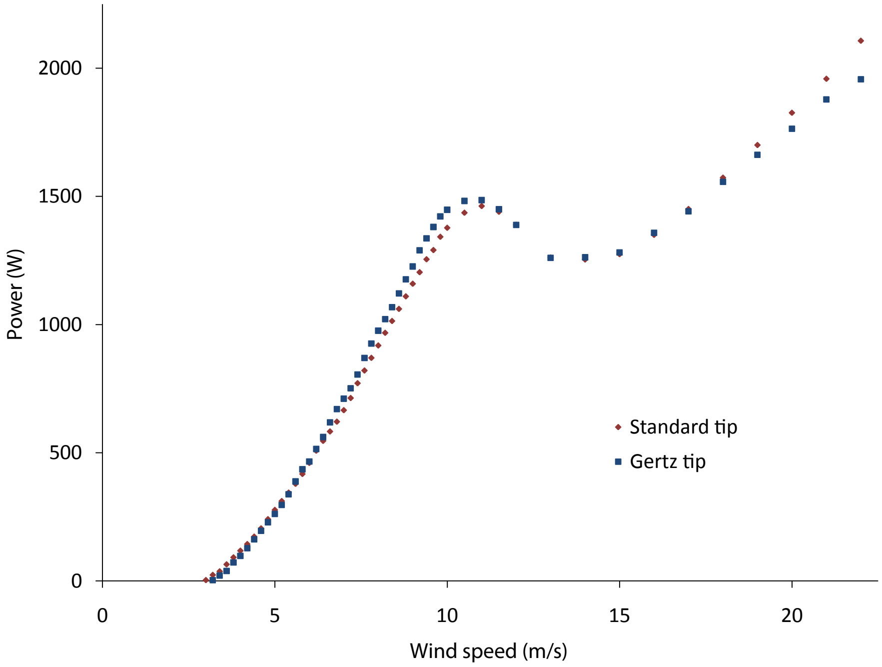

Figure 6.10: Rotor performance with Gertz winglet compared to baseline case.

Gertz winglet does perform better between 6 m/s and 10 m/s, but also from 14 m/s onwards.

6.2.3.3 Discussion of winglet results

Significance of winglet performance Considering the literature indicated power augmentation of 2% to 8% could be expected, the experimental results having peak values of just above 5% are justified. The shape of the power augmentation curve is also consistent with the related studies discussed earlier. Recall from figure 2.27 that the Mie tip vanes augmented power over the central part of the operating range while reducing it elsewhere. This same trend was displayed in the power augmentation results in figure 6.11. The bell-shaped nature of the power augmentation curve is also not surprising considering the remarks of Maughmer [36] regarding the realities of winglet design. He said that a winglet can only be optimized for one operating point. Thus the challenge is to establish a design that is optimized such that it has a net positive effect over the operating range of the wing or blade. The bell-shaped nature of the curve in figure 6.9 could also be very useful. This is due to the similar shape of

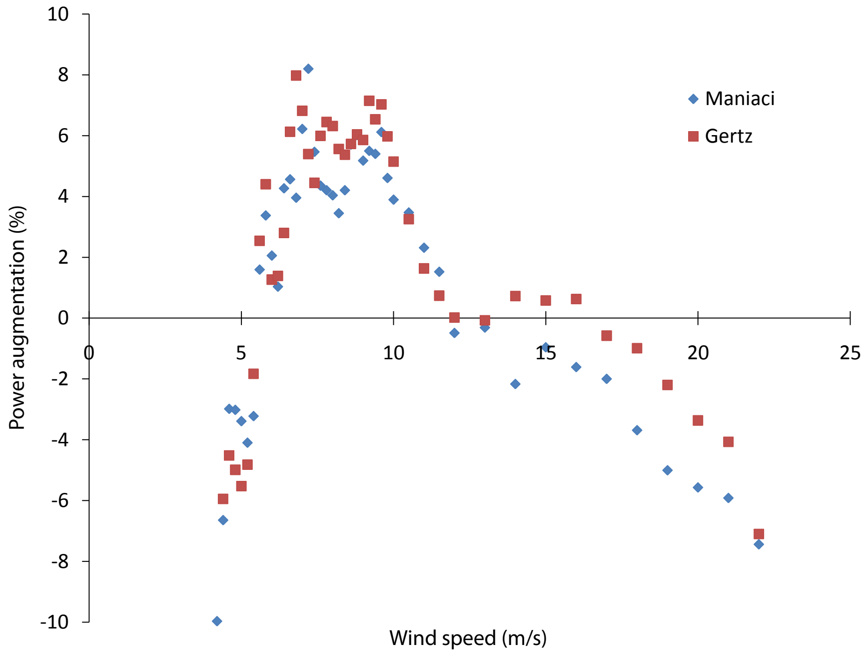

Figure 6.11: Power augmentation comparison of Gertz and Maniaci winglets.

the wind speed probability distribution. Recall figure 2.28 which presented the wind speed probability distribution for a site with an annual average wind speed of 6 m/s.

It seems as though, in theory, the power augmentation curve could be aligned with the peak of the wind speed distribution curve. This would maximize the benefit of the winglet by increasing power output over the range of most probable wind speeds. The detrimental effect of the winglet would be minimized since it would occur for less probable wind speeds. Thus, for a given rotor, a custom winglet could be designed for each wind class to maximize its benefit in that particular resource.

The results indicate that winglets can be effective over a specific operating range. To quantify the value of the winglets, an AEP estimate was performed. The AEP measure quantifies the value of the winglet to the turbine owner as was mentioned earlier. In performing the analysis, it was decided to test the hypothesis that a winglet should theoretically be optimal for a unique wind class (i.e. annual average wind speed). Thus, the AEP calculation was performed for a range of annual average wind speeds. The results are presented in figure 6.12 in the form of percentage increase in AEP compared to the baseline case.

It is clear from figure 6.12 that the hypothesis was correct. The Maniaci winglet

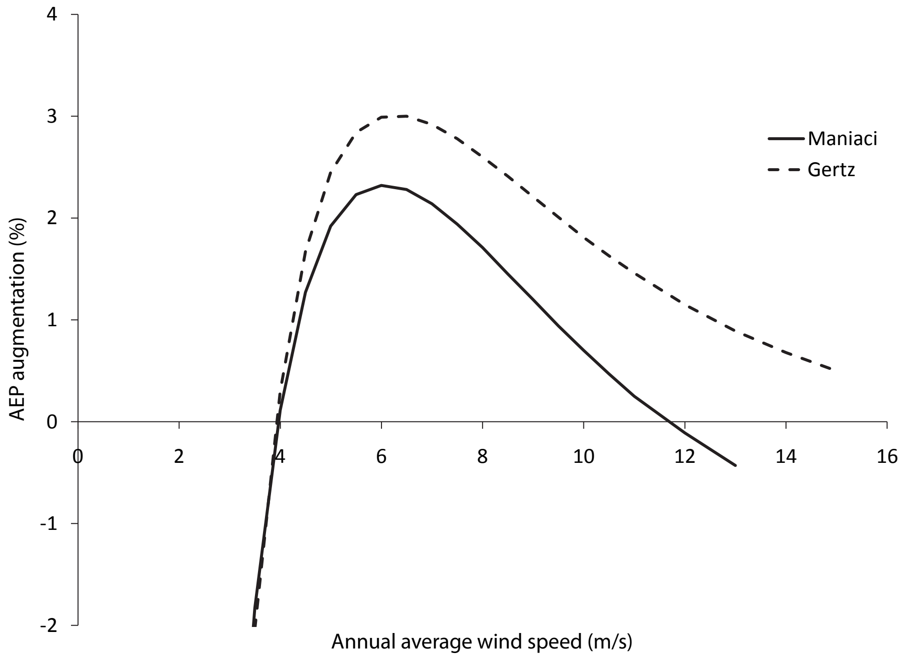

Figure 6.12: Percentage increase in AEP at different annual average wind speeds.

seems to be optimal for a wind class with an average annual wind speed of 6 m/s (IEC class IV). The curve peaks at 2.3% and falls off on either side. The curve has the same shape as the power augmentation curve presented in figure 6.9, which is not surprising for obvious reasons. It is also encouraging that the AEP augmentation is only negative for annual average wind speeds below 4 m/s and above 12 m/s. Considering there are no IEC classes defined below 6 m/s or above 10 m/s, those average wind speeds are likely less common. It can thus be concluded that the Maniaci winglet would likely not introduce any detrimental effects to AEP in any realistic wind regimes, and is optimal for IEC class IV.

The Gertz winglet provides equal or greater AEP augmentation than the Maniaci design for the majority of the cases evaluated. The AEP is increased by a maximum of 3% at an annual average wind speed of 6.5 m/s; close to the peak of the Maniaci curve at 6 m/s. The superior performance of the Gertz winglet is likely due to the design differences between the two winglets. This will be discussed in detail in the next section.

Whether an increase in AEP on the order of a few percent is worth the effort of designing and incorporating winglets into a wind turbine rotor design is another matter. For this particular turbine, assuming a price of electricity of \$0.13/kWh, an increase in energy production of 3% would yield an additional return of \$18 and \$30 annually for IEC wind classes I and IV, respectively. The net present value of the total increased return for each wind class is \$223 and \$398 assuming an interest rate of 5% and turbine lifetime of 20 years. Considering the average total installed cost for a turbine of this size is roughly \$12000 [72], it is arguable whether it is worth the effort of incorporating the winglets in the first place. However, considering the preliminary nature of this study, the winglets tested likely do not represent the greatest performance improvement possible. Considering the findings of Shimizu [6], which claimed power augmentation of up to 8%, far greater performance could possibly be achieved with more optimal designs should an iterative winglet design and testing program be executed. Indeed, the results thus far are encouraging and the winglet proposal certainly deserves further investigation.

A more theoretical advantage of the winglet configuration is the effect of reducing power at high wind speeds which could be beneficial to a turbine design campaign. In the case of a stall-regulated turbine such as this, the maximum power is limited by the generator rating, and the maximum power typically occurs at the cut-out wind speed (as can be seen in figure 6.8 and figure 6.10). The ideal scenario is for the power curve to plateau at the rated wind speed, enabling the maximum rating of the generator to be used over a wide range of wind speeds. Thus, reducing the power at high wind speeds, which the winglet is seen to do, is actually beneficial because it would allow design modifications that would shift the power curve up thus increasing energy capture at lower, more probable wind speeds. Both winglets reduce rotor maximum power by roughly 8%. Thus, the power curve could theoretically be shifted up by 8% without exceeding the maximum power of the standard tip configuration. This effect is illustrated in figure 6.13 for the case of the Maniaci winglet.

The power is clearly increased significantly over the majority of the power curve. This would of course result in a greater AEP, which is the ultimate goal. The resulting augmentation in AEP due to the power curve shift is presented in figure 6.14 with the original AEP augmentations presented for comparison.

The projected increase in AEP is quite significant for the case of the shifted power curve. Both winglet designs exhibit peak AEP increases of above 10%. Economically speaking, an increase in annual energy capture of 10% would have net present value of between \$743 and \$1326 for this turbine, again depending on the wind regime. These values would perhaps make the winglet proposal more attractive, depending on the additional cost of incorporating them into the design.

It should be noted that this is a very speculative analysis. It assumes that the geometry of the blade could be altered so as to shift the entire power curve up by

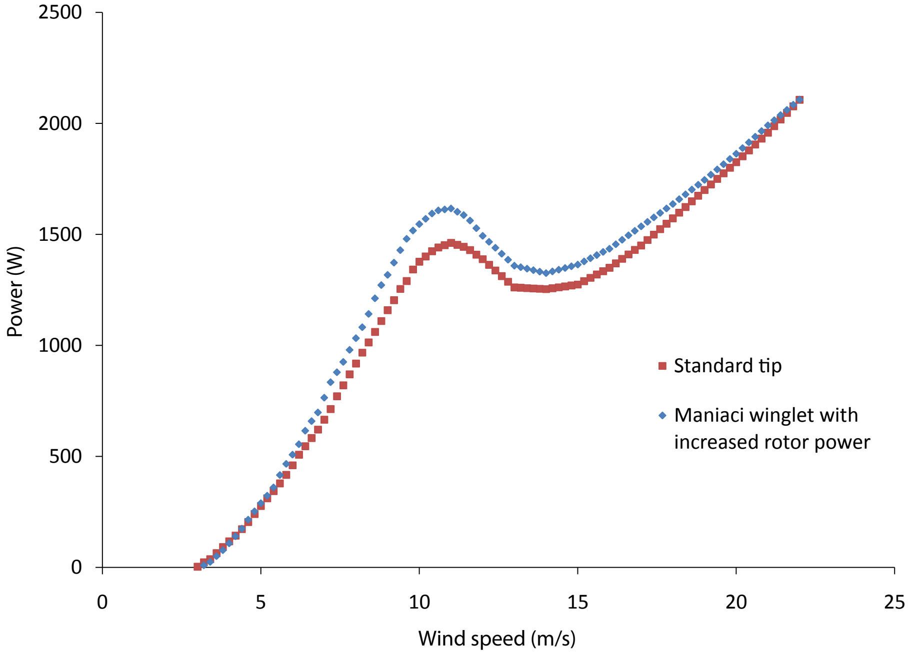

Figure 6.13: Possible theoretical improvement in power curve due to winglets.

8%. In practice, the rated power can be increased by increasing the design wind speed (that at which the blade performs most efficiently). This results in reduced performance at lower wind speeds which is not accounted for in the data presented in figure 6.13 and figure 6.14. Additionally, it is possible that the basis of the study, that is, a reduction in maximum power of 8%, was exaggerated due to the experimental plan used to produce the power curve in the first place. Recall that the rotor was actually slowed down incrementally from 200 rpm to 100 rpm to generate the data in the region above 11 m/s. As mentioned previously, this reduces the Reynolds number incrementally as well. Since the drag coefficient increases with decreasing Reynolds number, the high wind speed region of the power curve was therefore generated with the winglet exerting greater relative drag on the rotor than it would have at 200 rpm. This could have resulted in exaggerated power reduction at high wind speeds. This could also indicate that perhaps Maniaci's power augmentation predictions at high wind speeds are not so erroneous.

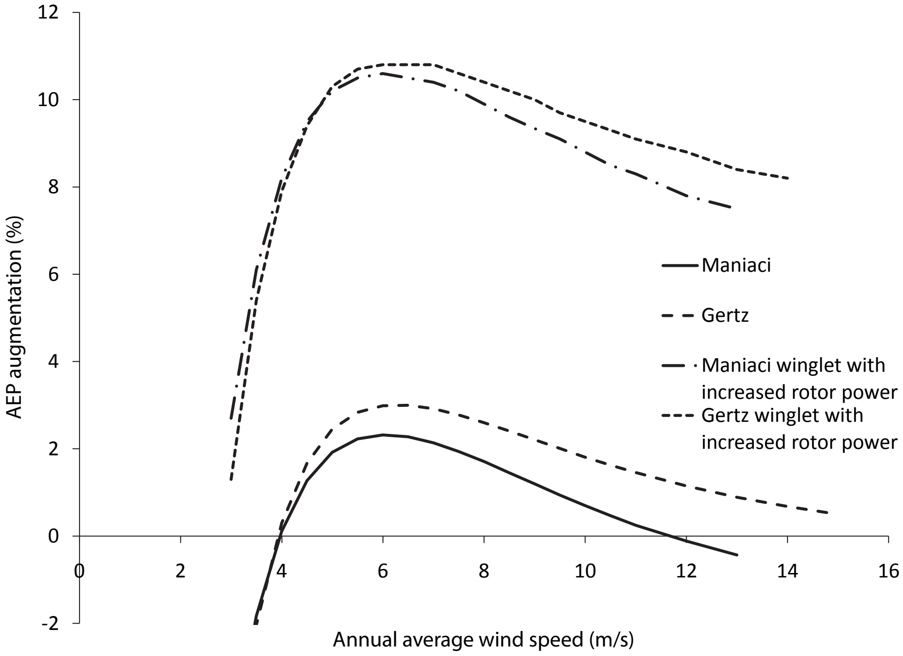

Figure 6.14: AEP augmentation due to power curve shift.

Maniaci vs. Gertz design As was mentioned in section 3.2.3, the main differences between the Maniaci and Gertz winglets are the toe and twist angles and the planform shapes. Figure 6.15 displays an illustration of the difference between the two winglets with respect to toe and twist. The velocity components incident to the winglet are also presented. In figure 6.15, V_r is the velocity component due to the rotation of the blade, V_i is the induced velocity due to the tip vortex, and V_w is the resultant velocity at the winglet.

In terms of winglet performance, it is possible that Maniaci's design is less efficient due to the toe angle selection and the wash-out effect of the positive twist angle. The positive twist angle strategy is counter to Maughmer's recommendation to establish a wash-in effect using negative twist, which was implemented on the Gertz winglet. Note in figure 6.15 that the induced velocity due to the tip vortex (V_i) acts to increase the angle of attack on the winglet. The strength of the tip vortex is proportional to C_L^2/AR of the blade [10], and the angle of attack on the winglet increases with vortex strength. In addition, the vortex's influence decreases with distance from the core (ie from the winglet root) according to the Biot-Savart law [10], thus V_i will be reduced towards the tip of the winglet. This explains the recommendation by Maughmer to

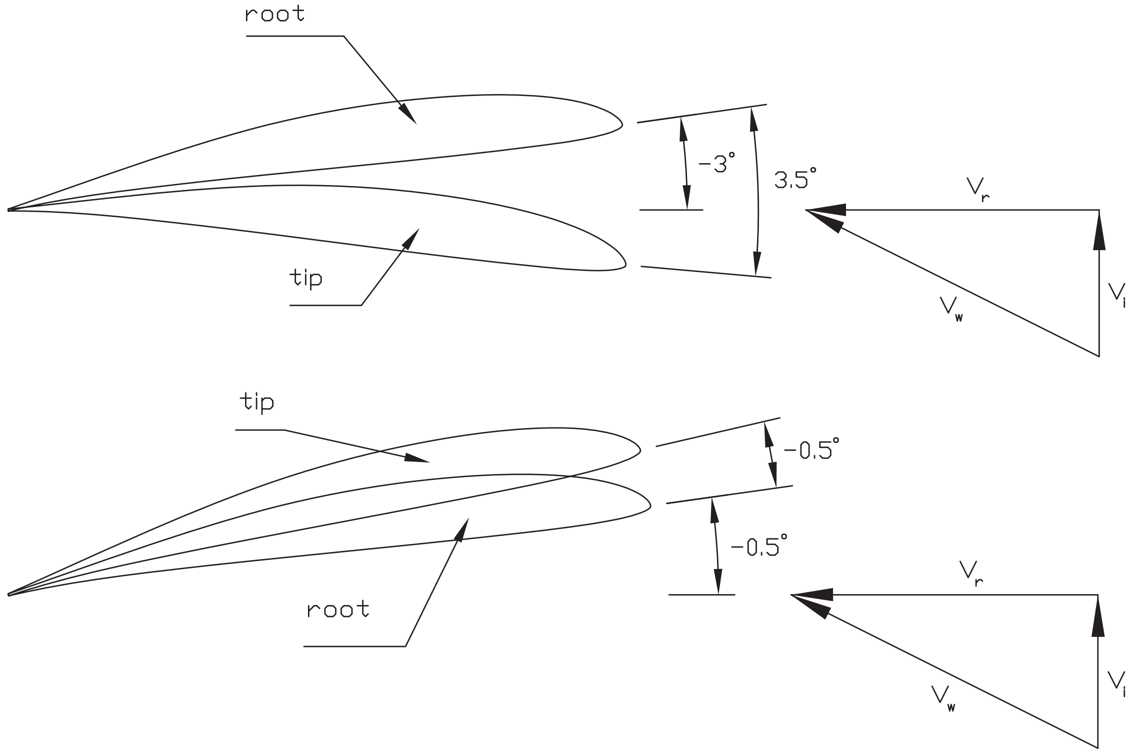

Figure 6.15: Illustration of differing winglet twist strategies. Top - Maniaci; Bottom - Gertz.

wash-in the tip. Introducing a negative twist such that the angle of attack is increased counters the reduced influence of the tip vortex and maintains a more constant angle of attack distribution along the entire winglet. This strategy was implemented on the Gertz winglet using a twist angle of $-0.5°$. The Maniaci winglet, meanwhile, introduced a positive twist of $3.5°$ thus decreasing the angle of attack in addition to the effect of the reduced V_i.

The toe angle of the winglet root is also of great importance. This is apparent upon investigation of the toe angles of the two winglets and the drag polar of the winglet airfoil, presented in figure 2.25. The Gertz and Maniaci winglets have toe angles of $-0.5°$ and $-3°$, respectively. For the idealized case of no tip vortex (i.e. $V_i = 0$ in figure 6.15), the root of the Gertz and Maniaci winglets would be operating at angles of attack of $0.5°$ and $3°$, respectively. Introducing a tip vortex will act solely to increase the angle of attack from those values. Thus, inspecting the drag polar, the

Gertz winglet begins at the low end of the low drag region and moves upwards as the tip vortex strength increases. The Maniaci winglet, meanwhile, begins more than half way up the low drag region. The advantage of this is the increased lift coefficient which will increase the positive effect of the winglet on the blade. The drawback, however, is it has less distance to travel before entering the region of rapid drag increase. It would clearly also stall prior to the Gertz design. This indicates that the Gertz design is essentially more forgiving in terms of vortex strength estimates. It is perhaps possible, therefore, that the tip vortex strength was under predicted by Maniaci's code, resulting in too great a root toe angle. Thus, the blade setting distribution of the Gertz design could be more compatible with the range of vortex strengths produced during turbine operation. As a result, the Gertz design has favourable lift and drag coefficients along the span of the winglet for a greater portion of the operating range of the rotor.

Other possible minor contributions to the improved performance of the Gertz winglet are the planform shape and winglet root chord ratio selection. The elliptical planform provides a more efficient lifting surface as compared to the linear taper used on the Maniaci design. The winglet root chord is equal to the blade tip chord as compared to Maniaci's reduced root chord. The combination of these two features maintains greater chord lengths over a greater span and results in increased Reynolds numbers and hence decreased drag coefficients along the span of the winglet.

Chapter 7

Conclusions

The objectives of this project were to design an aerodynamically efficient three-bladed wind turbine rotor customized for the UW Wind Energy Research Facility, build a set of three of these blades out of fibre-reinforced plastic while including an exchangeable tip mechanism, design and manufacture multiple tip designs, and perform tests at the Wind Energy Research Facility to establish the performance of the baseline rotor as well as the effect of the various tip designs. All of the objectives were successfully completed and the methods and results have been presented in the previous chapters. This chapter will outline the important conclusions that can be drawn from the work herein and present some recommendations towards improving the facility and experimental equipment as well as further valuable research endeavours.

7.1 Blade design and fabrication

The rotor blade was designed using the PROPID aerodynamic blade design software tool. The tool uses BEM theory to generate the blade geometry required for a rotor to perform as specified. This process resulted in a custom three-bladed rotor design that is optimized for use in the UW Wind Energy Research Facility using the available nacelle and tower. Each tapered and twisted blade is 1.6 m long with a root chord of 30 cm and tip chord of 10 cm. Three of these blades were fabricated out of fibre-reinforced plastic in the lab. A 2-piece female mold was used to manually lay up the structure of each half of each blade and subsequently bond the halves together to complete the blade. A mechanism was designed and incorporated into the blades that enabled the outer 10% of each blade to be exchanged. This feature allows any blade tip design to be tested for its effect on rotor characteristics such as power, noise emission, structural loading, etc. The blades and tip exchange mechanism performed as required throughout the test campaign; as there were no incidents of tip disconnection or blade structural failure.

7.2 Rotor performance

The performance of the baseline rotor (that with standard tips) was quantified successfully. This was achieved by measuring the voltage and current at the load bank and estimating the losses through the drivetrain prior to the connection to the generator. Making use of the variable speed capability of the turbine, data was collected at tip speed ratios that spanned the operating range of a typical wind turbine. Repeatability of the results was achieved, and the error on the power and power coefficient was determined to be between ±3% and ±10%. The rotor was found to produce a rated power of 1450 W at 11 m/s and a maximum power of 2100 W at the cut out speed of 22 m/s. The maximum power coefficient was 0.42 at a tip speed ratio of 6.7. The rotor was also estimated to be capable of producing between 4585 kWh and 8184 kWh of energy per year, depending on the wind regime.

The test results were compared to BEM predictions using two different sets of airfoil data, the VTK and Aerodas models. The VTK model correctly predicted the rotor performance up to 5.5 m/s, but differed from the test results for the remaining sections of the operational envelope. This was not unexpected, as previous studies demonstrated the difficulty in predicting wind turbine performance, especially at high wind speeds. VTK model inputs, namely the parameters that defined the airfoil aerodynamic coefficients, were able to be altered such that the model could predict the rotor's performance far more accurately. At wind speeds below 15 m/s the performance was well predicted, including the peak power and wind speed. The effects of blade roughness, variable speed operation, and tip and hub loss models were also investigated. Despite such efforts, however, the rotor's maximum power was still underpredicted by up to 13% by the model.

The prediction using the Aerodas model was not as accurate as the modified VTK model, but did estimate the power correctly over the range of wind speeds between 5.5 m/s and 10 m/s. The predicted peak power of 1600 W at 11.5 m/s was slightly high but the wind speed was close to that of the experimental data. The Aerodas model predicted the power at the cut-out speed to be 1450 W as compared to the experimental result of 2100 W. The slope of the power curve at hight wind speeds, however, was roughly parallel to that of the experimental data, something that the modified VTK method could not accomplish. The minor success of the Aerodas model is encouraging considering the blade had to be modeled as having only one airfoil, the S834, due to the lack of complete data for the S833 and S835.

Some realizations were made as a result of analyzing the performance of the models. Firstly, it was concluded that 2D airfoil data should be corrected for finite blade effects as outlined in section 2.3.3.1. The corrections, however, should not be applied at angles of attack corresponding to low wind speeds, in this case wind speeds below roughly 6 m/s. Another recommendation is regarding the Viterna model, which was used in the VTK method to predict rotor performance at high wind speeds. This model was unable to predict the steep slope of the power curve at high wind speeds for any set of input parameters. This was attributed to the fact that the model assumes constant rotor power beyond stall and thus a steep incline in this region is hard to predict. It would thus be valuable if the Viterna model was altered or re-derived such that power is not assumed to be constant beyond stall.

Finally, the performance of the rotor was only able to be accurately predicted at wind speeds above 10 m/s after gathering the experimental data and adjusting most of the inputs to the VTK model such that the experiment matched the prediction. This is clearly an indication that better methods are required to model the behaviour of wind turbine rotors at moderate to high wind speeds.

7.3 Effect of blade tip design

The effects of two different winglets, the Maniaci and Gertz designs, were quantified by repeating the test that was executed with the standard tip for each winglet. Both winglets were found to have a bell-shaped power augmentation profile, with a broad peak between 6.5 m/s and 9.5 m/s where power was increased by 5% to 7%. These power augmentation figures matched closely with the findings in the literature that suggested increases of 2% to 8% are possible. The Maniaci winglet was superior at wind speeds below 5 m/s whereas the Gertz winglet was better above 5 m/s. Annual energy production figures were also estimated for each winglet. It was found that the Maniaci and Gertz winglets would improve energy capture by a maximum of 2.3% and 3%, respectively, and that they would not reduce energy capture for any defined wind regime. A 3% increase would represent a net present value of between $224 and $374 to the turbine owner, and considering the total installed cost of such a turbine is in the range of $12000 it is uncertain whether it would be worth the effort to include such winglet designs on a turbine this size. It was noted, however, that these designs are certainly not optimal and it is possible that if a concerted effort were made to optimize the winglet design through further modeling and testing, more significant performance improvements could be attained.

Winglets were also found to decrease the maximum power by 8%, which it was speculated could be advantageous. It would allow the entire power curve to be shifted up while not increasing the maximum rotor power beyond the rated power of the generator. An analysis revealed that this could result in an additional yearly energy capture of 10%. Such an improvement would yield a net present value of between \$748 and \$1246 for this turbine, which is very significant considering the total installed cost estimate mentioned above. The 8% maximum power reduction, however, could also be an artifact of the variable speed nature of the test plan. This finding would have to be explored further before full confidence could be established.

7.4 Equipment improvements

Several deficiencies in both the test facility, turbine rig, and instrumentation and data collection were discovered throughout the experimentation process. Many of these drawbacks, however, can be solved simply and readily if so desired.

7.4.1 Facility

The UW Wind Energy Research facility is a multi-purpose facility designed to house both wind energy and fire research studies. It is clear when attempting to execute wind turbine performance tests that the facility was not solely designed for such purposes, as there are many obvious changes to the facility that could improve the quality and efficiency of such tests. Firstly, the cross-section of the air jet through the test section is actually wider and shorter than the exit at the end. This results in significant recirculation on either side of the jet, not to mention wasted energy. This design flaw was documented in detail in McWilliam [45] including recommendations towards possible solutions. One simple solution is to nozzle the jet down to the width of the test section exit which would also increase the flow speed and decrease turbulence.

The test results also indicate that the flow is deflected away from the streamwise axis by 2° in each cross-stream axis. This is no doubt due to the presence of the large burn house that sits roughly 3.5 m beyond the test section exit and blocks the entire air jet. If this structure were simply relocated the flow deflection would most likely disappear and significant flow energy would be saved, perhaps increasing the maximum wind speed of the facility.

The turbulence at the rotor plane was also found to be roughly 6%. While some flow conditioning does exist, it is clearly not optimal. If it is desired to compare experimental results from the facility to predictions produced by an idealized model, the turbulence should be reduced. In addition there are is a pair of semicircular baffles attached to the exit of each of the six fans in the fan bank which add significant turbulence and unnecessary drag to the flow. A study by Gertz in 2009 [73] indicated that if these baffles were simply lined up with the flow, both the turbulence and maximum wind speed could be increased significantly.

A reliable map of the flow through the facility is also required, as those attempted previously are incomplete and inconsistent. Should any of the above improvements be implemented, a full flow mapping campaign would be required.

7.4.2 Wind turbine rig, instrumentation and data collection

Preliminary tests found several areas for improvement in the design and operation of the turbine rig. Firstly, the method required to determine the power production of the rotor is inexact and tedious. Currently, power is measured at the load and must be summed with an estimate of the losses accrued between the rotor and the load bank. A method is required to measure the power produced at the rotor more readily and accurately. One that has been proposed is to turn the low-speed shaft of the turbine into a torque transducer. This would simply require the installation of strain gauges and a signal conditioning and transmission system. The Wind Energy Research group has already looked into the requirements for such a system and it is highly recommended that one be implemented before any further performance testing is executed.

The sampling rate of the data collection is also too slow. Currently the Keithley 2700 is used to gather several measurements. It is incapable of simultaneous measurements, however, and the switching time between channels is very slow. A full data point takes 3 seconds to collect. If the sampling rate could be increased to a reasonable frequency, the uncertainty in the results would be significantly reduced.

Finally, the arrangement of the load bank and rotor speed control can be significantly improved. As it stands, the load bank is static at a load of roughly 3 kW, while the turbine obviously produces a variable load depending on the wind and rotor speed. This arrangment requires grid power to be fed into the load bank to cover the additional load not provided by the rotor, which allows the load bank to act as though it is variable to accomodate the turbine while actually wasting power unnecesarrily. In addition, the speed of the rotor is determined manually within the control room. At low shaft speeds the voltage across the generator and load bank is used to control the rotor speed. Once full voltage is reached, the field in the generator is weakened to allow more current to flow through it, which could result in generator damage if the current reaches too high a level. It is recommended to assemble a controller/load bank combination that would solve both of these problems.

7.5 Recommendations for future studies

Considering the relative success of this initial winglet performance evaluation program, there are numerous possibilities for further research. The winglet idea could be further refined through continued collaboration with Maniaci and Maughmer at Pennsylvania State University. In addition, any other idea for specialized tip geometry could be tested now that a proven evaluation testbed is available. Further studies could also be performed using the existing winglets. A flow visualization study using smoke or tufts on the winglets would provide further insight into how and when the winglets are stalling, and would be valuable for future winglet design efforts. The effect of the existing winglets on noise production could also be verified. The literature indicates that winglets are capable of reducing tip noise thus a study that investigated such effects would be valuable. Blade loading is known to be increased by winglets as a result of the increased power production. It would certainly be worthwhile to investigate that issue as well.

It would also be very useful to generate 2D wind tunnel data for all three S83X series airfoils that spans a wide range of angles of attack. This would allow other models to be used to predict the performance of the rotor providing valuable validation data. Finally, the velocity correlation study could be repeated using two anemometers simultaneously. One would be located at the test section entrance and one at the rotor plane. Gathering simulataneous velocity data would produce a correlation with more confidence than the one presented in this study.

Bibliography

[1] M.O.L. Hansen. *Aerodynamics of Wind Turbines.* Earthscan. Sterling, VA, 2008. 1, 7, 8, 9, 11, 16, 17, 18

[2] T. Burton, D. Sharpe, N. Jenkins, and E. Bossanyi. *Wind Energy Handbook.* John Wiley and Sons: New York, 2001. 1, 12, 13, 14, 15, 18, 29, 30, 46, 57, 98, 105, 106

[3] World Wind Energy Association. 16 Gigawatt added in First Half of 2010, October 2010. http://www.wwindea.org. 3

[4] I. Antoniou, H. Aagaard Madsen, and U. Schmidt Paulsen. A theoretical and experimental investigation of new tip shapes. In *Proceedings of the European Community Wind Energy Conference, Germany, Mar. 8-12*, 1993. 4

[5] J.J. Chattot. Effects of blade tip modifications on wind turbine performance using vortex model. *Computers and Fluids*, 38:1405–1410, 2009. 4, 43, 44

[6] Y. Shimizu, E. Ismali, Y. Kamada, and T. Maeda. Power Augmentation of a HAWT by Mie-type Tip Vanes, considering Wind Tunnel Flow Visualization, Blade-Aspect Ratios and Reynolds Number. *Wind Engineering*, 27(3):183–194, 2003. 4, 42, 45, 57, 112

[7] M. Gaunaa and J. Johansen. Determination of the maximum aerodynamic efficiency of wind turbine rotors with winglets. *Journal of Physics: Conference Series*, 75, 2007. 4, 43, 44

[8] J. Johansen, M. Gaunaa, and N.N. Sorensen. Increased aerodynamic efficiency on wind turbine rotors using winglets. Number 2008-6728 in 26th AIAA Applied Aerodynamics Conference. Honolulu, Hawaii. American Institute of Aeronautics and Astronautics, August 2008. 4, 43, 44

[9] UIUC Applied Aerodynamics Group. UIUC Airfoil Data Site, October 2009. http://www.ae.illinois.edu/m-selig/ads.html. 9, 50, 51, 52

[10] J.D. Anderson. *Fundamentals of Aerodynamics*. McGraw-Hill, 3rd edition, 2001. 9, 10, 11, 114

[11] A. Betz. Schraubenpropeller mit geringstem energieverlust. Technical report, Gottinger Nachr., Germany, 1919. 13

[12] D.A. Spera. *Wind Turbine Technology*. ASME Press, 1994. 18

[13] UIUC Applied Aerodynamics Group. PROPID, September 2009. http://www.ae.illinois.edu/m-selig/propid. 19, 20, 55

[14] M.S. Selig and J.L. Tangler. Development and application of a multipoint inverse design method for horizontal axis wind turbines. *Wind Engineering*, 19(2):91–105, 1995. 19, 56

[15] R.E. Wilson and S.N. Walker. A fortran program for the determination of performance, load and stability derivatives of windmills. Technical Report GI-41840, Dept. of Mechanical Engineering. Oregon State University. Corvallis, Oregon. National Science Foundation. Research Applied to National Needs (RANN), Oct. 1974. 19

[16] B. Hibbs and R.L. Radkey. Calculating rotor performance with the revised 'prop' computer code. Technical Report RFP-3508. UC-60., Horizontal-Axis Wind System Rotor Performance Model Comparison - A Compendium. Wind Energy Research Center. Rockwell International., 1983. 19

[17] J. Tangler. Horizontal-Axis Wind Turbine Performance Prediction Code PROPSH. Technical report, Rocky Flats Wind Energy Research Center. Golden. CO., 1983. 19

[18] J. Tangler. HAWT Performance Prediction Code for Personal Computers. Technical report, Solar Energy Research Institute. Golden. CO., January 1987. 19

[19] M. Buhl. NWTC Design Codes (WTPerf by Marshall Buhl), January 2011. http://wind.nrel.gov/designcodes/simulators/wtperf. 21

[20] L.A. Viterna and R.D. Corrigan. Fixed pitch rotor performance of large horizontal axis wind turbines. Technical Report N83 19233, NASA Lewis Research Center, 1981. 22, 50, 100, 102, 104

[21] J. Tangler and J.D. Kocurek. Wind turbine post-stall airfoil performance characteristics guidelines for blade-element momentum methods. In *43rd AIAA Aerospace Sciences Meeting and Exhibit, January 10-13, 2005. Reno, Nevada, USA*, 2005. 23, 24, 50, 52, 55, 100, 101, 102, 103, 104

[22] M. Hand. NREL 10-m Wind Turbine in NASA Ames 80'x120' Wind Tunnel. internet, 2001. wind.nrel.gov/amestest. 23, 30

[23] D.A. Spera. Models of lift and drag coefficients of stalled and unstalled airfoils in wind turbines and wind tunnels. Technical Report NASA/CR2008-215434, National Aeronautics and Space Administration, 2008. 25

[24] H. Snel, R. Houwink, G.J.W. van Bussel, and A. Bruining. Sectional prediction of 3D effects for stalled flow on rotating blades and comparison with measurements. In *European Community Wind Energy Conference. Lübeck-Travemünde, Germany*, pages 395–399, March 1993. 28

[25] P.K. Chaviaropoulos and M.O.L. Hansen. Investigating three-dimensional and rotational effects on wind turbine blades by means of a quasi-3D Navier-Stokes solver. *Journal of Fluids Engineering*, 122:330–336, 2000. 28

[26] N.V. Raj. An improved semi-empirical model for 3-d post-stall effects in horizontal axis wind turbines. Master's thesis, University of Illinois, Urbana-Champaign, 2000. 28

[27] C. Bak, J. Johansen, and P.B. Andersen. Three-dimensional corrections of airfoil characteristics based on pressure distributions. In *2006 European Wind Energy Conference. Athens, Greece*, 27 February - 2 March 2006. 28

[28] C. Lindenburg. Investigation into rotor blade aerodynamics. Technical Report ECN-C03-025, ECN, 2003. 28

[29] J.J. Corrigan and J.J. Schillings. Empirical model for stall delay due to rotation. In *American Helicopter Society Aeromechanics Specialists Conference. San Fransisco, California*, January 1994. 28

[30] D. Simms, S. Schreck, M. Hand, and L.J. Fingersh. NREL Unsteady Aerodynamics Experiment in the NASA-Ames Wind Tunnel: A Comparison of Predictions to Measurements. Technical Report NREL/TP-500-29494, National Renewable Energy Laboratory, 2001. 29, 30, 31, 33, 34

[31] M.M. Hand, D.A. Simms, L.J. Fingersh, D.W. Jager, and J.R. Cotrell. Unsteady Aerodynamics Experiment Phase V: Test Configuration and Available Data Campaigns. Technical Report NREL/ TP-500-29491, National Renewable Energy Laboratory, 2001. 31

[32] S. Schreck, T. Sant, and D. Micallef. Rotational Augmentation Disparities in the MEXICO and UAE Phase VI Experiments. Technical Report NREL/CP-500-47759, National Renewable Energy Laboratory, 2010. 32, 35, 36

[33] J.G. Schepers and H. Snel. Model experiments in controlled conditions final report. Technical Report ECN-E–07-042, Energy Research Center of the Netherlands, 2007. 32

[34] D. Micallef, M. Kloosterman, C. Ferreira, T. Sant, and G. van Bussel. Comparison and Validation of BEM and Free Wake Unsteady Panel Model with the MEXICO Rotor Experiment. In *Extended Abstracts for Euromech Colloquium 508*, Wind Turbine Wakes. European Mechanics Society, October 2009. 37

[35] R.T. Whitcomb. A design approach and selected wind-tunnel results at high subsonic speeds for wing-tip mounted winglets. Technical Report NASA TN D-8260, National Aeronautics and Space Administration, July 1976. 37

[36] M.D. Maughmer. The design of winglets for high-performance sailplanes. In *AIAA Paper 2001-2406, June*, 2001. 38, 39, 41, 57, 62, 109

[37] M.D. Maughmer, T.S. Swan, and S.M. Willits. The design and testing of a winglet airfoil for low-speed aircraft. Technical report, The Pennsylvania State University, 2001. 41, 61

[38] H. Imamura, Y. Hasegawa, and K. Kikuyama. Numerical analysis of the horizontal axis wind turbine with winglets. *Japan Society of Mechanical Engineering International Journal*, 41:170 – 176, 1998. 43, 44

[39] J. Johansen and N. N. Sorensen. Aerodynamic investigation of Winglets on Wind Turbine Blades using CFD. Technical Report Riso-R-1543(EN), Riso National Laboratory, 2006. 43, 44

[40] M. Dossing. Vortex lattice modeling of winglet on wind turbine blades. Technical Report Riso-R-1621(EN), Riso National Laboratory, 2007. 43, 44

[41] J. Johansen and N.N. Sorensen. Numerical Analysis of Winglets on Wind Turbine Blades using CFD. Technical report, Riso National Laboratory, 2007. 43, 44

[42] S. Hjort, J. Laursen, and P. B. Enevoldsen. Aerodynamic winglet optimization. Technical report, Siemens Wind Power A/S, 2008. 43, 44

[43] T. van Holten. Concentrator systems for wind energy, with emphasis on tipvanes. *Wind Engineering*, 5:29–45, 1981. 42

[44] OPA Feed-in Tariff Program: Quick Facts Table, March 2011. http://fit.powerauthority.on.ca. 47

[45] M.K. McWilliam. Development of a wind tunnel test apparatus for horizontal axis wind turbine rotor testing. Master's thesis, University of Waterloo, Waterloo, ON, 2008. 48, 75, 78, 120

[46] D.M. Somers. The S833, S834, and S835 Airfoils. Technical Report NREL/SR-500-36340, National Renewable Energy Laboratory, August 2005. 49, 50, 85, 99

[47] R. Eppler. *Airfoil Design and Data*. Springer-Verlag, Berlin, 1990. 50

[48] R. Eppler. *Airfoil Program System "PROFILOO."*, 2001. 50

[49] D. M. Somers. Design and Experimental Results for the S825 Airfoil. Technical report, Airfoils, Inc., 1999. Proprietary to NREL. 50

[50] D.M. Somers. Design and Experimental Results for the S805 Airfoil. Technical Report ISR-440-69, NREL, Jan. 1997. 50

[51] D.M. Somers. Design and Experimental Results for the S809 Airfoil. Technical Report ISR-440-6918, NREL, Jan. 1997. 50, 51, 52

[52] D.M. Somers. Design and Experimental Results for the S814 Airfoil. Technical Report ISR-440-69, NREL, Jan. 1997. 50

[53] D.M. Somers. Design and Experimental Results for the S827 Airfoil. Technical report, Airfoils, Inc., 1999. Proprietary to NREL. 50

[54] D.M. Somers. *Subsonic Natural-Laminar-Flow Airfoils. Natural Laminar Flow and Laminar Flow Control*. Springer-Verlag New York, Inc., 1992. 50

[55] C. Hansen. NWTC Design Codes (AirfoilPrep). internet, March 2010. http://wind.nrel.gov/designcodes/preprocessors/airfoilprep/. 53

[56] P.J. Moriarty and A.C. Hansen. Aerodyn theory manual. Technical Report NREL/EL-500-36881, National Renewable Energy Laboratory, December 2005. 53

[57] D. Maniaci. Maniaci winglet design. Design document of Maniaci winglet provided to Drew Gertz, July 2010. 61, 106, 107, 108

[58] M. D. Maughmer. Personal correspondence over telephone, April 2010. 62

[59] D. Maniaci. Email correspondence, August 2010. 62

[60] das-holzportal.com, April 2011. http://www.das-holzportal.com/. 68

[61] Composotech structures - innovative excellence, http://www.composotech.com/. 68

[62] B. Gaunt. Power generation and blade flow measurements of a full scale wind turbine. Master's thesis, University of Waterloo, Waterloo, ON, 2009. 69, 74, 75, 76, 80, 81, 84

[63] C. Best. Measurement of fuel regression rate of a pool fire in crosswind with and without a large downwind blocking object. Master's thesis, University of Waterloo, 2010. 74, 75, 77, 81, 82, 89

[64] C. Devaud, J. Weisinger, D. Johnson, and E. Weckman. Experimental and numerical characterization of the flowfield in the large-scale UW live fire research facility. *Int. J. Numer. Meth. Fluids*, 60:539–564, 2009. 75

[65] S. Orlando, A. Bale, and D. Johnson. Experimental study of the effect of tower shadow on anemometer readings. *Journal of Wind Engineering and Industrial Aerodynamics*, 99:1–6, 2011. 82

[66] U. Frisch. *Turbulence*. Cambridge University Press, 1995. 83

[67] National Instruments Corporation. NI LabVIEW - Improving the Productivity of Engineers and Scientists, http://www.ni.com/labview/. 84

[68] Keithley Instruments, Inc. *Model 2700 Multimeter/Switch System User's Manual*, 2001. 84, 169

[69] J. Weisinger. Characterization of the university of waterloo live fire research facility wind generation system. Master's thesis, University of Waterloo, Waterloo, Canada, 2004. 89

[70] F. Seglenieks. Current readings for uw weather station, 2010. http://weather.uwaterloo.ca/. 93, 171

[71] S.F. Hoerner. *Fluid-Dynamic Drag*. Hoerner Fluid Dynamics, 1965. 104

[72] Small wind turbine purchasing guide, March 2011. Canadian Wind Energy Association. 112

[73] D. Gertz. An experimental study of the difference in wind tunnel flow quality by changing fan baffle alignment. April 2009. 121

[74] H.W. Coleman and W.G. Steele. *Experimentation and uncertainty analysis for engineers*. John Wiley & Sons, Inc., 2nd edition, 1999. 168

[75] Campbell Scientific, Inc. *CSAT3 Three Dimensional Sonic Anemometer*, revision: 6/10 edition. 169

APPENDICES

Appendix A

Blade Fabrication

A.1 Mold preparation

To build the blades out of fibreglass a two-piece female mold was prepared. First, solid models of the mold halves were created using the SolidWorks solid modeling program. See figure A.1 for the solid model of the suction side mold.

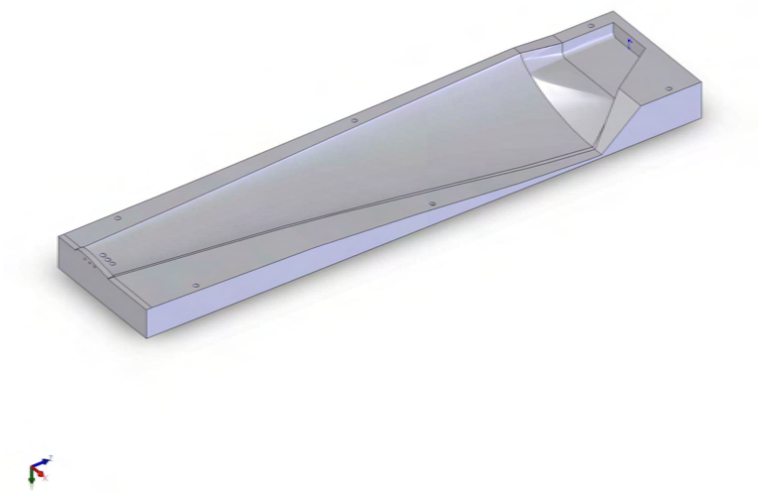

Figure A.1: Solid model of low-pressure side mold.

Holes were placed in the molds for alignment dowels that would guarantee the alignment of the coupler block during fabrication as well as allow the mold halves to line up perfectly during the mating and bonding phase. To locate the coupler within the part, holes were drilled horizontally in the side of the low-pressure side of the mold such that locating pins could align the coupler into place during the bonding phase. Vertical dowels were also used to locate the coupler as well as to create holes in the blade to place and access the cams. The vertical alignment dowels were prepared out of half inch solid aluminum stock while the 5 mm cam lock pins doubled as horizontal dowels for the coupler block. Figure A.2 shows the method by which the coupler block was located within the part during fabrication.

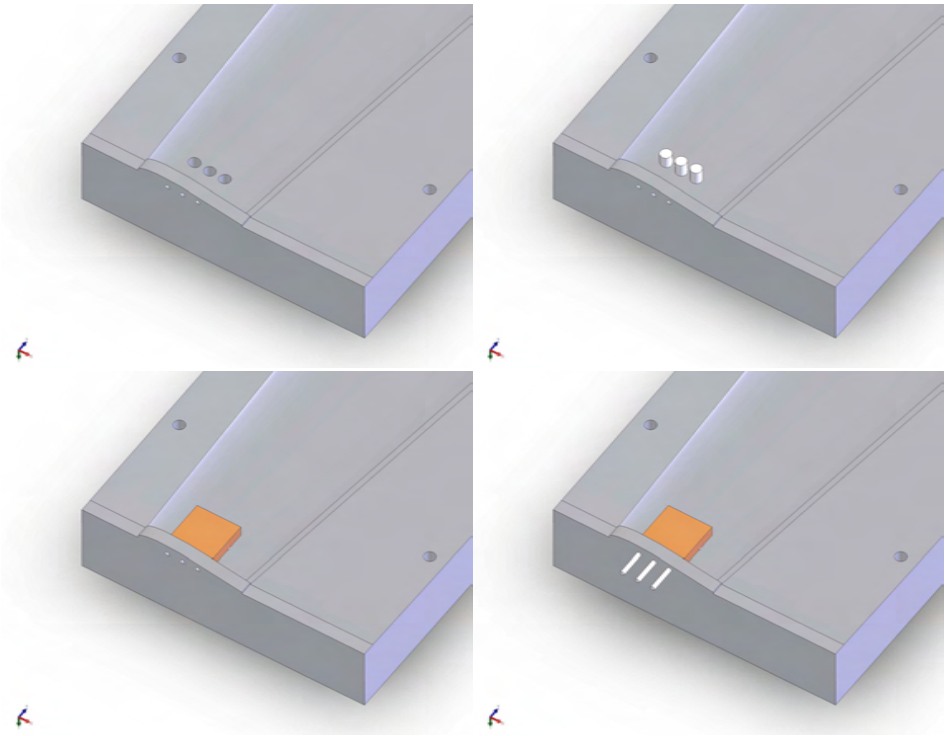

Figure A.2: Coupler placement procedure. Top left: empty mold; top right: coupler alignment dowels inserted; bottom left: coupler block placed on alignment dowels; bottom right: alignment bolts inserted.

The mating surfaces of the molds were also offset to account for application of the mold finish and to allow space for the skin and bonding layers to sandwich between the molds during bonding without altering the shape of the blade. This is the technique typically used in blade manufacture and results in a trailing edge thickness of roughly

3 mm. See figure A.3 for a diagram of these mold provisions.

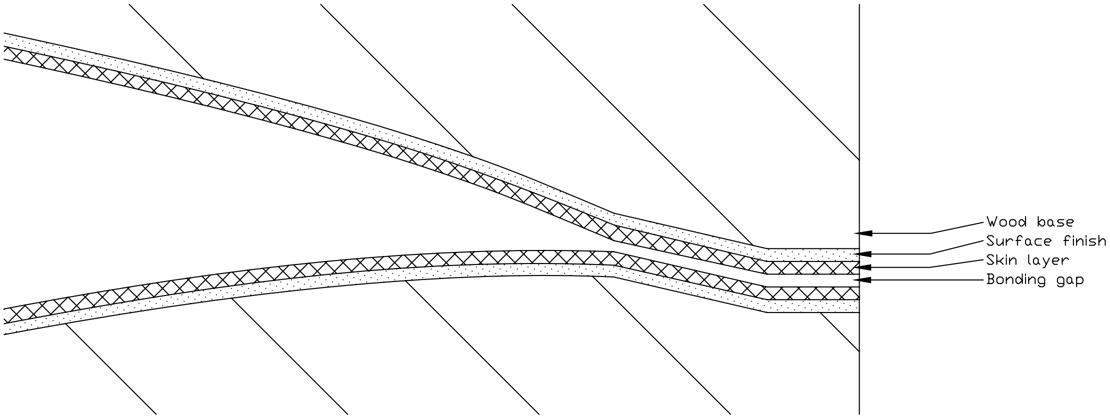

Figure A.3: Trailing edge detail of mold provisions.

Using the SolidWorks mold file a MasterCAM milling program was prepared by technician Jason Benninger and the in-house OKK 3-axis CNC machine was used to mill the female molds out of built up dies of Baltic birch plywood. Ideally aluminum would have been used due to its capability for excellent surface quality, however the cost would have been unreasonable due to the large size of the mold dies. Figure A.4 shows a picture of a mold during milling, while figure A.5 shows the mold after it was finished milling.

The molds were finished using Duratec as a surface finishing product. This would allow the parts to release from the wood mold once finished. To ensure the Duratec would bond to the wood molds, fibreglass resin with a 1.0% (by mass) DDM9 catalyst was first applied. Once it was tacky, the first of three coats of Duratec with 1.5% DDM9 catalyst was then rolled onto the molds, again having waited until one coat was tacky before applying the next. The molds were hand sanded with 180, 350, and 520 grit sandaper in that order. Six coats of TR 104 high temperature mold release wax were then applied. This procedure further ensures that the part will release easily from the mold. At this point the molds had a slight shine and were ready for part fabrication. See figure A.6 for a picture of the finished suction side mold. The alignment dowels were also inserted to display their use.

Figure A.4: Milling the mold.

Figure A.5: Mold upon completion of milling.

Figure A.6: Finished suction side mold with alignment dowels inserted.

A.2 Gel coat and fibre lay-up

Prior to fabricating each part, the molds were waxed another two times with the mold release wax. The alignment dowels and pins were also waxed to ensure they did not bond to the mold or part. Half inch bolts were used to plug the coupler block dowel holes during applications of the gel coat and resin. Once the application was finished the bolts were removed creating cam access holes in the blade surface. Three layers of masking tape were also applied to the mold where the face of the coupler would eventually be contacted. One layer of this tape was removed after application of each of the gel coat, skin resin, and structural resin. This kept the location clean such that the coupler block could be placed during bonding without interference. With the molds prepared, the outer surface of the blade, called the gel coat, was applied. This is a polyester-based compound with 1.5% DDM9 catalyst. DDM9 catalyst enables a fast cure so that releasing agents do not leech into the blade. Figure A.7 shows the tip of the low-pressure mold after gel coat application, figure A.8 shows the same area after removing the bolts and tape, and figure A.9 shows the entire mold with the gel coat applied.

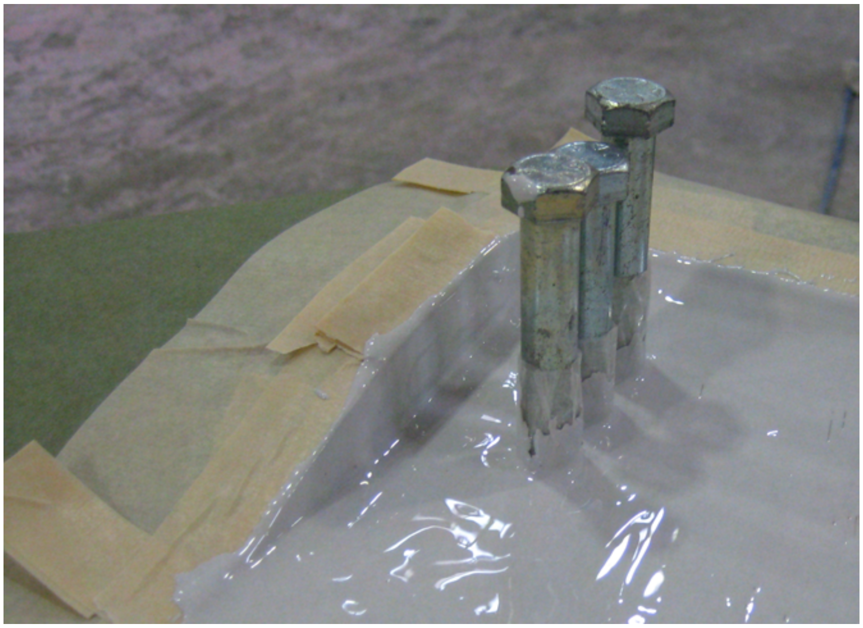

Figure A.7: Gel coat applied - prior to bolt and tape removal.

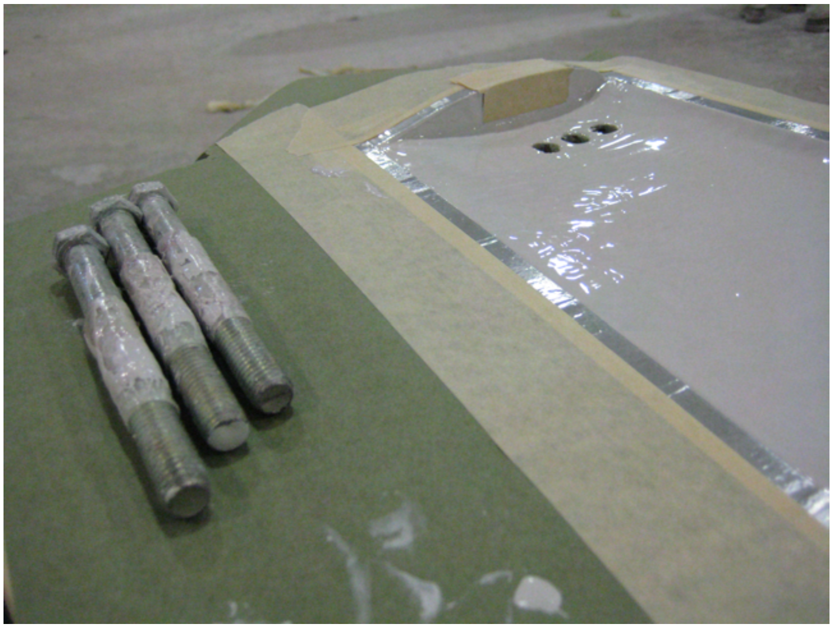

Figure A.8: Gel coat applied - bolts and tape removed.

Figure A.9: Gel coat applied to entire mold.

Once the gel coat is tacky, iso-polyester bonding putty with 1.5% 50-50 catalyst (50% norox 925 and 50% luperox CU80) was applied to the sharp corners of the mold. The 50-50 catalyst is used when a slower cure is desired. Applying bonding putty to the sharp edges fills in the areas that the first layer of fibre cannot reach due to the sharp bending radius requried.

Next, the first of seven layers of fibre cloth was laid up in the mold. See table A.1 for details of the fibre lay-up schedule of each shell, starting at the outer-most layer called the skin. Note that the lengths of the bi-directional and uni-directional layers taper down. This is because blade loading reduces from root to tip and thus less structure is required towards the tip.

The CSM skin was laid onto the gel coat first. Slits were cut at various locations to allow the fibre to sit properly in the mold. Iso-polyester resin with 1.5% DDM9 catalyst was then applied to the cloth with a foam roller. The fibre was then rolled out with a bristle brush, which eliminates any air bubbles between the gel coat and skin. Figure A.10 shows the molds with the skin and resin applied. Note that the skin stretches beyond the edges of the mold cavity, consistent with the sandwiching technique discussed earlier. See figure A.11 for a close-up view of the edges with the bonding putty present behind the skin.

Fibre layer	Coverage
Chopped strand mat (CSM)	all
Bi-directional at +/- 45^o (BD45)	0 - 0.9R, full surface
BD45	0 - 0.7R, full surface
Uni-directional, axial (UDA)	0 - 0.8R, along spar
UDA	0 - 0.6R, along spar
UDA	0 - 0.4R, along spar
BD45	0 - 0.5R, full surface

Table A.1: Lay-up schedule of blade.

Figure A.10: Mold with skin layer applied.

The next six layers of fibre are the structural bi-directional (BD) and uni-directional (UD) cloth. The BD cloth has fibres oriented at +/- 45^o and is used to strengthen against torsion. The UD layers are placed along the quarter chord and aid along with

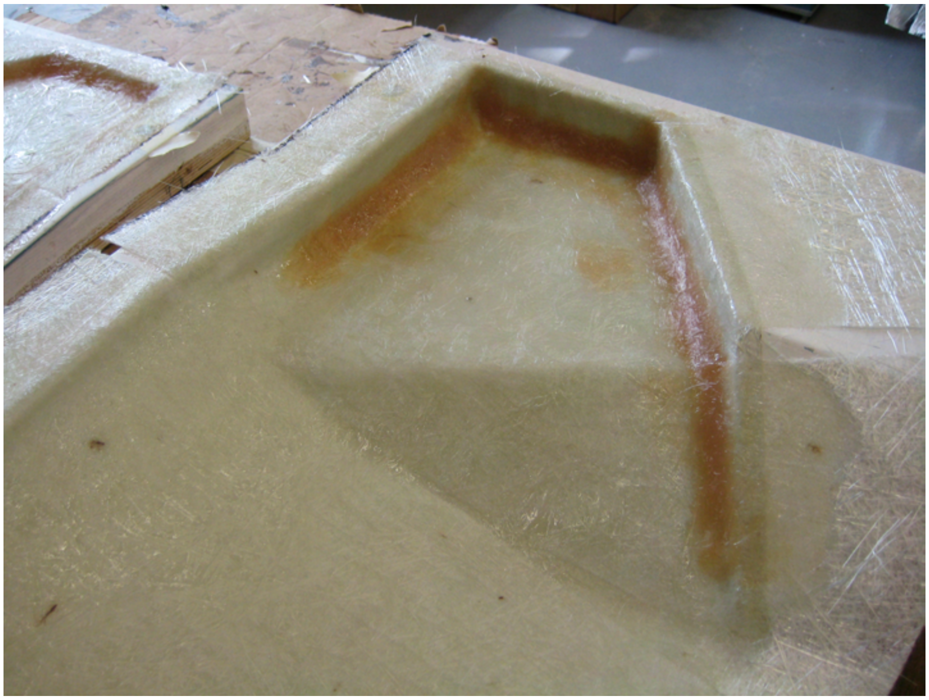

Figure A.11: Mold with skin applied - edge detail.

the spar to resist bending loads due to rotor thrust. Two layers of BD were applied, followed by all three layers of UD, followed by the last layer of BD. After each layer was applied, slits were cut in the cloth, iso-polyester resin with 1.5% 50-50 catalyst was rolled on with a foam roller and the fibre was rolled out with a bristle brush, as was done on the skin. At this point a layer of peel-ply cloth was applied to the entire mold cavity. The peel-ply cures with the fibre layers and is then peeled off leaving a rough texture which ensures a strong bond between the two blade halves after bonding is complete. The same procedure of slitting, rolling on resin with 1.5% 50-50 catalyst and rolling out air bubbles is performed after laying the peel-ply. Figure A.12 shows the part at this point.

The next step is known as “green trimming.” In this process all of the fibre other than the skin that extends beyond the mold cavity is trimmed away. During bonding this allows for the mold to close as it was designed to. A close-up of this extra fibre can be seen in figure A.13. When the structural layers are semi-cured (roughly 2 hours after catalyst is added to resin), a utility knife is sliced along the mold cavity through the extra fibre, which at this point is hard enough to slice but not rock solid as it would be when fully cured. See figure A.14 and figure A.15 for pictures of this process. Figure A.16 shows the molds after green trimming was complete.

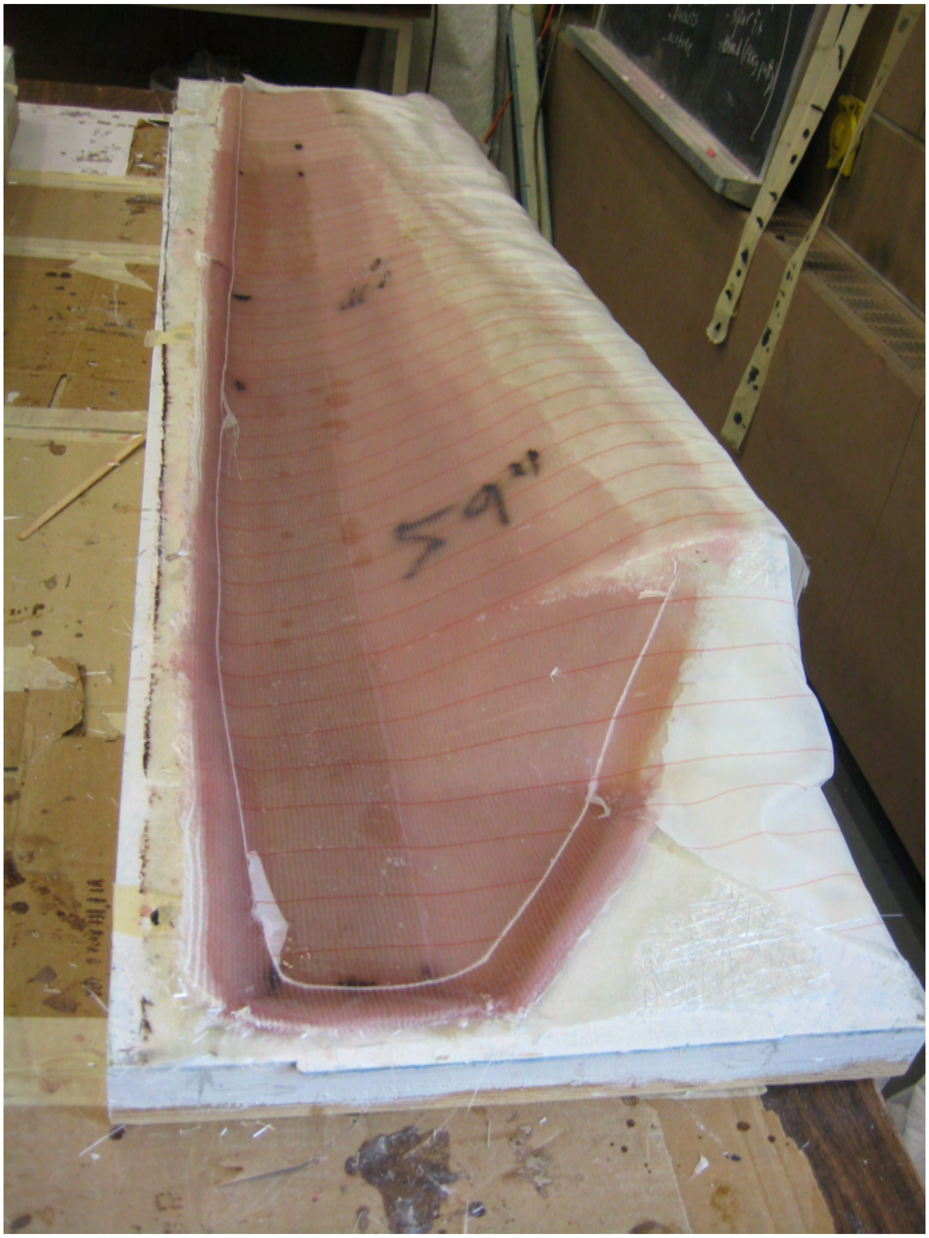

Figure A.12: Mold with structural layers and peel-ply.

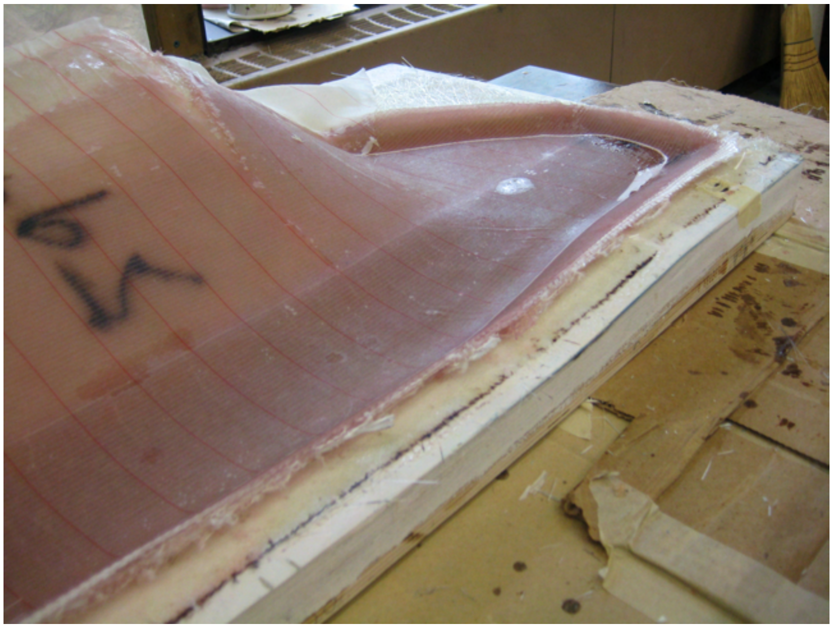

Figure A.13: Fibre to be removed during “green trimming.”

Figure A.14: Green trimming.

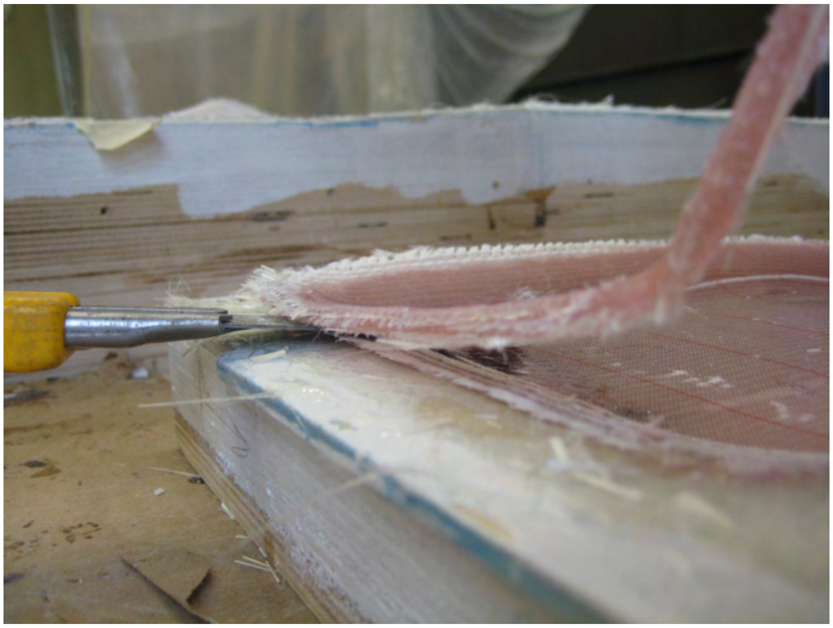

Figure A.15: Green trimming - detail.

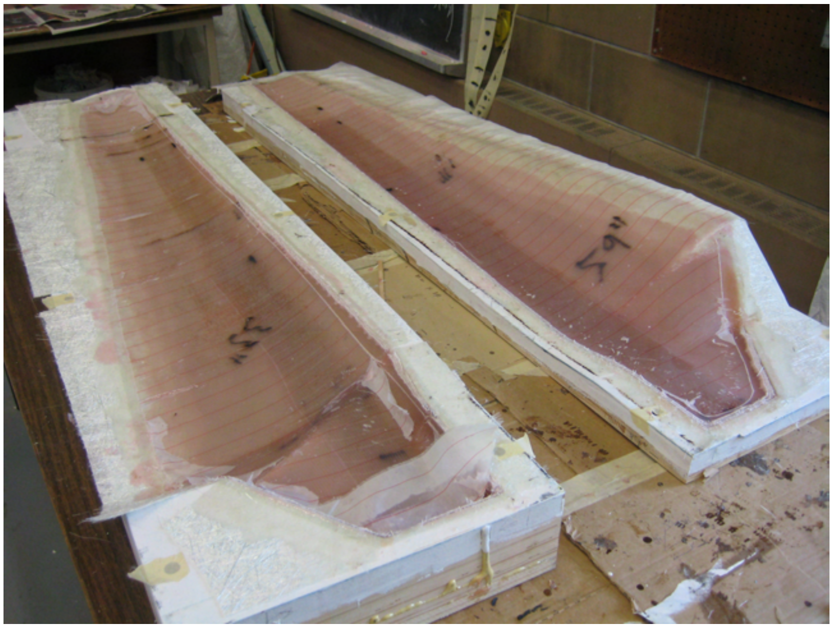

Figure A.16: After green trimming.

A.3 Spar preparation

A fibre-wrapped foam spar was installed in the blades to resist against thrust loading. To build the spar, a piece of solid blue foam measuring 1145 mm x 80 mm x 20 mm was cut and its edges sanded to achive rounded edges with a roughly 10 mm radius of curvature. The foam core was then wrapped with a piece of satin fibre cloth that had been pre-wetted with resin and 1.5% 50-50 catalyst such that the entire core had at least one layer of fibre wrapped around it. Bonding putty with 1.5% 50-50 catalyst was also applied along the fibre seam to help it stick. Finally, the spar was wrapped tightly in wetted peel-ply which kept the fibre pressed tightly against the foam core during curing. Once cured, the peel ply was removed and the required profile of the spar drawn on. It is required to cut the spar such that it follows the inner dimensions of the blade. See figure A.17 for a picture of the spar at this point. Figure A.18 shows the spar after it has been cut to size.

A.4 Mold fitting

Once the spar was cut a technique known as the “plasticine test” was used to ensure that the mold could close properly allowing for a 1 mm bonding gap above and below the spar, coupler block, and root block inserts. The root block is a block of wood that is placed in the root of the blade through which the mounting bolts are passed. The plasticine test entails putting the coupler block, spar, and root block into the mold and placing small cones of plasticine separated by roughly 50 mm on top of them. See figure A.19 for a photo of the cones in place. The mold is then closed tightly and re-opened. The thickness of the cones tells the size of the gap between the insert and the inner surface of the blade. See figure A.20 for a photo of the cones at this point. The inserts are then trimmed and the procedure repeated until the gap everywhere is roughly 2 mm to allow for 1 mm of bonding putty between the inner surface of the blade and each bonding surface of the insert inside.

A.5 Bonding

This is the stage where the low- and high-pressure sides of the part are bonded together. First, the vertical alignment dowels are put in place in the low-pressure mold. Next, a mixture of bonding putty and 1.5% 50-50 catalyst is prepared. The putty is applied generously along the seams of each mold half and on both halves where the root block, spar, and coupler will be contacted.

Figure A.17: Spar prior to cutting.

Figure A.18: Spar cut to inner dimensions of blade.

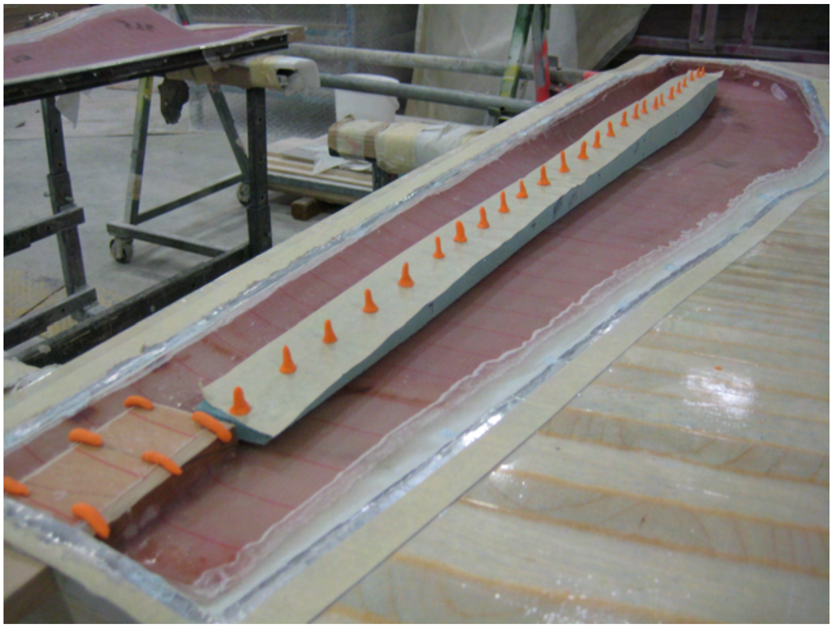

Figure A.19: Plasticine cones placed on blade inserts.

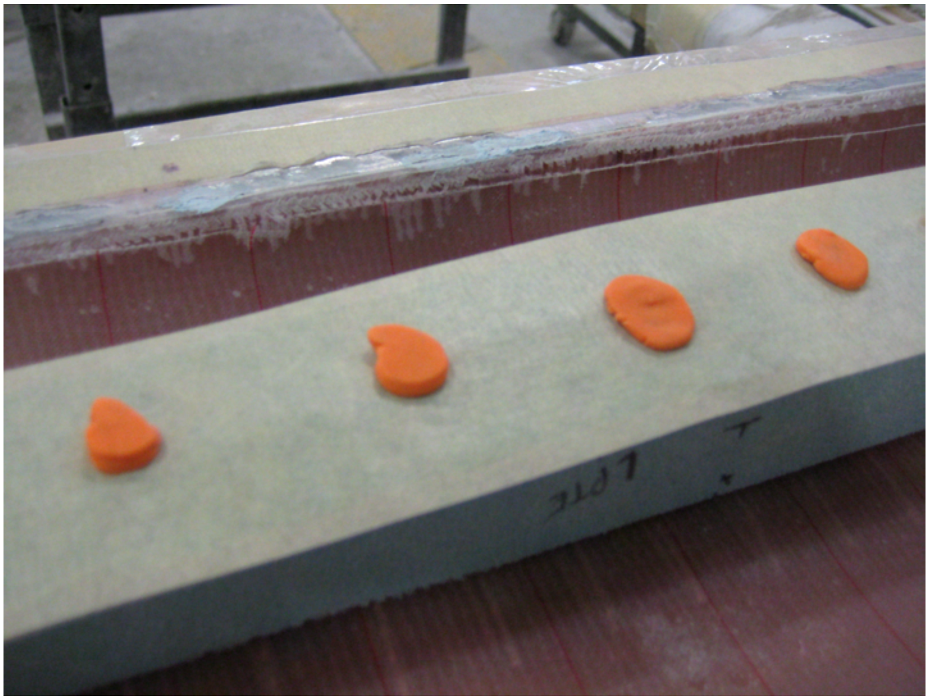

Figure A.20: Plasticine cones after having closed and re-opened mold.

The inserts are then pressed into place. See figure A.21 for a photo at this point. The coupler is locked in to place by sliding the locking bolts through the holes in the mold and into the bolt holes in the coupler block. The high-pressure mold is then inverted and placed onto the low-pressure mold such that the alignment dowels slide into the holes in the high pressure mold. Six clamps are applied and hand tightened to hold the mold closed. After curing overnight the parts are removed from the mold. Figure A.22 shows a photo of the blade after removal from the mold. Note the “flashing” extending from the blade at the seem between the high- and low-pressure shell. This was trimmed off prior to balancing, which is discussed next.

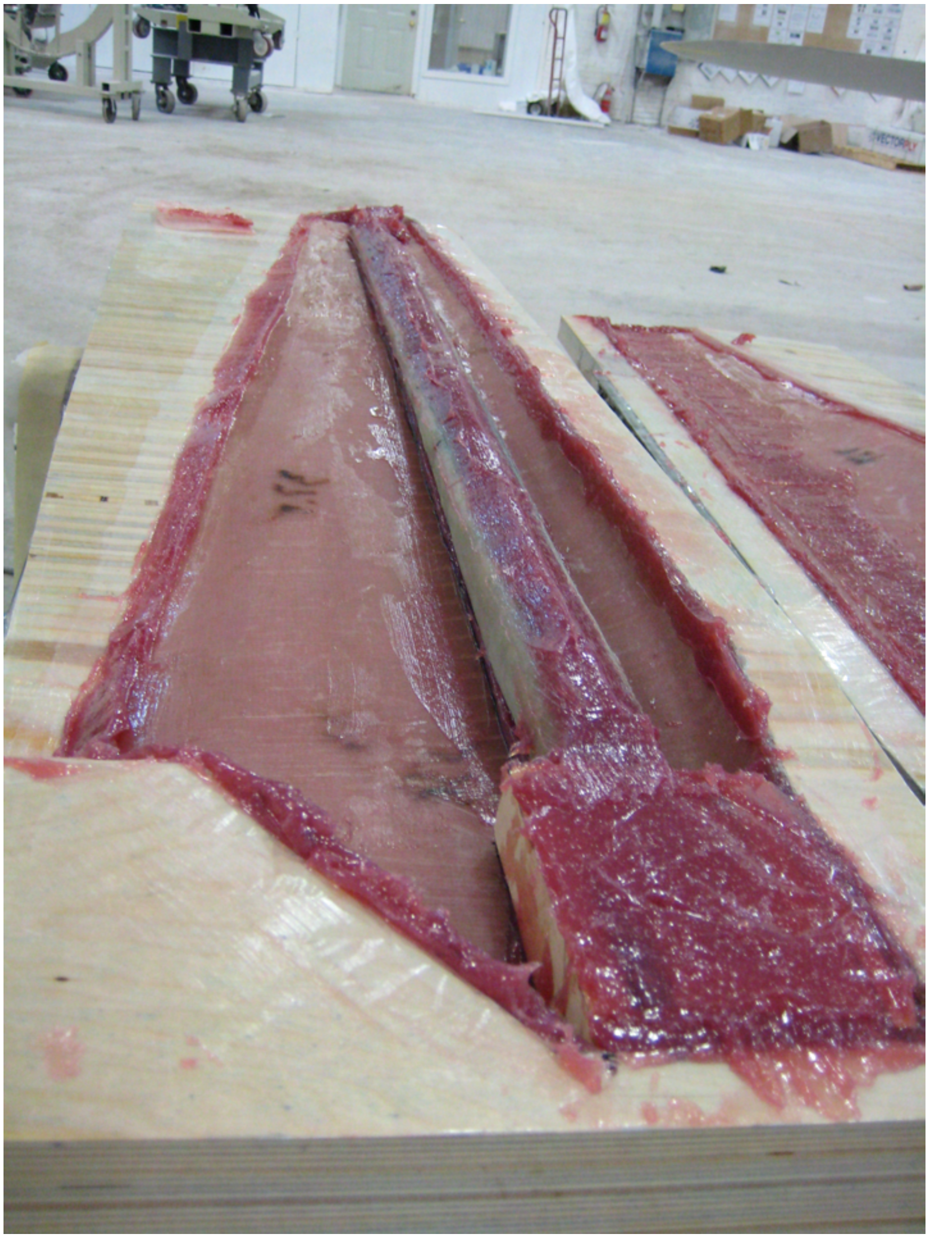

Figure A.21: Low pressure side mold with bonding putty applied.

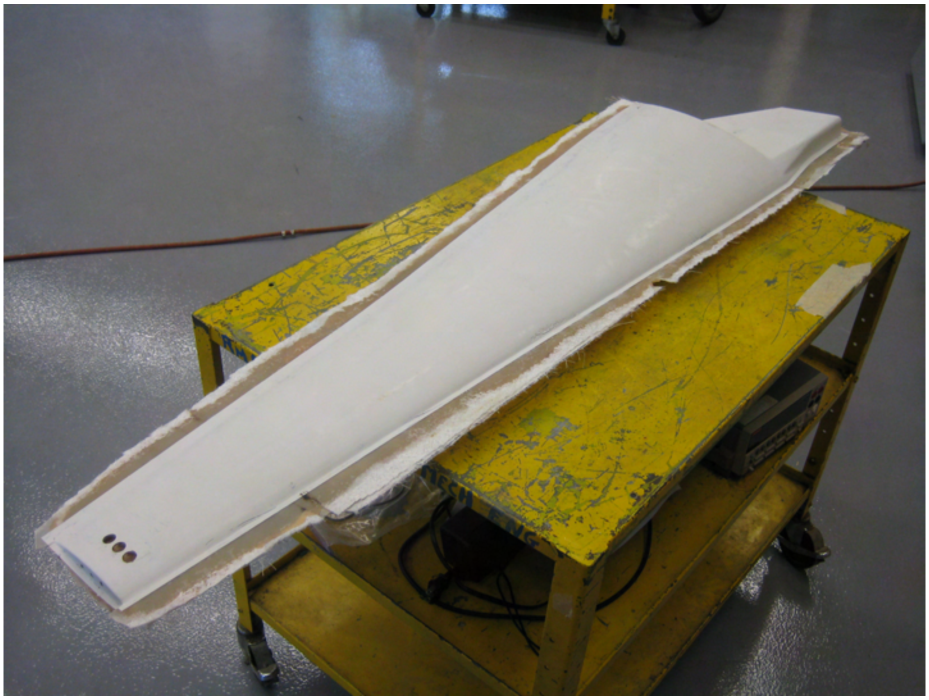

Figure A.22: Blade after cure and removal from mold.

A.6 Blade balancing

Blade balancing is required to limit vibrations that would otherwise arise due to the uneven centrifugal loads applied to the rotor shaft by the blades during operation. The procedure used to dynamically balance the blades was the same that is followed for commercial sized blades during periodic maintenance and refinishing. Balancing is achieved by adding weight to two of the three blades such that the static moment about the axis of rotation is constant for all three blades. Firstly, a static moment analysis is performed to determine the moment of each blade about the axis of rotation. To accomplish this, the mass of each blade is measured using two scales simultaneously. Knowing the distance from the axis of rotation to the location of each weighing point, the moment can be calculated. Figure A.23 displays a diagram of the forces and distances required for the moment calculation.

The moment about the axis of rotation is defined by equation A.1:

$$M = rm_r g + sm_s g \tag{A.1}$$

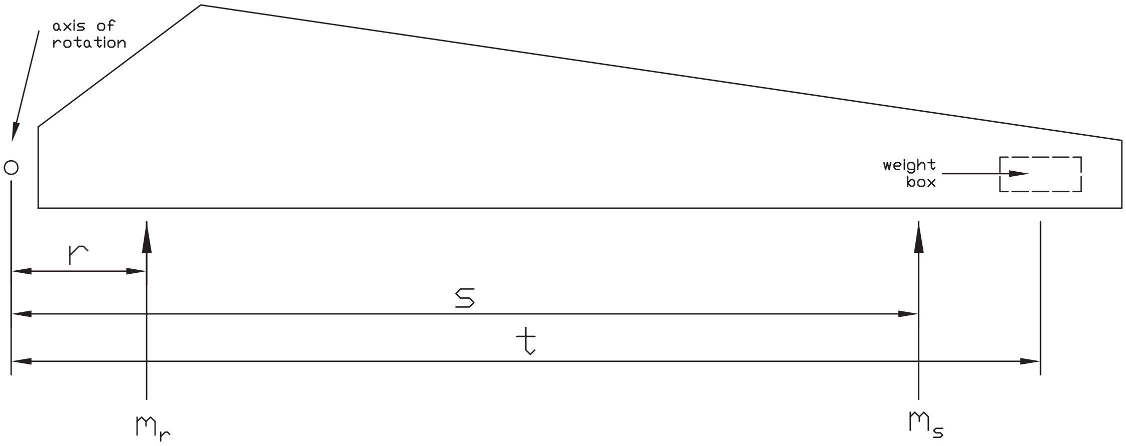

Figure A.23: Forces and distances used in moment analysis.

where m_r is the mass at a distance r from the axis of rotation, m_s is the mass at a distance s from the axis of rotation, and g is the acceleration due to gravity.

Typically, all three blades will have a slightly different moment, hence the requirement for balancing. The blade with the greatest moment is the reference blade. Using the weight box that was integrated into the coupler block (indicated in figure A.23), weight is added to the other two blades. A hole is drilled in the low-pressure side of the blade at the location of the weight box, and lead shot is added. The mass of lead shot required is determined using equation A.2:

$$m_l = \frac{M_o - M_i}{tg} \tag{A.2}$$

where M_o is the moment of the reference blade and M_i is the moment of the blade being balanced.

After adding the weight the hole is patched with bonding putty, fibre, and gel coat putty.

A.7 Blade finishing

The first step in the blade finishing process was to grind and sand down any remaining flashing to achieve a continuous surface everywhere but the trailing edge. At the trailing edge, the flashing had to be trimmed such that the design chord distribution was achieved. Using large calipers, the chord length at 10 blade stations was marked and a line was drawn joining those marks and indicating the desired profile of the trailing edge. The flashing was cut off along this line using a reciprocating saw. There were also various imperfections in the blade such as air gaps between the gel coat and skin layer, unsaturated fibre, etc. This occured mostly along the seam where the two blade halves were bonded together. All imperfections were grinded out and patched with gel coat putty. Next, the entire surface of each blade was sanded with 180 grit sandpaper. The surfaces were then blown off with compressed air and wiped down to remove all dirt. Finally, the blades were painted one side at a time with canned spray rust paint. First, a coat of primer was applied followed by enough coats of high-gloss to cover (roughly 6 - 10 coats waiting 15 minutes between each). It was important not to apply too much paint for each coat or the paint would build up and drips would result. After curing for 3 days the blades were flipped and the procedure repeated for the other side. Once painting was finished, the mounting bolt pattern was drilled using the mold as a jig. At this point the blades were ready to be mounted to the rig. See figure A.24 for a photo of a finished blade.

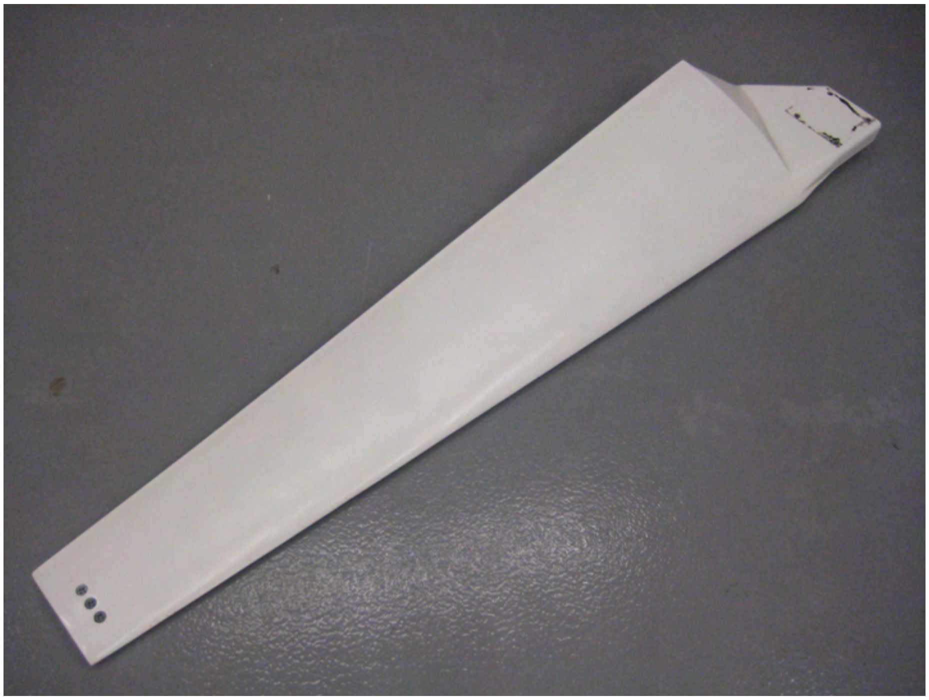

Figure A.24: Finished blade.

Appendix B

Tip Fabrication

The tips were milled out of maple wood using the in-house 3-axis OKK CNC machine. To accomplish this, a solid model of each tip was first produced using the SolidWorks solid modeling package. See figure B.1, figure B.2, and figure B.3 for the solid models of the standard, Maniaci, and Gertz tips, respectively.

Since a 3-axis mill was to be used to cut the parts, a method was devised to hold the part in place and cut one side, then flip the part and cut the other side while maintaining awareness of the coordinates of the first side. This method required 3 bolts to be threaded into one end of the tip, and another into the opposite end of the tip. Two aluminum blocks were prepared with holes such that the tip could be clamped between the blocks and the blocks secured to the mill table. The mill tool could then locate itself using the blocks and cut each side of the tip accurately. In the case of the winglets, additional material was added to either end such that the bolts could be threaded in without disturbing the finished surface. Once the entire surface other than the winglet tip was cut, the extra material was trimmed off the winglet tip. See figure B.4 for a photo of one of the tips during milling. Figure B.5 shows the tip in between having the first and second surface cut.

Once three of each tip had been cut the parts were painted with the same spray rust paint as the blades and the connecting bolts were threaded in. See figure B.6, figure B.7, and figure B.8 for photos of the finished standard, Maniaci, and Gertz tips, respectively. Three of the specialized winglet tips, discussed in section 4.1, were also produced by the same method.

Figure B.1: Solid model of standard tip.

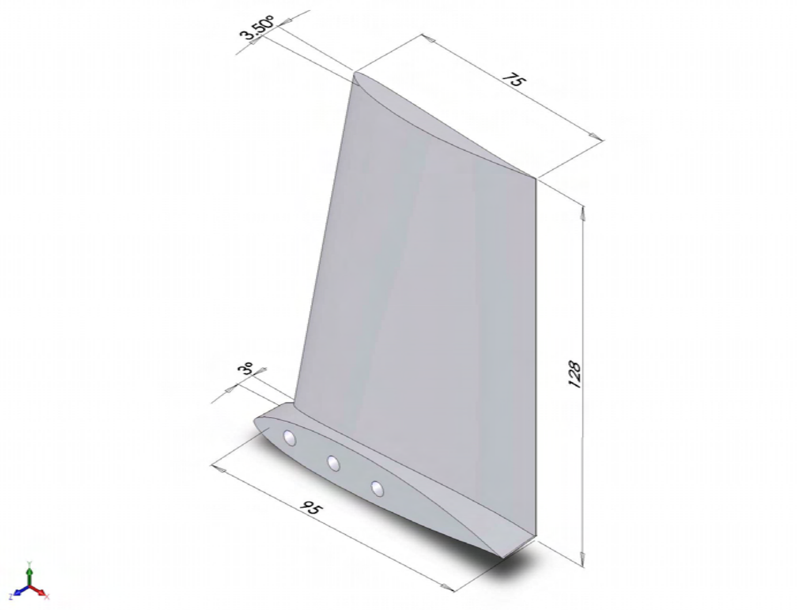

Figure B.2: Solid model of Maniaci tip.

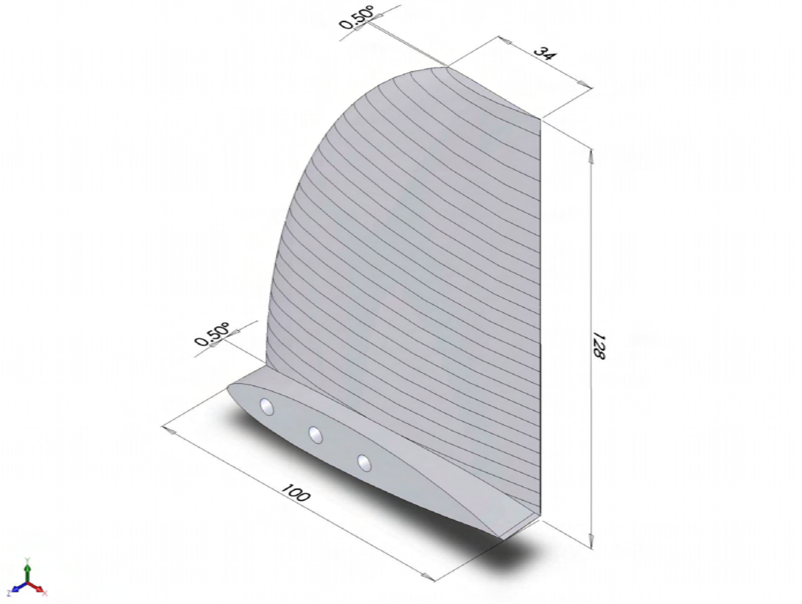

Figure B.3: Solid model of Gertz tip.

Figure B.4: One of the tips during milling.

Figure B.5: Tip in between having first and second surface milled.

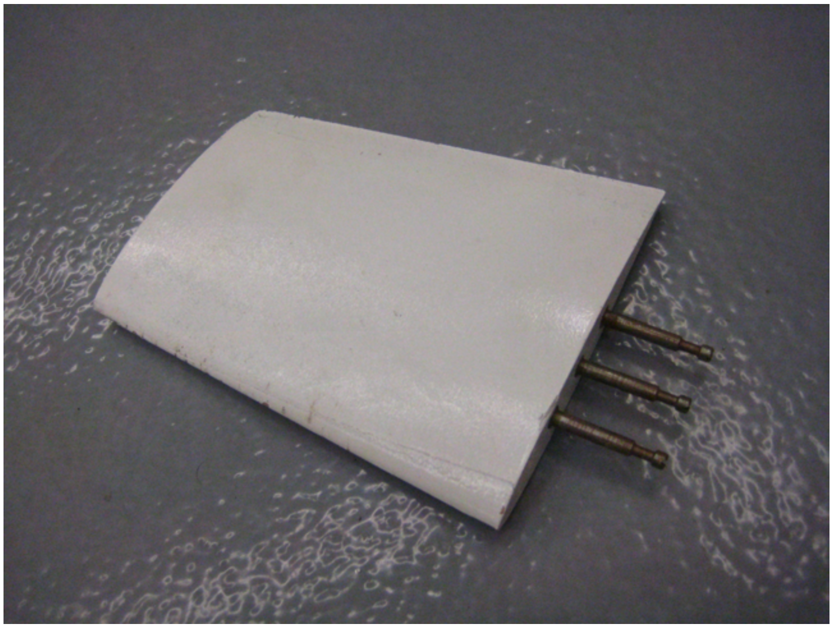

Figure B.6: Finished standard tip.

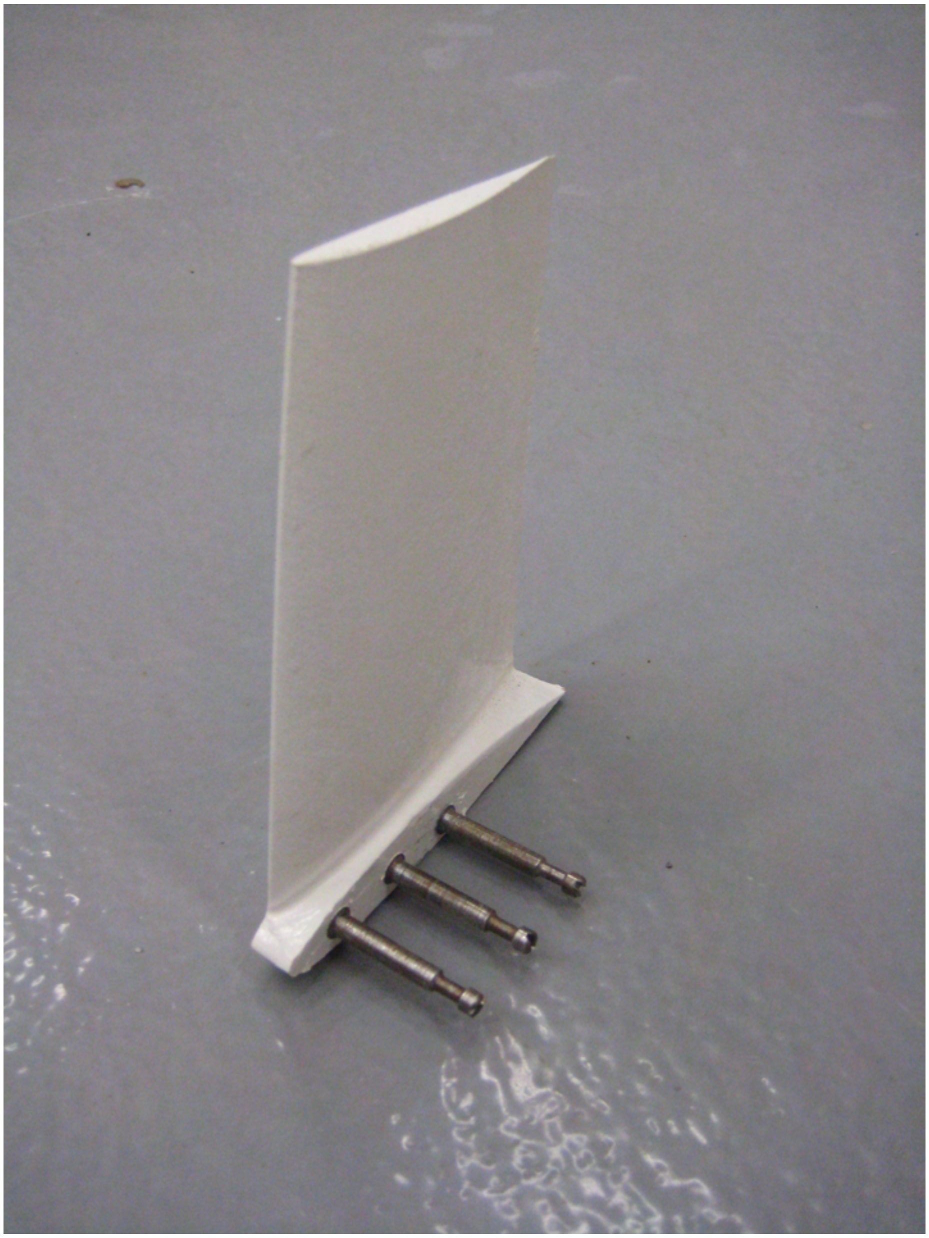

Figure B.7: Finished Maniaci tip.

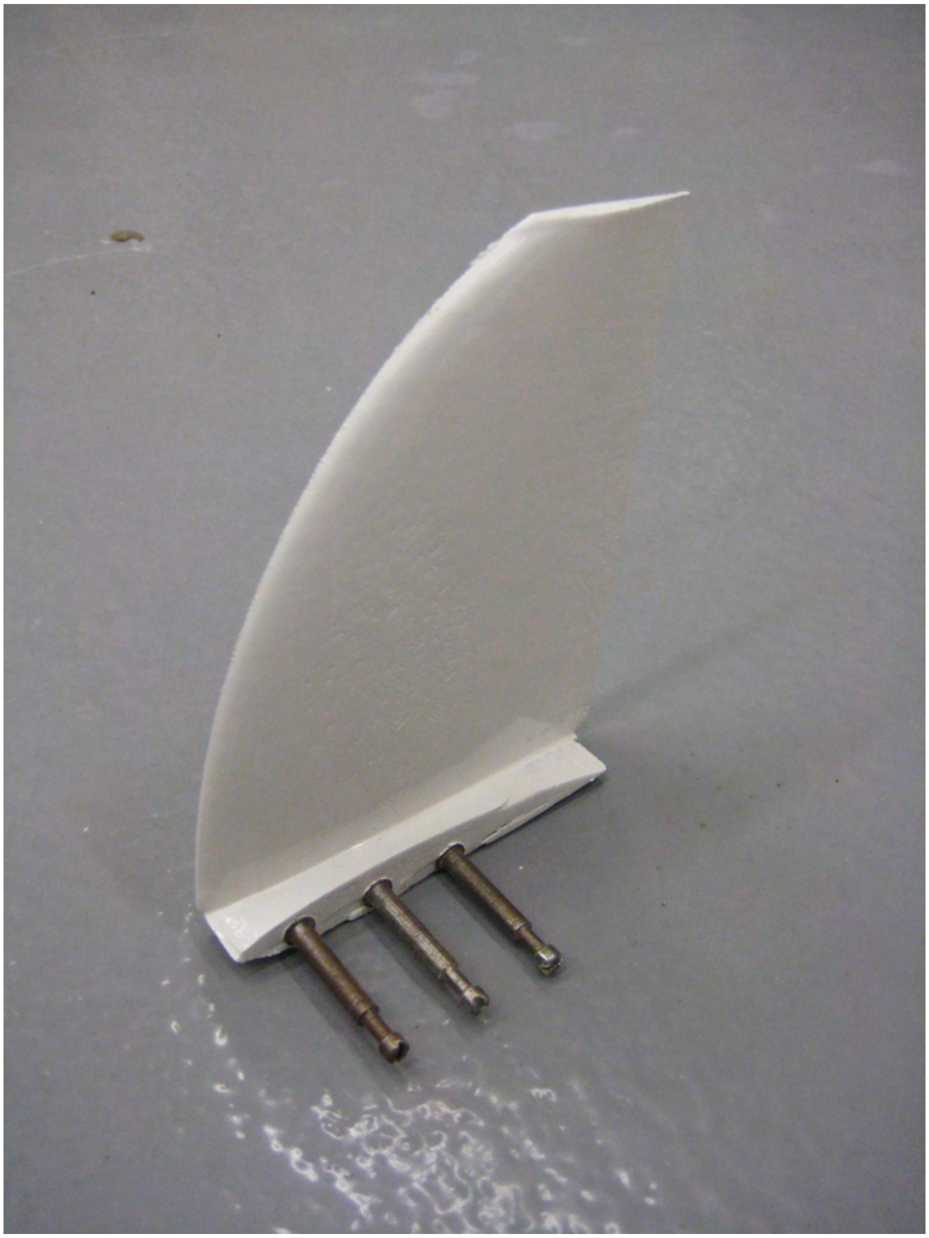

Figure B.8: Finished Gertz tip.

Appendix C

PROPID input file

```
# Started from wt06a.in
   # Variable Speed Turbine
   # Basic input
   MODE 1.0 # wind turbine
   INCV 0.0 # wind turbine mode (use TSR in analysis)
   LTIP 1.0 # use tip loss model
   LHUB 1.0 # use hub loss model
   IBR 1.0 # use brake state model
   ISTL 1.0 # use viterna stall model
   # 0 = use flat plate post-stall model
   USEAP 1.0 # use swirl suppression
   WEXP 0.0000 # boundary layer wind exponent
   NS_NSEC 10.0 1.0 # number of blade elements/number of sectors
   IS1 1.0 # first segment used in analysis
   IS2 10.0 # last segment used in analysis
   BE_DATA 0 # do not printout blade element data
   SH 0.0 # no shaft tilt effects on crossflow
   RHO 0.0023769 # air density (slugs/ft^3)
   # Geometry
   HUB 0.15 # normalized hub cutout
   HH 1.938 # normalized hub height
   BN 3 # blade number
   CONE 0.0 # cone angle of rotor (deg)
   RD 5.25 # radius (ft)
   CH_TW # Normalized chord and twist distribution
```

```
0.15 6
0.13 6
0.12 6
0.11 6
0.10 4
0.09 2
0.08 1
0.07 0
0.06 -1
0.05 -2
# Airfoil data files
AIRFOIL_MODE 4
5
S835_3D_trans_free.pd
.21 90 0 1.600 6
S835_3D_trans_free.pd
.21 90 0 1.600 6
S833_3D_trans_free.pd
.18 90 0 1.600 6
S834_3D_trans_free.pd
.15 90 0 1.600 6
S834_3D_trans_free.pd
.15 90 0 1.600 6
# airfoil family 1 with 5 airfoils
# r/R-location and airfoil index
AIRFOIL_FAMILY 5
.0000 1
.4000 2
.7500 3
.9500 4
1.0000 5
# use the first airfoil family (the one above)
USE_AIRFOIL_FAMILY 1
# Enforce tip loss model to always be on
TIPON
# Use the Prandtl tip loss model,
# not the original modified model.
TIPMODE 2
```

```
# Design point:  dsgnptnum, 200 rpm, 0 deg pitch, TSR 5 (6.7 m/s)
# Pick wind speed according to the avg wind speed
# for the GAEP line
# RPM set according to gearbox
# design pt 1:  200 rpm, 0.00 deg pitch, 6.5 m/s
DP 1 200 0.00 6.5 1
# Setup for the "A" airfoil data files
#
# For windspeed-alfa-cl-cd data at each blade station,
# specify filenames using the XJALCLCD_FILENAMES line.
# Data is generated on the fly
# during the wind speed sweep (2D_SWEEP line).
XJALCLCD_FILENAMES
10 # same as number of segments in CH_TW line
afclcd01a.dat
Station 1
afclcd02a.dat
Station 2
afclcd03a.dat
Station 3
afclcd04a.dat
Station 4
afclcd05a.dat
Station 5
afclcd06a.dat
Station 6
afclcd07a.dat
Station 7
afclcd08a.dat
Station 8
afclcd09a.dat
Station 9
afclcd10a.dat
Station 10
# Desired alpha distribution @ DP 1 1 1
# Seg radial loc alpha L/D Cl (max L/D)
# 1 no spec
# 2 0.15 6.00 47 0.95
```

```
  # 3 0.25 6.00 56 0.962
  # 4 0.35 6.00 57 0.963
  # 5 0.45 5.0
  # 6 0.55 5.0
  # 7 0.65 5.0
  # 8 0.75 4.7 65 0.9
  # 9 0.85 4.9
  # 10 0.95 5.00 58 0.761
  # Use this for automatic convergence
  #ITERMAX 15
  #TOLSP1 0.001
  #TOLSP2 0.001
  # Stage 1
  # Iterate on twist to get alpha(r/R=.75) = 4.7
  #>>line> NEWT1LDP <IFTP1(.)> <JSEGIX1(.)> <FNEWT1(.)> -
  # <KDPRPM1(.)> <KDPFL1(.)> <KDPXJ1(.)> -
  # <ITP1(.)> <ITP2(.)> <ITP3(.)> -
  # | <CLAMP1(.)> | <TOL1(.)>
  # Using ---> 500 local Cl of blade
  # 501 local a
  NEWT1LDP 502 8 4.7 1 1 1 1 3 1
  IDES
  # Stage 2
  # Iterate on twist to get alpha 9-10
  #>>line> NEWT2SDDP IFTP2(.)  JSEGIX2(.)  JSEGIX3(.)  JSEGREL(.)  KADJSBS(.)
  #>>line> <SSS(1)> <SSF(1)>
  #>>line> ...
  #>>line> <SSS(KADJSBS(.))> <SSF(KADJSBS(.))>
  #>>line> KDPRPM2(.)  KDPFL2(.)  KDPXJ2(.)  ISDTP(.)  ISCHED2(.)  | CLAMP2(.)
| TOL2(.)
  # Using ---> 100 Cl dist
  # 101 a dist
  # 102 alpha dist
  NEWT2SDDP 102 9 10 8 2
  1 0.2
  2 0.3
  1 1 1 2 100 .02
  IDES
```

```
  # Stage 3
  # Iterate on twist to get alpha 2-7
  #>>line> NEWT2SDDP IFTP2(.)  JSEGIX2(.)  JSEGIX3(.)  JSEGREL(.)  KADJSBS(.)
  #>>line> <SSS(1)> <SSF(1)>
  #>>line> ...
  #>>line> <SSS(KADJSBS(.))> <SSF(KADJSBS(.))>
  #>>line> KDPRPM2(.)  KDPFL2(.)  KDPXJ2(.)  ISDTP(.)  ISCHED2(.)  | CLAMP2(.)
| TOL2(.)
  # Using ---> 100 Cl dist
  # 101 a dist
  NEWT2SDDP 102 2 7 8 6
  1 1.3
  2 1.3
  3 1.3
  4 0.3
  5 0.3
  6 0.3
  1 1 1 2 100 .02
  IDES
  # Stage 4
  # Iterate on chord uniformly to get axial inflow(r/R=.75) = .333
  #>>line> NEWT1LDP <IFTP1(.)> <JSEGIX1(.)> <FNEWT1(.)> -
  # <KDPRPM1(.)> <KDPFL1(.)> <KDPXJ1(.)> -
  # <ITP1(.)> <ITP2(.)> <ITP3(.)> -
  # | <CLAMP1(.)> | <TOL1(.)>
  # 500 local Cl of blade
  # Using ---> 501 local a
  NEWT1LDP 501 8 .333 1 1 1 2 999 100 0.2
  IDES
  # Stage 5
  # Iterate on chord to get axial inflow 9-10
  #>>line> NEWT2SDDP IFTP2(.)  JSEGIX2(.)  JSEGIX3(.)  JSEGREL(.)  KADJSBS(.)
  #>>line> <SSS(1)> <SSF(1)>
  #>>line> ...
  #>>line> <SSS(KADJSBS(.))> <SSF(KADJSBS(.))>
  #>>line> KDPRPM2(.)  KDPFL2(.)  KDPXJ2(.)  ISDTP(.)  ISCHED2(.)  | CLAMP2(.)
| TOL2(.)
  # 100 Cl dist
```

```
  # Using ---> 101 a dist
  NEWT2SDDP 101 9 10 8 2
  1 .0
  2 .0
  1 1 1 1 100 .02
  IDES
  # Stage 6
  # Iterate on chord to get axial inflow 2-7
  #>>line> NEWT2SDDP IFTP2(.)  JSEGIX2(.)  JSEGIX3(.)  JSEGREL(.)  KADJSBS(.)
  #>>line> <SSS(1)> <SSF(1)>
  #>>line> ...
  #>>line> <SSS(KADJSBS(.))> <SSF(KADJSBS(.))>
  #>>line> KDPRPM2(.)  KDPFL2(.)  KDPXJ2(.)  ISDTP(.)  ISCHED2(.)  | CLAMP2(.)
| TOL2(.)
  # 100 Cl dist
  # Using ---> 101 a dist
  NEWT2SDDP 101 2 7 8 6
  1 .0
  2 .0
  3 .0
  4 .0
  5 .0
  6 .0
  1 1 1 1 100 .02
  IDES
  # Determine the rotor power, cp, and thrust curves (2D_SWEEP)
  #
  # use pitch setting from design point (DP) 1
  PITCH_DP 1
  # use rpm from design point (DP) 1
  RPM_DP 1
  # sweep the wind from 5 to 30 mph (cut-out spd) in increments of 1 mph
  WIND_SWEEP 5 30 1 2
  # perform the sweep
  2D_SWEEP
  # write out
  # 40 - power curve (kW) vs wind speed (mph)
  # 45 - cp vs TSR
```

```
# 51 - rotor thrust curve
WRITE_FILES 40 45 51
# Obtain aero distributions along the blade (1D_SWEEP)
#
PITCH_DP 1
RPM_DP 1
WIND_DP 1
1D_SWEEP
# write out
# 60 - blade power dist
# 65 - blade Cp dist
# 75 - blade l/d dist
# 76 - blade Re dist
# 80 - blade alfa dist
# 85 - blade cl dist
# 90 - blade a dist
# 95 - chord dist (ft-ft)
# 99 - alfa dist (ft-deg)
WRITE_FILES 75 76 80 85 90 95 99
# Setup for the "B" airfoil data files
# A second way to get airfoil data
#
# Generate airfoil data for each blade station
# at the Reynolds number corresponding to the last
# analysis case (19 mph).
#
# Use the Reynolds number store in the Re array.
STATION_RE 2
# Give the individual airfoil data filenames for each segment
AIRFOIL_FILENAMES
10
afclcd01b.dat
Station 1
afclcd02b.dat
Station 2
afclcd03b.dat
Station 3
afclcd04b.dat
```

```
Station 4
afclcd05b.dat
Station 5
afclcd06b.dat
Station 6
afclcd07b.dat
Station 7
afclcd08b.dat
Station 8
afclcd09b.dat
Station 9
afclcd10b.dat
Station 10
# Include a single composite file of all data, plus some header info
OUTGRAPH
airfoil.dat
# Set the alfa range
ALFA_MIN_MAX_INC 1
-5 90 1
# Uncomment line below to have comments written
# to the afclcd*a.dat files.
#WRITE_HEADERS
# Set data format to alfa-cl-cd
ITYPE 3
# Generate the alfa-cl-cd data for all 10 segments (10 files)
# and make the composite "airfoil.dat" file.
MAKE_PROP_AFDATA
# Annual energy production
GAEP 19 19 1 30
REPORT_START
# Report the last GAEP analysis case
REPORT_SPECIAL 8 999 999
REPORT_END
# Write out the rotor design parameters to file ftn021.dat
DUMP_PROPID
*
```

Appendix D

WT_Perf input file

```
----- WT_Perf Input File -----------------------------------------------------
   Drew Gertz thesis project turbine
   Compatible with WT_Perf v3.00f
   ----- Input Configuration ----------------------------------------------------
   False Echo:  Echo input parameters to "<rootname>.ech"?
   False DimenInp:  Turbine parameters are dimensional?
   True Metric:  Turbine parameters are Metric (MKS vs FPS)?
   ----- Model Configuration ----------------------------------------------------
   16 NumSect:  Number of circumferential sectors.
   5000 MaxIter:  Max number of iterations for induction factor.
   1.0e-6 ATol:  Error tolerance for induction iteration.
   1.0e-6 SWTol:  Error tolerance for skewed-wake iteration.
   ----- Algorithm Configuration ------------------------------------------------
   True TipLoss:  Use the Prandtl tip-loss model?
   True HubLoss:  Use the Prandtl hub-loss model?
   True Swirl:  Include Swirl effects?
   True SkewWake:  Apply skewed-wake correction?
   True AdvBrake:  Use the advanced brake-state model?
   True IndProp:  Use PROP-PC instead of PROPX induction algorithm?
   True AIDrag:  Use the drag term in the axial induction calculation?
   True TIDrag:  Use the drag term in the tangential induction calculation?
   ----- Turbine Data -----------------------------------------------------------
   3 NumBlade:  Number of blades.
   1.65 RotorRad:  Rotor radius [length].
   0.0 HubRad:  Hub radius [length or div by radius].
```

```
   0.0 PreCone:  Precone angle, positive downwind [deg].
   0.0 Tilt:  Shaft tilt [deg].
   0.0 Yaw:  Yaw error [deg].
   10 HubHt:  Hub height [length or div by radius].
   10 NumSeg:  Number of blade segments (entire rotor radius).
   RElm Twist Chord AFfile PrntElem
   0.05 0 0.001 1 FALSE
   0.15 18.9576 0.1875 1 FALSE
   0.25 18.9576 0.172825 1 FALSE
   0.35 15.7776 0.158115 1 FALSE
   0.45 12.7634 0.143405 1 FALSE
   0.55 9.1596 0.128695 5 FALSE
   0.65 6.669 0.113985 5 FALSE
   0.75 5.488 0.099275 5 FALSE
   0.85 4.2911 0.084565 7 FALSE
   0.95 2.0724 0.069855 7 FALSE
   ----- Aerodynamic Data -------------------------------------------------------
   1.225 Rho:  Air density [mass/volume].
   1.4639e-5 KinVisc:  Kinematic air viscosity
   0 ShearExp:  Wind shear exponent (1/7 law = 0.143).
   False UseCm:  Are Cm data included in the airfoil tables?
   7 NumAF: Number of airfoil files.
   "CertTest/Airfoils/S83X/S835.dat" AF_File:  List of NumAF airfoil files.
   "CertTest/Airfoils/S83X/S83X45%.dat"
   "CertTest/Airfoils/S83X/S83X55%.dat"
   "CertTest/Airfoils/S83X/S83X65%.dat"
   "CertTest/Airfoils/S83X/S833.dat"
   "CertTest/Airfoils/S83X/S83X85%.dat"
   "CertTest/Airfoils/S83X/S834.dat"
   ----- I/O Settings -----------------------------------------------------------
   True TabDel:  Make output tab-delimited (fixed-width otherwise).
   False KFact:  Output dimensional parameters in K (e.g., kN instead on
N)
   True WriteBED: Write out blade element data to "<rootname>.bed"?
   False InputTSR: Input speeds as TSRs?
   "mps" SpdUnits:  Wind-speed units (mps, fps, mph).
   ----- Combined-Case Analysis -------------------------------------------------
   0 NumCases:  Number of cases to run.  Enter zero for parametric analysis.
```

```
   WS or TSR RotSpd Pitch Remove following block of lines if NumCases is
zero.
   ----- Parametric Analysis (Ignored if NumCases > 0 ) -------------------------
   3 ParRow:  Row parameter (1-rpm, 2-pitch, 3-tsr/speed).
   2 ParCol:  Column parameter (1-rpm, 2-pitch, 3-tsr/speed).
   1 ParTab:  Table parameter (1-rpm, 2-pitch, 3-tsr/speed).
   True OutPwr:  Request output of rotor power?
   True OutCp:  Request output of Cp?
   False OutTrq:  Request output of shaft torque?
   False OutFlp:  Request output of flap bending moment?
   False OutThr:  Request output of rotor thrust?
   0,0,1 PitSt, PitEnd, PitDel:  First, last, delta blade pitch (deg).
   200,200,1 OmgSt, OmgEnd, OmgDel:  First, last, delta rotor speed (rpm).
   2,22.5,.1 SpdSt, SpdEnd, SpdDel:  First, last, delta speeds.
```

Appendix E

Uncertainty analysis

This section outlines the methods that were used to estimate the uncertainty in the experimental results. The fundamental theory is first presented followed by the specific methods used to determine the uncertainty in the various quantities presented in the paper.

E.1 General theory

Uncertainty in experimental measurements is made up of two components called the precision and the bias. Precision (also called random) uncertainty is due to the statistical variance of data and is constant for a population. Bias (also called systematic) uncertainty is due to instrumentation inaccuracies and often depends on the magnitude of the quantity being measured. The total uncertainty (U_r) of the quantity r is found by root sum squared summation of the bias (B_r) and precision (P_r) components, as outlined in equation E.1 [74]:

$$U_r = \sqrt{B_r^2 + P_r^2} \tag{E.1}$$

where $r \pm U_r$ provides a 95% confidence interval for the result [74]. For sample sizes larger than 10, the precision uncertainty is defined by the standard deviation (S_x) and size (N) of the sample population:

$$P_r = \frac{2S_x}{\sqrt{N}} \tag{E.2}$$

The bias uncertainty is either provided by the manufacturer of the measurement instrument or estimated based on the type of instrument. When estimating the

Measurement	label	units	Bias uncertainty	Source
wind speed at test section entrance	$V_{upstream}$	m/s	$0.02r \pm 0.04$	manual [75]
rotor speed	Ω	rpm	3.33×10^{-3}	estimate
air temperature (from c_s)	T	K	$0.02r \pm 0.04$	manual [75]
load voltage	V	V	see table E.2	
load current (from shunt)	I	A	$0.01r$	estimate
blade radius	R	m	0.005	estimate

Table E.1: Bias uncertainties for measured quantities.

uncertainty (U_f) of a quantity ($f(r_i)$) that is calculated using one or a combination of measured values (r_1,r_2,...,r_n), a partial derivative method is used, as shown in equation E.3:

$$U_f = \sqrt{\left(r_1 \frac{\delta f(r_i)}{\delta r_1}\right)^2 + \left(r_2 \frac{\delta f(r_i)}{\delta r_2}\right)^2 + ... + \left(r_n \frac{\delta f(r_i)}{\delta r_n}\right)^2} \tag{E.3}$$

E.2 Uncertainties in measured and calculated values

For this experiment, the measured quantities were the wind speed, rotor speed, air temperature, load voltage, load current, and blade radius. The sample size of all of the data sets was greater than 10 thus equation E.2 was used to determine the precision uncertainty. The bias uncertainties were either estimated or gathered from the instrument documentation and are outlined in table E.1.

The Keithley 2700 data acquisition system [68] was used to gather all of the signals. Thus there is an additional bias uncertainty introduced to those quantities that is calculated based on the values in table E.2.

The uncertainty due to the Keithley 2700 is a function of the reading, the range used, and the ambient temperature of the area in which the Keithley is located. With the bias and precision uncertainties established for each measured parameter, they were propagated through the data reduction equations outlined in section 6.2.1. The uncertainty propagation methods for the various calculations are outlined next. All

Range (V)	Resolution (μV)	Error on reading	Error on range	Coefficient on reading ($/^oC$)	Coefficient on range ($/^oC$)
0.1	0.1	30×10^{-6}	35×10^{-6}	1×10^{-6}	5×10^{-6}
1.0	1.0	30×10^{-6}	7×10^{-6}	1×10^{-6}	1×10^{-6}
10.0	10.0	30×10^{-6}	5×10^{-6}	1×10^{-6}	1×10^{-6}
100.0	100.0	45×10^{-6}	9×10^{-6}	5×10^{-6}	1×10^{-6}
1000.0	1000.0	50×10^{-6}	9×10^{-6}	5×10^{-6}	1×10^{-6}

Table E.2: Uncertainty due to Keithley 2700.

U values are calculated using the precision and bias methods outlined above.

E.2.1 Velocity at rotor plane

The velocity at the rotor plane (V_{disc}) was calculated using equation 6.1. The uncertainty in this quantity ($U_{V_{disc}}$) was calculated as follows:

$$U_{V_{disc}} = \sqrt{\left(\frac{\delta V_{disc}}{\delta V_{upstream}} U_{V_{upstream}}\right)^2} \tag{E.4}$$

Recall that V_{disc} was calculated based on $V_{upstream}$ using a pre-determined relation. This curve fit was assumed not to introduce any significant error.

E.2.2 Power

The power (P_{GEN})was calculated by summation of the power at the load bank and the power train loss estimate. It's uncertainty ($U_{P_{GEN}}$) was calculated as follows:

$$U^2_{P_{GEN}} = \left(\frac{\delta P_{GEN}}{\delta V} U_V\right) + \left(\frac{\delta P_{GEN}}{\delta I} U_I\right)^2 + \left(\frac{\delta P_{GEN}}{\delta P_{spinrotor}} U_{P_{spinrotor}}\right)^2 + \left(\frac{\delta P_{GEN}}{\delta P_{rotordrag}} U_{P_{rotordrag}}\right)^2$$

where

$$U_{P_{spinrotor}} = \sqrt{\left(\frac{\delta P_{spinrotor}}{\delta V} U_V\right)^2 + \left(\frac{\delta P_{spinrotor}}{\delta I} U_I\right)^2} \tag{E.5}$$

$$U_{P_{rotordrag}} = \sqrt{\left(\frac{\delta P_{rotordrag}}{\delta V} U_V\right)^2 + \left(\frac{\delta P_{rotordrag}}{\delta I} U_I\right)^2} \tag{E.6}$$

Recall that $P_{rotordrag}$ was calculated based on the instantaneous temperature and rotor speed using a pre-determined relation. Although the precision and bias error of the values used to determine the relation were accounted for, the curve fit was assumed not to introduce any significant error.

E.2.3 Density

The density (ρ) is a function of temperature and pressure. It's error U_ρ was determined using the following equation:

$$U_\rho = \sqrt{\left(\frac{\delta \rho}{\delta T} U_T\right)^2 + \left(\frac{\delta \rho}{\delta P} U_P\right)^2} \tag{E.7}$$

The pressure (P) was not measured but was gathered from the UW weather station web site [70]. It was assumed that this quantity had a precision uncertainty of 80 Pa and no bias uncertainty.

E.2.4 Tip speed ratio

The tip speed ratio (λ) is defined by equation 2.14 and is a function of Ω, R, and V_{disc}. It's uncertainty (U_λ) was calculated using the following equation:

$$U_\lambda = \sqrt{\left(\frac{\delta \lambda}{\delta \Omega} U_\Omega\right)^2 + \left(\frac{\delta \lambda}{\delta R} U_R\right)^2 + \left(\frac{\delta \lambda}{\delta V_{disc}} U_{V_{disc}}\right)^2} \tag{E.8}$$

E.2.5 Power coefficient

The power coefficient (C_P) is calculated using equation 2.11. It's uncertainty (U_{C_P}) was calculated as follows:

$$U_{C_P} = \sqrt{\left(\frac{\delta C_P}{\delta P_{GEN}} U_{P_{GEN}}\right)^2 + \left(\frac{\delta C_P}{\delta R} U_R\right)^2 + \left(\frac{\delta C_P}{\delta V_{disc}} U_{V_{disc}}\right)^2 + \left(\frac{\delta C_P}{\delta \rho} U_\rho\right)^2} \tag{E.9}$$